Syngap1 Promotes Cognitive Function through Regulation of Cortical Sensorimotor Dynamics

Thomas Vaissiere[1*], Sheldon D. Michaelson[1*], Thomas Creson[1], Jessie Goins[1], Daniel Fürth[2], Diana Balazsfi[1], Camilo Rojas[1], Randall Golovin[1], Konstantinos Meletis[3], Courtney A. Miller[1,4], Daniel O'Connor[5], Lorenzo Fontolan[6], and Gavin Rumbaugh[1#]

[1]Department of Neuroscience, The Herbert Wertheim UF Scripps Institute for Biomedical Innovation & Technology, Jupiter, FL, USA

[2]SciLifeLab, Department of Immunology, Genetics & Pathology, Uppsala University, Uppsala, Sweden

[3]Department of Neuroscience, Karolinska Institute, 17177 Stockholm, Sweden

[4]Department of Molecular Medicine, UF Scripps Biomedical Research, Jupiter, FL, USA

[5]Department of Neuroscience, The Johns Hopkins University School of Medicine, Baltimore, MD, USA

[6] Aix-Marseille Université, INSERM, INMED, Turing Centre for Living Systems, Marseille, 13009, France

**Equal Contribution*

[#]Correspondence: Gavin Rumbaugh, PhD
Department of Neuroscience
The Herbert Wertheim UF Scripps Institute for Biomedical Innovation & Technology
120 Scripps Way, #3B3
Jupiter, FL 33458
gavinrumbaugh@ufl.edu

Summary

Perception, a cognitive construct, emerges through sensorimotor integration (SMI). The genetic mechanisms that shape SMI required for perception are unknown. Here, we demonstrate in mice that expression of the autism/intellectual disability gene, *Syngap1*, in cortical excitatory neurons is required for formation of somatomotor networks that promote SMI-mediated perception. Cortical *Syngap1* expression was necessary and sufficient for setting tactile sensitivity, sustaining tactile object exploration, and promoting tactile learning. Mice with deficient *Syngap1* expression exhibited impaired neural dynamics induced by exploratory touches within a cortical-thalamic network known to promote attention and perception. Disrupted neuronal dynamics were associated with circuit-specific long-range synaptic connectivity abnormalities. Our data support a model where autonomous *Syngap1* expression in cortical excitatory neurons promotes cognitive abilities through assembly of circuits that integrate temporally-overlapping sensory and motor signals, a process that promotes perception and attention. These data provide systems-level insights into the robust association between *Syngap1* expression and cognitive ability.

Introduction

Sensorimotor integration (SMI) refers to the neurophysiological phenomenon reflecting how sensory processing and motor output influence each other[1,2]. SMI is essential to a range of motor and higher cognitive functions, from posture, balance and movement control to attention, memory, and learning[3–7]. Sensory and motor signals are conveyed across multiple time scales through distributed networks and brain areas[5]. In rodents, disrupting SMI impairs neural representations of object features (texture, contour, and relative location), which are required for more complex cognitive functions to emerge, such as sensory perception and salience[8–12]. However, the neurobiological processes that shape the connectivity of distributed SMI networks that promote higher cognitive functions remain unknown. This hinders our understanding of the neural correlates of adaptive behaviors.

In addition to supporting a healthy brain, SMI processes are associated with a diverse range of disease/disorder states. This includes clumsiness, abnormal eye tracking, and altered sensory integration/reactivity, which are core features of neuropsychiatric disorders, such ASD and psychosis, and are also observed as “soft signs” in many neurological disorders [13–18]. Genetic factors in the central and peripheral nervous systems have been implicated in abnormal sensory reactivity and altered motor control [19–23]. Mutations in several genes have been identified in neurodevelopmental disorders (NDD) that feature alterations in sensory processing, motor control, and intellectual ability [24–29]. Impaired SMI could, therefore, be a neural substrate of altered cognitive processes broadly observable in mental health disorders[28,30–33]. However, there have been comparatively few neurobiological investigations into how highly penetrant NDD risk genes contribute to SMI, resulting in a poor understanding of how gene expression shapes this essential neural process in health and disease.

We hypothesized that highly penetrant NDD genes regulate neurophysiological correlates of SMI required for higher cognitive functions. As an initial test of this hypothesis, we chose a

relevant NDD gene and then tested how its expression contributed to SMI and associated cognitive functions. We chose *SYNGAP1*/*Syngap1* because expression of this NDD gene in humans and mice, respectively, is required for both sensory processing and motor control [23,34]. Indeed, *de novo* mutations that lower *SYNGAP1* expression in humans cause a developmental and epileptic encephalopathy defined by impaired cortical excitability, postural/gait abnormalities, sensory processing impairments, and moderate-to-severe intellectual disability[35–40]. Moreover, a recent highly-powered genome-wide association study directly linked the *SYNGAP1* locus to cognitive abilities [41]. Importantly, excellent mouse genetic tools are available for the study of *Syngap1* at the systems level. These tools enable region- and/or cell-specific bidirectional regulation of its expression, which allow spatial and temporal investigations into how *Syngap1* regulates distributed neural systems associated with SMI. These models have been used to uncover a role for *Syngap1* in cortical processing of sensory signals and control of motor responses required for decision-making [23,40,42]. However, it remains unknown if *Syngap1* expression regulates neural correlates of SMI, and if so, how this contributes to constructs of cognition required for behavioral adaptation.

Here, *Syngap1* mouse genetic tools were used to explore how its expression regulates neurobehavioral correlates of SMI associated with constructs of cognition. To explore this, we utilized behavioral paradigms that rely on passive (receptive) and active (generative) whisker sensing to drive perceptual learning [43,44]. In active tasks, tactile feedback enables closed loop, ongoing control of whisker motion, which promotes perception by enabling self-generated control of object exploration during tactile learning [9,45].The structural and functional connectivity of the rodent somatomotor whisker system has been extensively elucidated [30,46–49]. The key nodes in higher-order whisker-related motor-sensory-motor (MSM) loops are known, and paradigms have been established that enable neurophysiological measurements of neuronal populations that mediate motor control during whisking, as well as tactile signals generated

during object exploration. Importantly, disrupting self-generated motor control of whiskers during object exploration impairs perceptual learning [9,50]. Thus, simultaneous tracking of whisker movement during object exploration and recording of activity within integrative neuronal populations enables elucidation of neurobiological principles that link SMI to cognition and behavior.

Using this framework, we utilized an array of *Syngap1* mouse models in learning paradigms that require the use of whiskers to generate percepts for behavioral adaptation. We paired these investigations with structural and functional analysis of somatomotor-associated neural circuits that integrate tactile and whisker motor signals. Combining these approaches, we demonstrate that *Syngap1* expression in cortical excitatory neurons is required for perceptual decision-making driven by tactile input, and for tactile-generated feedback control of whisker motion that underlies attention during active sensing. We also demonstrate that *Syngap1* regulates the structural/functional connectivity of cortical circuits within MSM loops known to integrate signals coding for touch and whisker motion. Together, these results demonstrate that a key function of *Syngap1* expression is to promote balanced integration of tactile and whisker motor signals within cortical sensorimotor loops. We propose that this form of abnormal SMI within the cortex of *Syngap1* mice contributes to reduced tactile sensitivity, poor attention, weak perceptual learning, and maladaptive behaviors. To our knowledge, this is the first demonstration for how impaired tactile processing associated with neurodevelopmental disorder genes can directly degrade cognitive performance required for behavioral adaptation.

Results

Syngap1 expression promotes whisker touch sensitivity and perceptual learning:

We and others have previously demonstrated a role for *Syngap1* in both tactile learning and neural representations of tactile stimuli in somatosensory cortex [23,51,52]. However, this past work

123 did not define if, how, and to what extent *Syngap1* contributes to tactile learning through
124 sensory processing. To begin to investigate sensory-mediated mechanisms linking *Syngap1*
125 expression to perceptual learning underlying behavioral adaptation, we utilized a variation of a
126 head-fixed tactile detection task where water-restricted animals were trained to provide a
127 perceptual report of a passive whisker stimulation by licking a sensor that also supplies a water
128 reward in mice older than 8 weeks of age. **(Fig. 1a)**. Three separate cohorts of *Syngap1*$^{+/+}$
129 (*wildtype* – normal SynGAP protein expression) and *Syngap1*$^{+/-}$ (+/-, germline heterozygous –
130 half SynGAP protein expression) mice were trained, with each cohort receiving either a weak,
131 medium, or strong whisker training stimulus during "Go" trials. Go trials were defined by a piezo
132 deflection that induced a whisker stimulation; an animal scored a "hit" when licking the detector
133 on these trials. "NoGo" trials were defined by a piezo deflection that did not translate into a
134 whisker stimulus; an animal scored a "correct rejection" (CR) by withholding licking during these
135 trials. We evaluated task performance of *wildtype* and *Syngap1*$^{+/-}$ mice by measuring total
136 correct choices (hit on Go trials; CR on NoGo trials), overall Hit rate, overall False Alarm (FA)
137 rate (FA = licking on a NoGo trial), and a trial discrimination index (*d'*). Stimulus intensity
138 positively correlated with performance in *wildtype* mice, with faster learning over the 21-day
139 training period with stronger stimulus intensity **(Fig. 1b)**, and improved trial discrimination at the
140 end of training in strong versus weak training stimuli **(Supplementary Fig. 1a-i)**. However,
141 *Syngap1* heterozygous mice exhibited deficient learning compared to controls as evidenced by
142 fewer total correct choices, particularly in the strongest training stimulus **(Fig. 1b;**
143 **Supplementary Table 1).** Additional analysis of trial data revealed that *Syngap1*$^{+/-}$ mice
144 exhibited fewer Hits compared with littermate controls in the medium stimuli paradigm
145 **(Supplementary Fig. 1d-f)**, and fewer hits with more FAs in the strong stimulus experiment
146 **(Supplementary Fig. 1g-i)**. A generalized linear mixed model that considered all three cohorts
147 revealed that the probability of correct choices in *Syngap1* heterozygous mice was less
148 sensitive to increases in training stimulus intensity **(**$F(57, 662.8)=2.8$, $p<0.001$**, Supplementary**

149 **Table 1)**. This suggested that *Syngap1* mice have reduced tactile sensitivity, though dual Hit
150 and FA impairments, which could be a consequence of a fundamental disruption to distributed
151 and generalized reinforcement learning mechanisms and/or motor control issues. To definitively
152 determine if *Syngap1*$^{+/-}$ mice exhibit reduced tactile sensitivity, we carried out a "pull-back"
153 experiment[53] where animals that met acquisition criteria were subjected to a daily reduction in
154 Go-stimulus intensity **(Fig. 1c)**. This experiment was possible because of a modified 3-step
155 training paradigm that selected for a subset of *Syngap1*$^{+/-}$ mice that learned to the same degree
156 as *wildtype* littermates with the strong stimulus cohort **(Supplementary Fig. 1j-n)**. Thus, when
157 additional *Syngap1*$^{+/-}$ mice were trained and the poor learners excluded from additional in-depth
158 training, trial performance ended up no different between genotypes after 21 days of training
159 **(Fig. 1d –** ***first data point*****).** In this pull-back paradigm, there was an effect of genotype and an
160 interaction between genotype and stimulus intensity in Go trials **(Fig. 1d)**. Indeed, in well-trained
161 *Syngap1*$^{+/-}$ mice, Hit rates decreased faster relative to littermate controls as the stimulus
162 intensity was reduced ($F(4,40)=2.62$, $p<0.05$). These head-fixed passive whisker stimulation
163 task data demonstrate that *Syngap1* expression promotes tactile sensitivity.
164
165 This task reflects perceptual learning through a passive tactile stimulus. However, animals in the
166 wild, including rodents and humans, most often acquire sensory information through self-
167 generated movement of sense organs[54,55]. Therefore, we sought to determine the extent to
168 which *Syngap1* expression regulated tactile sensitivity and associated perceptual adaptations in
169 active sensing paradigms. First, we employed an active whisker-touch paradigm, **N**ovel
170 **O**bjection **R**ecognition using only **T**exture **(NOR-T)**[23], which was carried out in freely moving
171 animals and was, therefore, ethological in nature. Freely moving mice in the dark were tasked
172 with discriminating between two visually identical objects that only differed in texture **(Fig. 2a)**.
173 Trimming whiskers in *wildtype* test mice prevented the expected shift in time spent around the
174 novel textured object **(**whisker: $t(9)=3.3$, $p=0.009$; no whisker: $t(9)=0.07$, $p=0.9$; **Fig. 2b)**,

175 confirming the task requires active use of whiskers. *Wildtype* mice could discriminate between
176 the two objects, while *Syngap1*$^{+/-}$ mice could not **(**wildtype: t(7)=3.2, p=0.01; *Syngap1*$^{+/-}$: t(5)=-
177 0.7, p=0.5; **Fig. 2c)**. However, when the difference in texture pattern density between the
178 objects was greater (8 vs 5 instead of 9 vs 8 vertical ribs/cm, and presumably more perceptually
179 salient, both genotypes could now discriminate **(**wildtype: t(9)=3.5, p=0.007; *Syngap1*$^{+/-}$:
180 t(9)=3.6, p=0.005; **Fig. 2d)**. Additional object recognition testing was conducted, which
181 confirmed that poor texture discrimination in *Syngap1*$^{+/-}$ mice was caused by reduced tactile
182 sensitivity rather than a more generalized impairment in brain function and behavior. For
183 example, *Syngap1*$^{+/-}$ mice were able to discriminate equally well compared to littermate controls
184 in a traditional novel object recognition task that robustly engages multisensory processes
185 **(**wildtype: t(6)=2.9, p=0.02; *Syngap1*$^{+/-}$: t(9)=4.3, p=0.002; **Fig. 2e)**. Together, these data
186 demonstrate that *Syngap1* regulation of tactile sensitivity extends to texture discrimination.
187
188 In addition to texture discrimination, mice and rats actively use whiskers to perceive the location
189 of objects relative to their head [8,56,57]. To determine how *Syngap1* contributes to this form of
190 tactile perception, we utilized a head-fixed Go/NoGo object localization task[58]. In this task, mice
191 can use a single whisker to discriminate between two distinct object positions near the head
192 **(Fig. 3a)**. Water-restricted animals were trained to discriminate between the Go and NoGo
193 positions over ~28 daily sessions. Correct choices on Go trials (e.g., licking the sensor) were
194 reinforced with a water reward; FAs (licking on NoGo) resulted in a 15s timeout; misses (no
195 licking on Go) went unrewarded and unpunished. While *Syngap1*$^{+/-}$ mice learned to detect the
196 difference between the two locations, there was an effect of genotype, and an interaction
197 between genotype and sessions, on the fraction of correct choices and in the trial discrimination
198 index, *d'* **(Fig. 3b)**. To determine if impaired learning by mutants in this active tactile exploration
199 task was related to impaired sensitivity to detecting object location, we again performed a pull-
200 back experiment **(Fig. 3c)**. Statistical analysis revealed that performance was not the same

201 between genotypes at the end of training (fraction of total correct: $F(1,15) = 5.3$, $p=0.03$).
202 However, an interaction between genotype and object distance during pull-back sessions was
203 detected in total correct choices **(**$F(4, 60) = 2.6$, $p=0.04$, **Fig. 3d)**. Consistent with impaired
204 sensitivity (e.g., reduced precision) for detecting object location, the pull-back curve indicated
205 that performance dropped off faster in *Syngap1*$^{+/-}$ mice compared to wildtype littermates.
206
207 The motion of the whisker relative to an object is essential for determining object texture and
208 location [8,30,47,49]. Object contact causes whiskers to bend, eliciting torques and forces at the
209 whisker base that are proportional to changes in whisker curvature. Strain within the follicle
210 causes action potentials within trigeminal ganglion neurons. Therefore, reduced sensitivity for
211 texture and location in *Syngap1* mice may be related to abnormal whisker motion during object
212 exploration. To directly test this idea, we used a two-step approach that measured whisker
213 kinematics in the same animals with and without the presence of a stationary pole **(Fig. 3e, j)**.
214 Whisker dynamics were recorded using high-speed videography followed by offline location
215 tracking with *WHISK*[58] or DeepLabCut[59] (**Supplementary Fig. 2**, **Video S1**). There was no
216 effect of genotype on the setpoint ($t(34)=0.5$, $p=0.6$), maximum range of the whisker cycle
217 (protraction: $t(34)=1.1$, $p=0.3$; retraction: $t(34)=0.7$, $p=0.4$), or whisker velocity during free air
218 whisking **(**protraction: $t(28.2)=1.4$, $p=0.2$; retraction: $t(34)=0.39$, $p=0.7$, **Fig. 3f-i, Video S2)**,
219 indicating that *Syngap1* expression does not regulate whisker kinematics in the absence of
220 tactile input. We next quantified whisker dynamics in these same animals during whisking
221 against a stationary pole **(Fig. 3j; Video S3)**, a paradigm that approximates the sensing process
222 in the head-fixed pole localization task **(Fig. 3a)**. Physical interactions between the whisker and
223 pole during rhythmic whisking induced whisker curvature during individual touch episodes **(Fig.**
224 **3j-k)**. Each episode of whisker contacting the object (i.e., touch episode) was extracted from the
225 high-speed videos. Contact duration and whisker curvature for each touch episode was
226 calculated for both genotypes. We observed that touch episodes generated smaller changes in

whisker curvature in *Syngap1*$^{+/-}$ mice compared to *wildtype* controls **(**AUC: U=57, p=0.001; **Fig. 3k-l)**. Moreover, there was an effect of genotype on touch duration, with *Syngap1*$^{+/-}$ mice exhibiting shorter touch durations than *wildtype* controls **(**t(18.8)=2.6, p=0.02; **Fig. 3m)**. Finally, we categorized touches based on how they influenced touch-induced pumps (TIPs), a specific type of whisker dynamic where the animal purposefully holds the whisker on the pole and engages in a "pumping" behavior once the pole is perceived [60]. Importantly, TIPs elicit attention downstream of perception [50], and therefore this whisker kinematic provides a proxy measure of attention levels. We categorized all touches into four TIP categories based on amplitude and acceleration of the whisker while in contact with the pole **(Supplementary Fig. 3; Video S4**). In the category defined by >2 changes in amplitude and acceleration during pole contact, which includes the long-lasting touches with substantial levels of integrated curvature (and presumably long bouts of attention), we found that there were fewer of these touches in *Syngap1* heterozygotes compared to *wildtype* controls **(Fig. 3n-o, o:** U=239, p=0.01**).** Thus, this finding is consistent with impaired attention, reduced object exploration, and reduced tactile sensitivity in *Syngap1*$^{+/-}$ mice.

Syngap1 expression within cortical excitatory neurons promotes perceptual learning, touch sensitivity, and touch-induced changes to whisker motion:

Somatosensory systems are distributed throughout the brain and body. Thus, to gain mechanistic insight into the role of *Syngap1* expression on tactile sensing, we sought to identify the regional and cell-type origins of *Syngap1* expression sufficient to explain tactile phenotypes in this animal model. We hypothesized that *Syngap1* expression within higher-order brain areas may be sufficient to explain its role in both whisker dynamics and tactile learning. This theory was based on literature demonstrating that *Syngap1* is enriched in cortical areas [61,62], combined with separate literature indicating that touch engages top-down MSM loops, which dynamically tune whisker dynamics during sensing by signaling downward to brainstem motor neurons [30,63–

253 [65]. To do this, we utilized two established *Syngap1* mouse lines that conditionally regulate the
254 gene's expression in cortical glutamatergic neurons (e.g., *EMX1*+ neurons). One line enables
255 conditional heterozygosity within *EMX1*+ neurons during the mid-embryonic period (*EMX1-*
256 *Syngap1-OFF*), while the other embryonically re-activates *Syngap1* expression in a
257 heterozygous null background selectively within the EMX1+ population [66,67] (*EMX1-Syngap1-*
258 *ON*) **(Fig. 4a, Supplementary Fig. 4)**. We first assessed whisker kinematics **(Fig. 4b)**. No effect
259 of genotype was observed in free air whisking measures in either model **(Fig. 4c-e,**
260 **Supplementary Table4)**, which is consistent with a lack of phenotypes observed in germline
261 (whole body) *Syngap1*$^{+/-}$ mice **(Fig. 3h-l)**. However, during pole presentation **(Fig. 4f)**, *EMX1-*
262 *Syngap1-OFF* heterozygous mice largely phenocopied altered touch-induced whisker
263 kinematics originally observed in germline *Syngap1*$^{+/-}$ mice **(Fig. 4g-j; Fig. 3l-o)**. Touch
264 episodes were shorter and generated less curvature compared to *wildtype* littermates
265 (t(23.7)=3.3,p=0.003). In contrast, *EMX1-Syngap1-"ON"* heterozygous mice did not express
266 touch-regulated whisker motion phenotypes found in the other two models **(Fig. 4g-j, g:**t(35.9)=-
267 0.4,p=0.7**)**, even though *Syngap1* expression was only re-activated within EMX1+ glutamatergic
268 cortical projection neurons (e.g. thalamic, cerebellar, brain stem areas, as well as the rest of the
269 body, including all GABAergic neurons, remained heterozygous for *Syngap1* expression [60,61]).
270 This result demonstrates that *Syngap1* expression within EMX1+ neurons is necessary and
271 sufficient for regulating touch-induced changes to whisker kinematics during pole exploration.
272
273 *Syngap1* expression within cortical glutamatergic neurons was also necessary and sufficient for
274 promoting tactile sensitivity. For example, restricting *Syngap1* heterozygosity to cortical
275 excitatory neurons phenocopied germline heterozygosity in the WDIL paradigm – there was a
276 reduction in learning over the three-week training period in this task **(Fig. 4k,** F(19, 266) =
277 2.603, p<0.001**; Supplementary Fig. 5a**). In contrast, restricting *Syngap1* heterozygosity to all
278 cells in the body except cortical glutamatergic neurons (i.e., EMX1-*Syngap1-ON*) resulted in no

differences between genotypes in key measures of learning and trial discrimination **(Fig. 4l**, F(19, 133) = 0.5560, p=0.9**; Supplementary Fig. 5b).** Moreover, there was no effect of genotype in the pull-back portion of the study **(Fig. 4m,** F (5, 108) = 0.36, p=0.9**, Supplementary Fig. 5c),** demonstrating that detection sensitivity was normal in the EMX1+ rescue mice. Lack of phenotypes in the *Syngap1*-ON model was most likely driven by re-expression of *Syngap1* expression in the target neuron population (e.g., cortical excitatory neurons). This interpretation was supported by impaired pull-back sensitivity in non-Cre-expressing *Syngap1*-OFF mice compared to littermate controls **(Supplementary Fig. 5d-e)**. Indeed, these non-Cre expressing mice represent a distinct strain of *Syngap1* heterozygous knockout mice[66]. Thus, this result demonstrates reproducibility of the effect of *Syngap1* expression on tactile sensitivity. *EMX1-Syngap1-ON* mice were also tested in the NOR-T paradigm. Mice with *Syngap1* re-expressed in the EMX1+ population were able to discriminate between the two nearly identical textured objects **(**t(17)=2.4, p=0.03**; Fig. 4n, Supplementary Fig. 5f)**. Importantly, no unexpected germline deletion of LoxP sites[68] was observed in the *EMX1-Syngap1-ON* mice **(Supplementary Fig. 4)**, demonstrating that regulation of *Syngap1* expression was indeed restricted to the expected target population. Together, these data demonstrate that expression of *Syngap1* within cortical glutamatergic neurons is both necessary and sufficient to produce touch-driven whisker control during object exploration, tactile sensitivity, and perceptual learning.

***Disrupted Neuronal Dynamics within the somatomotor network of Syngap1+/- mice*:**

Given the autonomous role of *Syngap1* expression in cortex to sustain object exploration and associated perceptual learning, we hypothesized that neuronal dynamics within top-down MSM loops would be disrupted in *Syngap1*$^{+/-}$ mice. To directly test this, we measured unit spiking activity in higher-order whisker-related sensorimotor areas, including M1/M2, S1-BF, and whisker thalamus (VPM and POM areas), in *Syngap1* mice as they whisked in the presence or

305 absence of a stationary pole. Neuronal spiking activity was recorded simultaneously across
306 these regions in awake head-fixed *Syngap1*$^{+/+}$ and *Syngap1*$^{+/-}$ mice using multi-channel silicon
307 probes **(Fig. 5a-d, Supplementary Fig. 6-8)**. During the two-hour recording period, lighting,
308 auditory white noise, and the presence of a pole were varied to provide animals with a diverse
309 sensory experience. After habituation, there was no difference in the amount of running on the
310 treadmill during the recording **(Supplementary Fig. 8b)**. Across the three brain areas, there
311 was no difference in the number of multiunit activity (MUA) clusters extracted from the two
312 genotypes during electrophysiological recordings **(Supplementary Fig. 7b)**. In addition, there
313 was no effect of genotype on the mean peak MUA spike rate in any of the three brain areas
314 when activity was averaged for the entire recording period **(Fig. 5e)**. This suggests that the
315 absolute level of ongoing spiking activity within the somatomotor network over prolonged time
316 periods is not changed in head-fixed *Syngap1* mice.
317
318 Periods of free-air whisking and pole exploration represented only a fraction of the total time
319 during the recording session. Therefore, we hypothesized that genotype-specific changes in
320 neural activity would emerge during specified behavioral epochs defined by whisking with and
321 without the pole present. Discrete free whisking (no pole) and touch (pole present) events were
322 identified from high-speed video recordings **(Video S1).** These events represent two distinct
323 behavioral transitions – from stationary to self-generated whisker movement **(whisking –**
324 **VideoS2)** and from self-generated whisker motion to object contact inducing curvature **(touch –**
325 **Video S3)**. We identified whisking and/or touch responsive MUA clusters in each brain area
326 from both genotypes **(Fig. 5f)**. In animals from both genotypes, the dynamics of spike rate
327 modulation were distinct in MUA clusters during free whisking compared to touch, and these
328 patterns of activity agreed with past studies using similar recording techniques[69]. For example,
329 free-air whisking units displayed prolonged activity on the order of hundreds of milliseconds,
330 while touch-responsive units displayed activity for much shorter periods of time **(Video S5)**.

331 Distinct unit modulation associated with free whisking and touch is consistent with the unique
332 time scale of the two behaviors. Free whisking bouts were variable, though they usually lasted
333 for hundreds of milliseconds and beyond[70], while individual touches were generally an order of
334 magnitude faster, with 80% of touches lasting less than 50ms **(Fig. 3m and 4h;**
335 **Supplementary Fig. 8c)**.
336
337 The extraction of units modulated by whisker motion and/or touch allowed us to explore neural
338 dynamics within and across the three regions of the somatomotor cortex as animals whisked
339 with and without the pole present. We first quantified communication between neural
340 populations by estimating the dimensionality of a subspace in the source population that best
341 predicts activity in a target population[71]. We did this to test the hypothesis that *Syngap1*
342 haploinsufficiency generally impairs the function of the somatomotor network during periods of
343 active tactile exploration. Specifically, we identified a subspace within the source region's neural
344 activity that optimally predicts the activity in the target region. The dimensionality of this
345 subspace serves as a measure of how many neural dimensions are involved in the
346 communication between the two regions **(Fig. 5g)**. In *Syngap1*$^{+/-}$ mice, the analysis of neural
347 communication across neural populations revealed a significant increase in predictive
348 performance, particularly in cross-area interactions during whisking (**Fig. 5h-i**).
349 A significant increase in 1-NMSE was observed specifically in the S1 to M1 region pair in
350 mutants, indicating that the neural activity in S1 is more predictive of M1 activity compared to
351 wildtypes. This enhanced predictive accuracy suggests that there may be altered functional
352 connectivity between S1 and M1 in *Syngap1*$^{+/-}$ mice. The trend of increased predictive
353 performance from S1 to M1 in *Syngap1* mutants during whisking was also consistent across
354 behavioral epochs, though not all were statistically significant. This increased accuracy was not
355 accompanied by statistically significant changes in subspace dimensionality, although there was
356 a consistent trend toward greater dimensionality in the mutants, particularly in cross-regional

interactions. This pattern was observed across different behavioral conditions, with a more pronounced effect during inactive epochs and a subtler, though present, trend during touch **(Supplementary Figure 6)**. These findings indicate that the *Syngap1* mutation may have a broad impact on the thalamocortical communication network, affecting both the strength and structure of inter-regional neural interactions.

Features of neuronal spiking activity within nodes of the somatomotor network

To begin to understand how neuronal dynamics are altered in *Syngap1* mice, we next explored unit spiking properties across all three regions during whisking events with and without the presence of the stationary pole. Measuring spike rate modulation during the two distinct behaviors revealed numerous measures with genotype effects **(Fig. 6a, Supplementary Table 6)**. In general, motor signals associated with free whisking were significantly increased in *Syngap1*$^{+/-}$ compared to *Syngap1*$^{+/+}$ mice. Furthermore, the increase in motor activity during free whisking observed in M1 of *Syngap1*$^{+/-}$ mice was also present in S1 and thalamus, with thalamus resembling M1 **(Fig. 6a)**, while S1 MUAs demonstrated a less notable increase in activity compared to that observed in M1 and thalamus **(Fig. 6a)**. Together, these findings demonstrate that *Syngap1* mice have a generalized increase in whisker motor signals within MSM network nodes.

In contrast, touch-related activity was generally decreased across these three regions in *Syngap1* mutants **(Fig. 6b)**. Analysis of MUA cluster dynamics during all touch events revealed significantly reduced peak spike rates in *Syngap1*$^{+/-}$ relative to *Syngap1*$^{+/+}$ mice. The general finding of reduced activity across the tactile-motor loop during touch in *Syngap1* mutants is consistent with our findings of reduced curvature of the whisker during individual object touches in animals with reduced expression of *Syngap1* **(Fig. 3l; Fig. 4g)**. In addition to abnormalities in peak spike rates, there was a clear disparity in the temporal onset of spiking in response to

383 touch in mutants relative to wildtype littermate controls **(Fig. 6b)**. Unit dynamics in *Syngap1*$^{+/-}$
384 mice appeared to be low-pass filtered compared to wildtype littermates. In the thalamus, peak
385 touch-dependent modulation was delayed, while duration of touch-related activity was
386 prolonged in *Syngap1*$^{+/-}$ mice compared to wildtypes **(Fig. 6b)**. In M1/M2, a biphasic response
387 was noted in wildtypes, with a rapid initial peak of activity occurring in response to object touch
388 **(Fig. 6b)** and a secondary peak occurring 10-20ms later, which likely reflects recurrent activity
389 arriving from other brain areas. In contrast, the initial peak after touch was reduced in
390 *Syngap1*$^{+/-}$ mice, while the delayed responses appeared intact. Importantly, we observed
391 reduced touch-induced spiking within S1-BF integrator units of *Syngap1* mutants, which
392 responded to both whisker motion and pole-touch **(Supplementary Fig. 8e)**.
393
394 Reduced touch-related activity in units from *Syngap1*$^{+/-}$ mice could be a consequence of
395 reduced psychomotor properties of the whisker during pole exploration (e.g., reduced average
396 curvature during touch episodes). However, we have reported previously that controlled whisker
397 curvature induced by passive whisker deflections results in reduced calcium-related neuronal
398 activity in S1-BF from *Syngap1* mutants[23]. Thus, it is also possible that *Syngap1*$^{+/-}$ somatomotor
399 networks may encode fewer spikes per unit of curvature. To resolve these two possibilities, we
400 clustered all touch events into four categories based on integrated total whisker curvature in
401 response to pole contact (e.g., “small”, “medium”, “large”, and “extra-large” levels of curvature).
402 When categorized this way, there was no difference in curvature between the genotypes within
403 any of the four touch categories **(Fig. 6c)**. As a result, touch-responsive units could now be
404 compared between genotypes in the context of similar average levels of curvature. When unit
405 activity was reanalyzed across the four touch categories in each genotype, surprising results
406 were obtained. In wildtype mice, the expected positive correlation between curvature category
407 and average peak spike rate in all three brain areas was present **(Fig. 6d)**. However, in
408 *Syngap1*$^{+/-}$ mice, this relationship was essentially inverted. For example, there was a clear

409 negative correlation between the magnitude of average curvature and average unit spike rate in
410 both S1-BF and thalamus. Indeed, in S1-BF, touches that generated the greatest whisker
411 curvature had the least amount of associated unit activity **(Fig. 6c-d)**. Taken together, touch
412 elicits weak and temporally altered spiking activity in units from all three somatomotor areas in
413 *Syngap1* mutants, while units that responded to whisking exhibited enhanced activity in these
414 same areas.
415
416 **Circuit pathologies within higher-order somatomotor network hubs in *Syngap1* mice**
417 Given the observed somatomotor network dysfunction in these mice, we hypothesized that
418 dysfunction arises in part through abnormal structure and/or function of specific circuits
419 connecting nodes within this network. We chose to probe inputs onto somatosensory cortex
420 (S1) neurons for three reasons. First, abnormal connections through S1 were disproportionally
421 identified in the communication subspace analysis **(Fig. 5g-i; Supplementary Figure 6)**.
422 Second, neurons in this region are known to integrate motor and touch signals required for
423 perception [47,72,73]. Third, within S1, *Syngap1* regulates dendritic morphogenesis in deep
424 neurons[74] and developmental synaptic connectivity of feed-forward excitation in upper lamina
425 neurons[23], which could lead to circuit connectivity alterations capable of influencing neuronal
426 dynamics within this cortical area. To test this idea, a cell-type specific rabies virus (RBV)
427 monosynaptic retrograde labeling technique[75] was performed to trace brain-wide synaptic
428 connectivity onto L5 S1 neurons in *Syngap1*$^{+/+}$ and *Syngap1*$^{+/-}$ mice **(Fig. 7a-c)**. We achieved
429 regional and neuronal subtype selectivity by crossing *Syngap1*$^{+/-}$ mice to RBP4-Cre mice and
430 then injecting viral vectors directly into S1 of adult mice. Traced neurons within anatomically
431 defined brain areas were registered and quantified[76] **(Supplementary Fig. 9a-d)**. The location
432 of helper and rabies virus injections within L5 S1 was similar across all animals of both
433 genotypes and a similar number of sections from each group was analyzed **(Supplementary**
434 **Fig. 9e-h)**. Importantly, no difference between genotypes was observed in the number of double

435 labeled L5 S1 starter cells (t(12)=-0.6,p=0.6) and there was a similar number of inputs (t(12)=-
436 0.8,p=0.4); e.g., number of eGFP-only neurons outside L5 S1) relative to the starter cell
437 population **(Supplementary Fig. 9i-j)**. This indicated that the total long-range synaptic
438 connectivity onto L5 S1 neurons was not different between genotypes, which agrees with prior
439 data demonstrating no alteration in spine density of L5 S1 at PND60 in *Syngap1*$^{+/-}$ mice[74].
440
441 We quantified relative connectivity onto L5 S1 neurons for all brain regions and observed a
442 difference only for motor cortex (M1/M2) inputs **(**t(12)=-2.5, 0.03, **Fig. 7d-f)**. Grouping neurons
443 within cortical origins across the antero-posterior axis revealed a genotype effect **(Fig. 7g,** Ctx-
444 >S1/L5, F(1,13)=6.6,p=0.01**)**. The genotype effect of afferent cortical connectivity onto L5 S1
445 neurons was driven by changes in motor cortex areas. Indeed, we observed an increase in
446 eGFP-labeled neurons in M1/M2, but not other cortical areas, in *Syngap1*$^{+/-}$ mice compared to
447 *wildtype* controls **(Fig. 7d-f)**. Moreover, when neurons originating from motor areas were
448 removed from the "cortex" cluster, this difference was no longer significant **(Fig. 7g,** Ctx-M-
449 >S1/L5, F(1,13)=6.6,p=0.01**)**. Furthermore, the increased M1/2 labeling in *Syngap1*$^{+/-}$ mice was
450 driven largely by neurons in deeper layers **(Fig. 7g,** M1/L2-3->S1/L5 and M1/L5->S1/L5**)**. Thus,
451 this unbiased screen of synaptic connectivity onto L5 S1 neurons revealed an increase in inputs
452 arriving from motor cortex. Other connections may also be impacted in these mice, through
453 these other regions did not reach levels of statistical significance.
454
455 To assess the validity of the significantly elevated motor-to-somatosensory cortex synaptic
456 connectivity reported by RBV retrograde transsynaptic tracing, we measured the function of this
457 input in *Syngap1* mice. An opto-probe was inserted into motor cortex of *Thy1*-ChR2 mice, which
458 expresses ChR2 selectively within L5 neurons[77]. A single-channel electrode was lowered into
459 L5 of S1 to record field potentials **(Fig. 7h).** Optogenetic activation within M1/M2 resulted in a
460 biphasic waveform **(**WF1, WF2; **Fig. 7h-j)**. TTX injection into the thalamus had an outsized

461 impact on WF2 compared to WF1 **(Fig. 7j)**. Given that WF1 occurred within a few milliseconds
462 of the stimulus, these data together indicated that the early peak most likely reflects
463 monosynaptic connections from M1/M2 to S1, while the later peak may reflect a multi-synaptic
464 loop, such as the M1/2 > Thalamus > S1 loop. In a different set of experiments, a single-channel
465 electrode was placed in L5 of S1 to record field potentials induced by ChR2+ in either wildtype
466 or heterozygous *Syngap1* mice **(Fig. 7k-m)**. We observed an increase in WF1 in *Syngap1*
467 mutants relative to littermate controls **(Fig. 7k-m,** at 60mW/mm^2: t(5.6)=-3.4,p=0.01**)**, which was
468 consistent with the RBV retrograde tracing results. Moreover, long-range functional
469 hyperconnectivity of M1/2 > S1 in *Syngap1* mice was not generalized, but was rather somewhat
470 selective. In contrast to M1/M2 inputs to L5 of S1-BF, whisker deflections, which drive
471 peripherally generated activity that arrives in S1 through thalamic feed-forward excitation,
472 resulted in *smaller* synaptic responses in L5 S1 from *Syngap1*$^{+/-}$ mice compared to wildtype
473 littermates **(**F(1,11)=16.2,p=0.002, **Fig. 7n-o)**. Together, these data demonstrate that L5
474 neurons in S1 of *Syngap1* mice receive a relatively strong input from M1/M2, a connection that
475 relays whisker motor signals [30,72], but relatively weak afferent thalamocortical connectivity, an
476 important connection that transmits whisker-touch signals into cortex. These circuit-specific
477 impairments are consistent with abnormal dynamics within the somatomotor network as animals
478 explore the environment using whiskers **(Fig. 5g-i).**
479

480 **Discussion**

481 The molecular and cellular mechanisms that link SMI in higher brain regions to cognitive
482 constructs that support adaptive behavior, such as attention and perception, are poorly
483 understood. The motivation behind this study was to investigate the relationships
484 between neurobiological correlates of SMI that promote cognitive functions and genetic factors
485 associated with intellectual abilities. Here, we investigated how a gene strongly associated with
486 sensory processing, cognitive ability, and autism risk, *Syngap1,* regulates sensorimotor

487 processes in the cortex that support perception and attention. To understand how *Syngap1*
488 contributes to SMI, we independently investigated how it contributes to sensory and motor
489 processing underlying tactile sensing with whiskers. We also investigated the role of this gene
490 directly in SMI through combined behavioral and electrophysiological observations during active
491 whisker touch. Together, these data converged on a model where *Syngap1* promotes tactile
492 perception and associated behavioral reactivity by assembling circuits that initially represent
493 touch in the cortex. These circuits also integrate touch signals with whisker motor signals to
494 promote an understanding of object features, such as location and texture, as well as eliciting
495 attention. Our results indicate that *Syngap1* expression promotes assembly of cortical circuits
496 that enable sensorimotor processing crucial for cognitive functions, including perception and
497 attention. Thus, *SYNAGP1*/*Syngap1* haploinsufficiency may degrade intellectual ability by
498 disrupting the function of a cortical sensorimotor network required to engage these cognitive
499 processes.
500
501 Initially, we established that *Syngap1* loss-of-function leads to behavioral *hypo*-sensitivity when
502 sensing with whiskers, which is expressed across tactile domains, including detection
503 sensitivity, texture discrimination, and object localization **(Fig. 8a)**. These mouse studies are
504 consistent with reports of tactile hyposensitivity and very high pain thresholds in *SYNGAP1-DEE*
505 patients, including impaired behavioral reactivity in response to external stimuli applied to the
506 body [23,78]. Importantly, similar to the mouse model, this human patient population is defined by
507 heterozygous loss-of-function variants within the *SYNGAP1* gene. Second, we found that
508 *Syngap1* expression in cortical excitatory neurons is both necessary and sufficient for setting
509 tactile detection thresholds that drive perception and associated adaptive behaviors **(Fig. 3)**. For
510 example, well-trained *Syngap1* mutant mice made more perceptual errors relative to wildtype
511 littermates in a subset of trials designed to measure tactile sensitivity. This suggested that poor
512 learning in the tactile domain displayed by *Syngap1* mice may be explained, in part, through

513 reduced whisker sensitivity. This phenotype was caused by its expression in cortical excitatory
514 neurons because perceptual errors associated with whisker stimulus detection sensitivity were
515 phenocopied in a mouse model with reduced *Syngap1* expression restricted to this population.
516 Furthermore, when SynGAP protein was re-expressed in cortical excitatory neurons within
517 *Syngap1* heterozygous mice, perceptual errors linked to whisker sensitivity were no longer
518 present. A similar rescue of texture discrimination was observed in the *Syngap1* cortex-specific
519 re-expression model. These findings, when integrated with past studies of other NDD risk
520 factors, highlight the principle that individual genes can either promote or suppress neural
521 mechanisms that dictate tactile sensitivity. Several NDD genes, such as *Shank3*, *Mecp2, and*
522 *Fmr1* have been shown to regulate tactile sensitivity [19,79]. However, for these risk factors, gene
523 loss-of-function was linked to tactile *hyper-*sensitivity rather than *hypo*-sensitivity, which was
524 explained by either cell-autonomous expression within the peripheral nervous system or in the
525 CNS [19,22,80–82]. Moreover, these studies focused on behavioral reactivity, and therefore did not
526 link risk gene expression to neural correlates of cognitive constructs. The uniqueness of
527 *Syngap1* with respect to tactile sensitivity in the context of these mouse studies is important
528 because tactile hyposensitivity is also relatively common in NDD populations, including ASD
529 [26,80,83–86]. Thus, *Syngap1* mouse lines are emerging as genetic tools useful for elucidating the
530 neural correlates linking NDD-associated sensory sensitivity to cognitive functions underlying
531 adaptive behavior. In line with this, subsequent experiments in this study were aimed at
532 understanding the potential neurobehavioral and neurophysiological correlates linking tactile
533 hyposensitivity driven by *Syngap1* loss-of-function to impaired cognitive constructs.
534
535 Subsequent experiments led to a framework where *Syngap1* function within cortical
536 glutamatergic neurons promotes tactile sensitivity through coding of touch signals in cortical
537 somatomotor networks **(Fig. 8b)**. Several lines of evidence support this framework. *First*,
538 impaired responses to passive whisker stimuli within cortical somatomotor areas of *Syngap1*

539 mice is consistent with weak perceptual learning and reduced tactile sensitivity in the passive
540 WDIL task. Our past studies have demonstrated that passive whisker deflections, the stimuli in
541 WDIL, are weakly registered in barrel cortex of *Syngap1* mice, and this neurophysiological
542 observation was dependent on *Syngap1* expression in the EMX1+ population [23]. In that prior
543 study, we noted that increased stimulus intensity of the whisker input in *Syngap1* mice caused
544 larger deficits in barrel cortex activity compared to wildtype littermates. Whereas increasing
545 stimulus intensity in wildtype mice led to larger cortical activation, this input/output relationship
546 was impaired in *Syngap1* mice. Similarly, in this current study, we found that increasing the
547 intensity of the stimulus during WDIL training induced more robust learning in wildtype mice.
548 However, in *Syngap1* mutant mice, this was not the case. Increasing the stimulus intensity in
549 these animals did not generate proportionally better learning as it did in wildtype, which led to
550 qualitative differences in learning between genotypes **(Fig. 1)**. Thus, in these mice, there is a
551 clear correlation between weak somatosensory cortex responses to passive whisker deflections
552 and weak learning related to this same stimulus. Importantly, both behavioral reactivity to **(Fig.**
553 **4)**, and cortical representations of [23], the passive whisker stimulus are dependent upon *Syngap1*
554 expression in cortical glutamatergic neurons.
555
556 *Second,* we observed abnormal touch-induced whisker exploratory behavior in *Syngap1* mice
557 **(Fig. 2-3)**, including a reduction in the frequency and duration of touch-induced pumps (TIPs).
558 This phenotype is also consistent with poor touch coding within cortical sensorimotor networks.
559 Touch coding within higher-order motor-sensory-motor (MSM) loops is believed to generate
560 touch-induced changes to whisker kinematics observed during active tactile sensing [30,60,64,70].
561 Tactile signals representing initial object touch are believed to engage higher-order circuits that
562 support constructs of cognition, such as attention [60,70,87]. This leads to a shift in whisker sensing,
563 with motion directed toward focused object exploration by the animal, which includes prolonged
564 and purposeful object contacts that generate high levels of whisker curvature (e.g., TIPs). Thus,

weak higher-order registration of initial object contacts in cortical networks is consistent with disrupted touch-induced whisker kinematics during object exploration. According to the existing model, touch signals in higher-order sensorimotor loops trigger prolonged object interactions by altering the function of whisker motor circuits in the brainstem, which is a neural correlate of attention [30,64,65]. In support of this theory, we observed normal whisker kinematics in *Syngap1* mice during free-air whisking. Altered whisker kinematics were observed only when animals were presented with the stationary pole. This result would infer that the *Syngap1* expression in higher brain areas may be required to sustain object exploration by linking touch signals to attentional processes. This theory was additionally supported by the finding that *Syngap1* expression within the cortical excitatory neuron population is both necessary and sufficient for touch-induced changes to whisker kinematics **(Fig. 4)**. Therefore, *Syngap1* expression likely regulates neurobiological processes within this restricted neuronal population to promote integration of touch signals into attentional circuits that modulate whisker motor neurons in the brainstem. One possible cellular mechanism may involve the regulation of connectivity and/or function of cortical excitatory neurons that both code for touch and signal to brainstem neurons that drive whisker motion. This possibility was supported through our electrophysiological observations of reduced touch responses in units within higher-order somatomotor loops from *Syngap1* mutants **(Fig. 5)**. Future studies will be necessary to determine the extent to which *Syngap1* expression regulates touch-responsive neurons in the cortex that project to brainstem whisker motor circuits.

Third, we observed weak touch responses during pole exploration across higher-order somatomotor areas in *Syngap1* mice, including somatosensory and motor cortex, as well as whisker areas in thalamus **(Figs. 5-6)**. In these mutant animals, weak touch responses were present in the context of an increase in temporally-overlapping whisker motor signals. This sensorimotor imbalance reflected a real change in the signal-to-noise ratio of neurons that

591 integrate touch with whisker motion. Importantly, we observed weak whisker touch responses in
592 neurons from the barrel region of somatosensory cortex that also respond to whisker motion.
593 This is a direct electrophysiological demonstration of altered SMI within the cortex of *Syngap1*
594 animals. Reduced signal-to-noise for touch/motor integration is consistent with impaired object
595 localization. Object localization is thought to be computed, in part, through convergent whisker
596 touch and motor signals that are integrated within cortical sensory and motor areas [30].
597 Electrophysiological correlates of reduced touch coding, as well as correlates of enhanced
598 motor signals, were supported by circuit tracing and subsequent functional circuit validation
599 studies in *Syngap1* mice. *Syngap1* mice had hyper-functional inputs from motor cortex that
600 project to Layer 5 somatosensory cortex **(Fig. 7)**. These mice also possess a weak subcortical
601 input that transmits touch signals into L5 somatosensory cortex.
602
603 It is unclear how reduced *Syngap1* expression in mice can cause impaired cortical touch
604 representations, while also causing enhanced whisker motor representations. Understanding
605 this dichotomy will provide insight into the neural correlates of impaired sensorimotor processing
606 in NDDs. *Syngap1* expression may exert unique cell-autonomous functions within neuronal
607 subtypes that comprise the EMX1+ population. Unique, cell-autonomous functional control over
608 expression of neuronal features that directly assemble and refine circuits could lead to
609 unpredictable circuit-specific impairments, not unlike what was observed in this current study.
610 This hypothesis is supported by evidence in past studies demonstrating that *Syngap1* potently
611 regulates cellular substrates of circuit assembly and refinement, such as dendritic
612 morphogenesis, synaptic maturation, and cell/circuit-level forms of neural plasticity [88].
613 Intriguingly, *Syngap1* regulates circuit-building substrates in a cell- and region-specific manner,
614 sometimes in opposite directions. For example, it can both promote[74] and constrain[23] dendritic
615 morphogenesis within distinct EMX1+ neuronal subtypes during developmental critical periods.
616 Pertinent to this current study, the developmental maturation of L5b tufted neurons in

617 somatosensory cortex is greatly accelerated in *Syngap1* mutant mice. These *Syngap1*-deficient
618 neurons reach adult-like features of maturation weeks before similar neurons in wildtype
619 littermates [74]. This accelerated maturation spans major morphogenic developmental milestones,
620 including accelerated dendritic differentiation, early acquisition of dendritic spines, and
621 subsequent precocious spine pruning. In contrast, in this same model, and within the same
622 brain area (somatosensory cortex), the development of L2/3/4 upper-lamina neurons feature
623 arrested development [23]. Altered maturation of neurons in cortex is not restricted to
624 somatosensory cortex [74]. De-synchronization of postmitotic dendritic and synaptic maturation
625 across distinct neuronal subtypes and regions is consistent with impaired somatosensory
626 network function observed in this study.
627
628 Significant mechanistic questions remain unanswered. One such area of exploration is to
629 understand to what extent somatomotor system organization, such as local excitatory and
630 inhibitory microcircuit connectivity or long-range connectivity among network hubs, is dictated
631 directly (e.g., cell-autonomously) by *Syngap1* expression within distinct cellular subtypes. The
632 challenge will be to then contrast this with indirect (e.g., non-cell autonomous/homeostatic)
633 compensatory consequences that are engaged because of the direct cell-autonomous changes
634 to neuronal structure and function downstream of *Syngap1* heterozygosity. This framework may
635 help to explain the unexpected current result that M1/M2 excitatory projections to S1 exhibited
636 outsized levels of hyperconnectivity compared to excitatory inputs originating from other brain
637 areas. With regards to the cellular building blocks of cortical circuits, they can be broken down
638 into nested categories, including neuronal vs. non-neuronal cells, excitatory vs. inhibitory
639 neurons, or subclasses of excitatory (PT, IT) and inhibitory (PV, SOM) neurons. The current
640 study provides evidence that cell-autonomous expression of *Syngap1* within cortical excitatory
641 neurons is both ***necessary*** and ***sufficient*** for touch perception and touch-associated behavioral
642 adaptations that require perception and attention. How these behavioral phenotypes relate to

643 circuit assembly errors among different subclasses of excitatory neurons remains unknown. For
644 example, accelerated maturation of L5 somatosensory cortex neurons[74] in *Syngap1*$^{+/-}$ mice
645 could be a non-cell-autonomous compensatory process driven by arrested development and
646 hypofunction of upper lamina excitatory neurons in the same cortical area[23].
647
648 It is also possible that cell-autonomous functions of *Syngap1* within inhibitory neurons may also
649 play a role in the organization of the somatomotor system. Kwon et al[52] recently reported that
650 conditional knockdown of *Syngap1* within inhibitory neurons caused an impairment in
651 performance during a similar whisker-dependent Go/NoGo task. However, genotype effects
652 were detected for False Alarm responses, but not Hit responses. Because False Alarms may
653 reflect impulsive responding, while Hits reflect a learned association between the whisker
654 stimulus and the reward, these past results suggest that expression of *Syngap1* within inhibitory
655 neurons may be restricted to motor control processes. Moreover, that study did not assess
656 sufficiency of *Syngap1* within the inhibitory population. In our current study, manipulating
657 SynGAP protein expression in cortical excitatory neurons essentially phenocopied observations
658 in the germline heterozygous model. Integrating results from this past study with our current
659 results indicate that there are autonomous roles for *Syngap1* in both excitatory and inhibitory
660 cortical neurons, though whisker touch perception and attention is largely shaped by the
661 function of the gene within the excitatory population. Regarding non-neuronal cell types,
662 SynGAP is expressed in rodent astrocytes, but to lesser extent compared to neurons[51]. There
663 are reports of sparse Cre activity in isolated astrocytes in the *Emx1*-Cre mouse line[67], so it is
664 theoretically possible that *Syngap1* expression in astrocytes could contribute to phenotypes
665 observed in this study. However, we have empirically observed only a handful of glia that
666 express a Cre reporter cassette in the EMX1-Cre mouse line (G.R., *unpublished observations)*,
667 suggesting that cell-autonomous functions of *Syngap1* in astroglia may not substantially
668 contribute to somatomotor/perceptual phenotypes. Future studies leveraging intersectional

genetic perturbations that target *Syngap1* expression within defined cellular subtypes, across various brain areas, and across developmental epochs, will be necessary to tease out the direct vs. indirect effects of *Syngap1* on cellular elements that build top-down somatomotor network loops. Furthermore, given the recent genome-wide linkage of *SYNGAP1* to cognitive function[41], it will be important determine to what extent *Syngap1* gain-of-function in animal models[89] can enhance cognitive functions, and if so, how this might be achieved through altering neuronal dynamics within sensorimotor networks.

Data availability

The data that support the findings of this study are available from the corresponding author upon reasonable request.

Code availability

Custom code was written in Matlab, R and Python for data analysis. Codes which are not already available in public repository (see Methdods) are available upon reasonable request.

Acknowledgements

This study was supported by funding provided by NIMH (MH096847) and NINDS (NS110307) to G.R./C.A.M and G.R. (w/D.O. as CO-I), respectively. We thank Gogce C. Crynen, PhD, Director of the UF Scripps Biostatistics Core, for consultation on appropriate application of statistical models to complex data sets. L. F. is supported by funding from Excellence Initiative of Aix Marseille Université - A*MIDEX (Turing Centre for Living Systems). We would like to thank Dakota Roberts, Stephanie A. Miller and Izan Gonzalez Fayos for technical assistance with histology and tissue processing.

Author Contributions

T.V and S.D.M. performed experiments, designed experiments, analyzed data, co-wrote the manuscript, and edited the manuscript. T.C. performed experiments, designed experiments, analyzed data, and edited the manuscript. D.F. and D.B. analyzed and interpreted data. L.F. designed experiments, analyzed data, interpreted data, and edited the manuscript. C.R. performed experiments, designed experiments, and generated reagents. R.G. designed experiments and generated data. K.M. provided key reagents and interpreted data. C.A.M secured funding, designed experiments, interpreted data, and edited the manuscript. D.O. designed experiments, interpreted data, edited the manuscript. G.R. conceived the study, secured funding, designed experiments, interpreted data, co-wrote the manuscript, and edited the manuscript.

Declaration of Interests

The authors declare no competing interests.

---------END--------

711 **MAIN Fig. Legends** (<1150 words)

712

713 **Fig. 1. *Syngap1* expression promotes perceptual learning (tactile sensitivity) during passive tactile**
714 **stimulus (WDIL). a.** Schematic of the whisker-dependent instrumental learning paradigm (WDIL),
715 including single whisker detection task structure and response outcomes with go trials being
716 discriminated by single whisker deflection for 3 different whisker stimulus intensities (~ 400, 650 and 900
717 º/s). During the WDIL task there was no auditory cue. The noise generated by the piezo during the Go
718 and NoGo trial was masked by a 70dB white noise. The **b.** Fraction of total trials correct during WDIL for
719 3 different whisker stimulus intensities: ~400º/s (wt: blue, n=9 and *Syngap1*$^{+/-}$: +/-, red, n=10), 650º/s (wt:
720 blue, n=7 and *Syngap1*$^{+/-}$: +/-, red, n=7) and 900º/s (wt: blue, n=8 and *Syngap1*$^{+/-}$: +/-, red, n=8). **c.**
721 Summary schematic of the training phase and the reduced stimulation phase. **d.** False alarm (FA) and hit
722 rates for animals that reached criteria and underwent the reduced stimulation phase (pull back) for
723 wildtype (wt: blue, n=6) and *Syngap1*$^{+/-}$ (+/-: red, n=6). Number of animals per genotype is indicated in
724 parentheses. Shaded areas represent the standard error of the mean (S.E.M.). p-value for main effects
725 and interaction are indicated as n.s.: p>0.05, *: p<0.05, **: p<0.01, ***: p<0.001 detailed statistics are
726 provided in Supplementary Table1.

727

728 **Fig. 2. *Syngap1* expression promotes perceptual learning (tactile sensitivity) in ethologically**
729 **relevant active sensing paradigms. a.** Novel object recognition texture (NOR-T) task structure in which
730 mice are tasked to discriminate between visually identical objects having either 8 or 9 verticals ribs/cm.
731 The light level in the arena is 85 lux. **b.** Exploration time and discrimination index during the testing phase
732 of the NOR-T for wild-type animals performing the task with (n=10) or without whiskers (n=10) for objects
733 with 1 verticals ribs/cm difference. **c.** Exploration time and discrimination index during the testing phase of
734 the NOR-T for wild-type (wt: blue, n=8) and *Syngap1*$^{+/-}$ (+/-: red, n=6) for objects with 1 verticals ribs/cm
735 difference. **d.** Exploration time and discrimination index during the testing phase of the NOR-T for wild-
736 type (wt: blue, n=10) and *Syngap1*$^{+/-}$ (+/-: red, n=10) for objects with 3 verticals ribs/cm difference. Mice
737 with at least 10 sec of cumulative object exploration in the NOR-T were included in the analysis **e.** Novel
738 Object Recognition (NOR) task structure with exploration time and discrimination index during the testing

phase of the NOR for 2 different objects: a stapler and a lock in wild-type (wt: blue, n=7) and *Syngap1*$^{+/-}$ (+/-: red, n=10). Mice with at least 30 sec of cumulative object exploration in the NOR were included in the analysis. Number of animals per genotype is indicated in parentheses and in white within the bar graph. Error bars represent the standard error of the mean (S.E.M.). P-value are indicated as n.s.: p>0.05, *: p<0.05, **: p<0.01, ***: p<0.001. Detailed statistics are provided in Supplementary Table2.

Fig. 3. *Syngap1* expression promotes perceptual learning (tactile sensitivity) in a whisker-dependent discrimination task during instrumental learning based on pole location. a. Schematic of the behavioral paradigm during instrumental learning based on pole location. The pneumatic lift provided by the pneumatic linear slide also generates a sound that is not covered by the white noise and serves as an audio cue. **b.** Fraction of total trials correct, false alarm (FA) rate, Hit rate and d' during the acquisition phase of the pole-location discrimination task. **c.** Schematic of the reduced stimulation phase of the pole-location discrimination task. Wildtype (wt: blue, n=9) and *Syngap1*$^{+/-}$ (+/-: red, n=8) **d.** Fraction of total trials correct, false alarm (FA) rate, Hit rate and d' during the reduced stimulation phase of the pole-location discrimination task. Wildtype (wt: blue, n=9) and *Syngap1*$^{+/-}$ (+/-: red, n=7). Number of animals per genotype is indicated in parentheses. Shaded areas represent the standard error of the mean (S.E.M.). P-value for main effects and interaction are indicated as n.s.: p>0.05, *: p<0.05, **: p<0.01, ***: p<0.001. **e-i.** Whisker dynamics in free air and during object exploration. Superimposition of 40 frames representing whisking in wt mouse acquired at 500Hz illustrating free whisking of a single whisker, scale bar = 5mm **(e)**. Representative traces of whisker angle in wt (blue) and *Syngap1*$^{+/-}$ (red). Quantification of whisker setpoint **(g)**, amplitude **(h)** and velocity **(i)** of the protraction (prot.) and retraction (ret.) whisking phase during a 30 second recording window. **j-o.** Active touch dynamics of a single whisker for the first 30 seconds of pole presentation, superimposition of 40 frames representing active touch, scale bar = 5mm **(j)**. Representative traces of whisker curvature **(k)** and quantification of area under the curve (AUC) for whisker curvature **(l)**, average touch duration **(m)** and the total number of peak protractions detected for each individual touch event for wild-type (wt: blue, n=1144) and *Syngap1*$^{+/-}$ (+/-: red, n=1541) **(n)** and their respective animal average **(o)**. Error bars represent the standard error of the mean (S.E.M.) and number of animals for wild-type (wt: blue, n=17) and *Syngap1*$^{+/-}$ (+/-: red, n=19) is also indicated in white within

767 the bar graph and/or in parentheses. P-value are indicated as n.s.: p>0.05, *: p<0.05, **: p<0.01, ***:
768 p<0.001. Detailed statistics are provided in Supplementary Table3.
769
770 **Fig. 4. *Syngap1* expression within cortical excitatory neurons promotes tactile sensitivity and**
771 **perceptual learning. a.** Mouse line probing the impact of *Syngap1*$^{+/-}$ restricted to cortical excitatory
772 neurons (*EMX1-Syngap1-OFF)*; cortical excitatory neuron rescue of *Syngap1*$^{+/-}$ (*EMX1-Syngap1-ON)* - all
773 other cells in brain and body remain heterozygous for this gene. **b-e** Whisker dynamics in free air and
774 during object exploration. Superimposition of 40 frames representing whisking in wt mouse acquired at
775 500Hz illustrating free whisking of a single whisker, scale bar = 5mm **(b)**. Quantification of whisker
776 setpoint **(c)**, amplitude **(d)** and velocity **(e)** during the protraction (prot.) and retraction (ret.) whisking
777 phase during a 30 second recording window for the *EMX1-Syngap1-OFF* mouse line (wt, n=19 and +/fl,
778 n=17) *and EMX1-Syngap1-ON* mouse line (wt, n=19 and +/fl, n=20). **f-j** Active touch dynamics of a single
779 whisker for the first 30 seconds of pole presentation, superimposition of 40 frames representing active
780 touch, scale bar = 5mm **(f)**. Quantification of area under the curve (AUC) for whisker curvature **(g)**,
781 average touch duration **(h)** and the total number of peak protraction detected for each individual touch
782 event **(i)** and their respective animal average **(j)**. Color coding of groups is described in **(a)**. **k-n.**
783 Modulation of *Syngap1* expression in cortical excitatory neuron population in tactile sensitivity assays.
784 Summary schematic of the training phase during passive tactile stimulus (WDIL) performed with a whisker
785 deflection of ~650 º/s corresponding to a medium stimulus intensity and fraction of total trials correct in
786 *EMX1-Syngap1-OFF* **(k)** and *EMX1-Syngap1-ON* **(l)** mouse lines. **m.** Hit rate for *EMX1-Syngap1-ON*
787 animals that reached criteria and underwent the reduced stimulation phase of the WDIL performed with a
788 whisker deflection of ~650 º/s (pull back). **n.** Discrimination index during the testing phase of the NOR-T
789 for objects with 10 groves spacing difference in *EMX1-Syngap1-ON* line. Mice with at least 10 sec of
790 cumulative object exploration in the NOR-T were included in the analysis. Shaded areas and Error bars
791 represent the standard error of the mean (S.E.M.) and number of animals for wild-type (wt: blue, n=17)
792 and *Syngap1*$^{+/-}$ (+/-: red, n=19) is also indicated in white within the bar graph and/or in parentheses. P-
793 value are indicated as n.s.: p>0.05, *: p<0.05, **: p<0.01, ***: p<0.001. Detailed statistics are provided in
794 Supplementary Table4.

795

796 **Fig. 5. Impaired thalamocortical network dynamics during active sensing in *Syngap1*$^{+/-}$ mice**. **a.**
797 Experimental design and timeline during multi-channel silicon probe recordings. 3 probes were used
798 during the recording along with camera and pole presentation while the mouse can move on a treadmill
799 (TM). Different environmental variables were presented (light, sound and a pole that the mouse with a
800 single whisker can interact with). **b.** Schematic of the neural circuitry and probe insertions during the
801 experiment targeting key component of the somatosensory circuit (M1: motor cortex, S1: somatosensory
802 cortex and TH: sensory thalamus). Post hoc analysis of electrode tracts did not have sufficient resolution
803 to separate POM and VPM regions so the TH recordings may reflect units from both areas. **c.**
804 Representative DiI (red) staining of probe implantation in motor cortex (M1), thalamus (TH), and
805 somatosensory cortex (S1, left to right) with reconstructed DiI traces overlayed onto the Allen Brain atlas
806 **d.** Multi probe track reconstruction in Allen Brain atlas for all wt (blue) and *Syngap1+/-* (+/-; red) for all the
807 animals that underwent silicon probe recordings. **e.** Average spike rate (spikes/seconds) for extracted
808 cluster including multiunit activity for both wt and *Syngap1+/-* (+/-) in M1, TH and S1. Small dots represent
809 units, larger dots are animal means and largest dot represents group averages. Half violin plots illustrate
810 the unit distributions. **f.** Raster and PSTH examples of firing for multi-units from M1 (top row), S1 (middle),
811 TH (bottom) in wt and *Syngap1*$^{+/-}$ mice. **g-i.** Subspace analysis of neural communication in Syngap1+/-
812 mice across and within cortical regions. **g**. Schematics of neural subspace dimensionality and predictive
813 performance analysis across neural populations. High-dimensional neural activity in a source population
814 is mapped onto a lower-dimensional subspace that is optimized for predicting the target population
815 activity. **h**. The subspace dimensionality in the source population for predicting neural activity in the target
816 population was determined by selecting the smallest number of dimensions at which the predictive
817 performance, measured by 1-NMSE (Normalized Mean Squared Error), remained within one standard
818 error of the mean (SEM) from the best performance. Bar plots display minimal subspace dimensionality
819 with error bars representing SEM across different randomized choices of the source and target neural
820 populations (see Methods). This analysis was applied across cortical regions, including within and
821 between S1, M1, and TH. To evaluate the significance of differences in subspace dimensionality between
822 genotypes a Monte Carlo permutation test was applied. A consistent trend of increased subspace

823 dimensionality in Syngap1 could be observed, particularly in the connections from TH to S1 and S1 to
824 M1, although these differences do not reach statistical significance. A similar trend was present during
825 touches and inactive whisking epochs **(Supplementary Fig. 6). c.** Predictive performance, measured as
826 1-NMSE (normalized mean squared error), of the target population activity based on the source
827 population activity across the same-region and cross-region pairs.
828
829 **Fig. 6. Impaired nodes of thalamocortical network during active sensing in *Syngap1*$^{+/-}$ mice**.
830 **a-b.** Averaged PSTHs for responsive clusters showing spike rates as z-scores during whisking onset **(a)**
831 and touch **(b)** for M1, S1 and TH. **c.** Characterization of spike rates (as z-scores) from **(b)** based on
832 strength of whisker curvature (t1: 0-25 percentile, t2: 25-50 percentile, t3: 50-75 percentile and t4: 75-100
833 percentile of maximum whisker curvature) for M1, S1 and TH in wt and *Syngap1*$^{+/-}$ mice and the
834 corresponding peak amplitudes of z-score firing rates for each percentile of whisker touch **(d).** Shaded
835 areas and Error bars represent the standard error of the mean (S.E.M.) and number of animals for wild-
836 type (wt: blue, n=17) and *Syngap1*$^{+/-}$ (+/-: red, n=19) is also indicated in white within the bar graph and/or
837 in parentheses. P-value are indicated as n.s.: $p>0.05$, *: $p<0.05$, **: $p<0.01$, ***: $p<0.001$.
838
839 **Fig. 7. Specific components of the touch circuit within the somato-motor cortex are**
840 **hyperconnected in *Syngap1*$^{+/-}$ mice. a.** Model of accelerated maturation of S1L5 neurons based on
841 prior published work[74]. **b.** Breeding strategy to enable S1L5 input mapping in wildtype and *Syngap1*$^{+/-}$. **c.**
842 Consecutive steps for cell type specific tracing: AAV transduction of Cre-dependent helper viruses
843 (PND60, flex-TVA and flex-RG), rabies virus transduction (PND74, EnvA-RV-GFP), and rabies virus
844 spread (PND81). Transduction of the helper virus flex-TVA and rabies virus are visualized respectively
845 with the mCherry and GFP (red and green fluorescent signal) scale bar for brain section fluorescent
846 images is 1mm and 100um for other images. On brain section the anterior-posterior (AP) coordinate
847 relative to bregma in mm is indicated. **d.** Quantification of brain area specific inputs of S1L5 neurons
848 normalized to the starter cell population (SS: somatosensory cortex, AU: auditory cortex, PT: posterior
849 parietal association areas, VI: visual cortex, MO: motor cortex, TH: thalamus, CP: caudoputamen, RS:
850 retrosplenial area, ACA: anterior cingulate area). **e.** Representative images of monosynaptic inputs from

851 the motor cortex (+/+: wt, n=1 – 38 cells, +/-: *Syngap1*$^{+/-}$, n=1 – 59 cells). Dotted line represents the brain
852 outline on the motor cortex for coronal section at Bregma (AP=0mm). Scale bar = 200um. **f.** Flat map of
853 motor cortex connectivity (arbitrary unit, a.u.) in antero-posterior (AP) and media-lateral (ML) averaged
854 across all wt (n=7) and *Syngap1*$^{+/-}$ (+/-, n=7) mice. **g.** Quantification of the distribution of inputs to S1L5
855 normalized to the starter cell population in the antero-posterior axis for inputs from all cortical areas (ctx-
856 >S1L5), all cortical inputs after removing the motor inputs from the quantification (ctx – M -> S1L5), the
857 motor cortex inputs (M1 -> S1L5), the L2/3 motor inputs (M1/L2-3 -> S1L5), L5 motor inputs (M1/L5 ->
858 S1L5; blue: wt, n=7; red: *Syngap1*$^{+/-}$:+/-, n=7; smoothed conditional means). **h.** Cartoon representing
859 recording of LFPs during optogenetic stimulation of M1 an thalamic application of TTX resulting in the
860 quantification of baseline and TTX LFP responses in S1L5. **e.** Field potential traces during baseline and
861 30 min post TTX bath application displaying 2 waveformes (wf1 and wf2). **j.** Quantification of the peak
862 amplitude response during wf1 and wf2. **k-l.** Traces and peak LFP responses in S1L5 after M1L5
863 stimulation at 30 mW/mm2 **(k)** and 60mW/mm2 **(l)** stimulation intensities. **m.** Peak amplitude of LFP
864 responses from different stimulation intensities in wt (n=5) and *Syngap1*$^{+/-}$ mice (n=4). **n.** Recording of
865 LFPs during single whisker deflection. Individual peak LFP responses for each stimulated whisker. Nine
866 whiskers (alpha, beta, A1, B1, B2, C1, C2 D1, gamma) were stimulated consecutively. **o.** LFP amplitude
867 after single whisker deflection in wt (n=8) and *Syngap1*$^{+/-}$ (n=8) across 9 different whiskers. Shaded areas
868 and Error bars represent the standard error of the mean (S.E.M.) and number of animals for wild-type (wt:
869 blue, n=17) and *Syngap1*$^{+/-}$ (+/-: red, n=19) is also indicated in white within the bar graph and/or in
870 parentheses. P-value are indicated as n.s.: p>0.05, *: p<0.05, **: p<0.01, ***: p<0.001. Detailed statistics
871 are provided in Supplementary Table5.
872
873 **Fig. 8. Model for how *Syngap1* expression shapes tactile sensitivity and perceptual behaviors**
874 **through regulation of cortical SMI circuitry. a.** When a *Syngap1+/-* animals explore objects with
875 whiskers, touch information is poorly encoded in cortex, which prevents attentional processes from
876 engaging a state-switch, which leads to reduced exploration times. Reduced exploration time will overtly
877 decrease the opportunity for whiskers to code tactile signals required to compute object features. This
878 impacts the strength of a tactile percept, which will impair perceptual learning and associated adaptive

behaviors. **b.** In these mice, the touch signals that arrive in the cortex during the shortened object exploration are weakly encoded. In L5 somatosensory cortex, these weak touch signals are integrated with overly strong whisker motion (motor) signals, a SNR deficit that will degrade the ability of circuits to compute touch and texture features. Indeed, whisker motion and whisker touch generate two distinct streams of information at the level of the whisker follicle. The motor stream carries real-time whisker location information, while the touch stream contains a code for when touch occurred and how strong it was (through whisker curvature). These streams of information are integrated in barrel cortex L5 neurons, which enables an understanding of where the object rests relative to the head. This model can explain how *Syngap1* mice learn so poorly within the tactile domain. It is important to note that we also demonstrate that perceptual behaviors are disrupted when the task is biased toward whisker touch, but perception is intact for similar tasks when multisensory processes are available to the *Syngap1* animal.

Supplementary Fig. 1. Additional measures during passive tactile stimulus (WDIL) in *Syngap1*$^{+/-}$ mice, related to Fig. 1. Behavioral measures during WDIL training for the low (400 º/s) **(a-e)**, medium (650 º/s) **(f-j)** and high (900 º/s) **(k-o)** whisker stimulation corresponding to Fig.1b. Hit/false alarm (FA) rates and d' scores during task acquisition are indicated for the three intensity levels **(b, e, h)**. d' scores after 20 days of acquisition for the 3 stimulus intensities **(c, f, i)**. **j-n.** Pull back experiments for the WDIL paradigm showing the ratio of mice graduating the task at the different step of training (step2 and step3) **(k)**, the number of sessions **(l)** and the total number of trials **(m)** to graduate step2 and step3 prior to the pull back experiment corresponding to Fig. 1. **n.** Fraction of total trials correct) rate and d' score during decreasing whisker stimulation intensity of the pull back phase of the WDIL. Shaded areas and error bars represent the standard error of the mean (S.E.M.). p-value for main effects and interaction are indicated as n.s.: $p>0.05$, *: $p<0.05$, **: $p<0.01$, ***: $p<0.001$ detailed statistics are provided in Supplementary Table1.

Supplementary Fig. 2 related to Fig. 3. Whisker dynamics and touch detection analysis comparison between WHISK and DLC. **a.** Screen shot of 3 random frames (frame number in white) from highspeed recordings. Raw angle obtained with DLC tracking of the whisker (green) and tracking with the WHISK

software (blue). **b-c.** Output of DLC and WHISK for 4 different measurements (angle, filtered angle, instantaneous amplitude and phase) during a 30 seconds period **(b)** and a snippet of data at the red star for a duration of 1 second **(c)**. **d.** Example and validation of touch detection based on thresholding and DF/F of intensity when the whisker is within the tRaw1 and tRaw2 areas. **e-f.** Comparison of filtered signal with ground truth manually analyzed data **(e)** and their relative accuracy **(f)**. **g.** Example of curvature analysis with DLC fitting a polynomial onto the first 4 proximal whisker labeled points. Green dots are references to the frame equivalent to the curvature displayed in **h**. **h.** Curvature of the whisker over time with red boxes denoting the moment of touch detected as described in **d**.

Supplementary Fig. 3 related to Fig. 3. a. Illustration theoretical and actual data whisker kinematics during whisking and touch against a pole in a head fixed freely whisking behavior. **b.** Illustration of the categorization of different types of touches, from simple to complex with the category 2c being the most complex observed.

Supplementary Fig. 4 related to Fig. 4. a. Immunoblots and quantification of Pan-SynGAP and total protein in the striatum and hippocampus from *EMX1-Syngap1-ON* mouse line. The genotype for the mouse line are reflected as such +/+ Syngap1+/+:Emx1Cre+ and +/ls for Syngap1+/lx-stp:Emx1Cre+ **b.** Rates of recombination in tail and liver tissue from *EMX1-Syngap1-ON* mouse line. The umber of animals for wild-type (wt, n=12) and *EMX1-Syngap1-ON* (+/ls, n=12) is also indicated in white within the bar graph and/or in parentheses Error bars represent the standard error of the mean (S.E.M.). p-value for main effects and interaction are indicated as n.s.: $p>0.05$, *: $p<0.05$, **: $p<0.01$, ***: $p<0.001$. Detailed statistics are provided in Supplementary Table4.

Supplementary Fig. 5. Additional measures for the modulation of *Syngap1* expression within cortical excitatory neurons during tactile sensitivity experiments related to Fig. 4. a. Hit/FA rates and d' during WDIL acquisition for wt and *EMX1-Syngap1-OFF* mouse line (complementary to Fig. 4k). **b.** Hit/FA rates and d' during WDIL acquisition for wt and *EMX1-Syngap1-ON* mouse line (complementary to

935 Fig. 3L). **c-d**. Total fraction trials correct, FA rates and d' in *EMX1-Syngap1-ON* mouse line
936 (complementary to Fig. 3M) **(c)** and their genetic control counterpart which is not expressing Cre **(d)**
937 during decreasing whisker stimulation intensity of the WDIL paradigm. **e.** Ratio of mice graduating the
938 task at the different step of training (step2 and step3) for the genetic control counterpart of the *EMX1-*
939 *Syngap1-ON* which is not expressing Cre. **f.** Exploration times during the testing phase of the NOR-T for
940 objects with 10 groves spacing difference in *EMX1-Syngap1-ON* line (complementary to Fig. 3N). Shaded
941 areas and error bars represent the standard error of the mean (S.E.M.). p-value for main effects and
942 interaction are indicated as n.s.: $p>0.05$, *: $p<0.05$, **: $p<0.01$, ***: $p<0.001$ detailed statistics are provided
943 in Supplementary Table4.
944
945 **Supplementary Fig. 6. Subspace analysis of neural communication in Syngap1+/- mice across and**
946 **within cortical regions during touch and inactive epochs. a.** Subspace dimensionality for predicting
947 neural activity in a target population from a source population, measured during touch epochs. Error bars
948 represent SEM across different randomized choices of the source and target neural populations (see
949 Methods). A significant increase in subspace dimensionality was observed in the TH-to-S1 pair in
950 Syngap1$^{+/-}$ mice compared to wild-type controls ($p < 0.05$). **b.** Predictive performance of target population
951 activity based on source population activity during touch epochs. A significant increase in 1-NMSE was
952 observed in S1-to-M1 interactions in Syngap1$^{+/-}$ mice, suggesting that the neural activity in S1 is more
953 predictive of M1 activity compared to wt. These results suggest altered neural communication dynamics in
954 the S1-to-M1 and TH-to-S1 pathways. **c.** Subspace dimensionality measured during epochs during which
955 no touches or whisks were observed. Similar to the touch epochs, subspace dimensionality was
956 significantly increased in the TH-to-S1 projection in Syngap1$^{+/-}$ mice compared to wild-type controls ($p <$
957 0.05), pointing to a persistent alteration in communication dynamics between these brain regions. **d.**
958 Predictive performance during inactive epochs. A significant increase in predictive performance was
959 observed in the S1-to-M1 projection in Syngap1+/- mice ($p < 0.01$), further supporting the possibility of an
960 altered functional connectivity between these regions in Syngap1 mutants.
961

962 **Supplementary Fig. 7. Multisite silicone probe recordings during behavior related to Fig. 6. a.**
963 Representation of the environmental conditions present during the recordings (dark: black, light: white,
964 pole present: purple, sound present: orange. Motion (blue trace) on the treadmill is displayed along with
965 Drift map and spiking activities across M1, S1 and TH for 2 representative animals (wt and het). **b.**
966 Number of clusters detected during the recording along the three areas per animals. **c.** Raster of the
967 PSTH analysis by depth of the neuronal activity for M1, S1 and TH. Traces for responsive (colored) and
968 non-responsive (grey) MUA clustered by depth are displayed for wt (blue) and het (red). **d.** Quantification
969 of the ratio of responsive clusters and their proportion relative to being responsive only to touch, whisking
970 or both whisking and touch. **e.** PSTH of whisking and touch responses across M1, S1, and TH. **f.** Number
971 of samples represented per animals (circles) and the sum of all the responsive traces (diamond) for wt
972 (blue) and het (red) mice. (wt (blue) and *Syngap1*$^{+/-}$ (het, red); (n.s.: $p>0.05$, *: $p<0.05$, **: $p<0.01$, ***:
973 $p<0.001$).
974
975 **Supplementary Fig. 8 related to Fig. 6. a-d.** Behavioral metric during electrophysiological recordings.
976 Illustration of the Janelia, Low Friction Rodent-Driven Belt Treadmill used during electrophysiology
977 recordings **(a)**. Relative distance moved forward (top) and backward (bottom) during habituation for the
978 first 6 days and recording (last day), the percent of forward movement during each phase of the
979 experiment for wt and het mice **(b).** Cumulative distribution of touches in wt and het mice **(c). d.**
980 Behavioral touch data which have been subdivided into 4 equal bins based on quartile of curvature and
981 the corresponding measures: touch duration, AUC or peak curvature (rows) for each quartile are
982 displayed. **e.** Classification of responsive population for whisking and touch behavior and their spike rates
983 when subdivided by the curvature quartile described in d.
984
985 **Supplementary Fig. 9 related to Fig. 7.** Experimental protocols related to rabies virus tracing and data
986 associated with **Fig. 5**. **a.** Experimental setup and timeline for data acquisition and processing of whole
987 brain tracing data **b.** Cellular segmentation and registration using Wholebrain software for 3
988 representative coronal sections. **c.** Schematic representation of viral transduction. **d.** Example 3D brain of
989 cellular registration from 2D coronal sections. **e.** Mapping of the distribution of the coronal section used

990 for the analysis of all the samples in the antero-posterior stereotactic coordinates. **f.** Total number of
991 sections in which cellular count and brain region registration was performed. **G-h**. Distance between
992 every section sampled in the study **(g)** and their brain coverage **(h)**. **i.** Number of starter cells, cells
993 expressing both GFP and mCherry in subsamples section. **j.** Ratio of the total number of inputs to the
994 number of starter cells counted. Error bars represent the standard error of the mean (S.E.M.). p-value for
995 main effects and interaction are indicated as n.s.: $p>0.05$, *: $p<0.05$, **: $p<0.01$, ***: $p<0.001$ detailed
996 statistics are provided in Supplementary Table5.
997
998

999 **METHODS**

1000

1001 **Mice**

1002 All mouse procedures were conducted in accordance with the NIH Guide for the Care and Use of
1003 Laboratory Animals, and all methods were authorized by the Scripps/UF Scripps Biomedical Research
1004 Institutional Animal Care and Use Committee. Both males and females (M/F) were used in all
1005 experiments except when explicitly noted. The design and maintenance of constitutive and conditional
1006 *Syngap1* lines have been described previously [66,90]. Briefly, we used inbred constitutive heterozygous
1007 *Syngap1* knock-out mice (*Syngap1*$^{+/-}$), conditional knock-out (*Syngap1*$^{+/fl}$ JAX: #029303) and conditional
1008 rescue (*Syngap1*$^{lx\text{-}st}$ JAX: #029304) mouse lines. Emx1-Cre (JAX: #005628) mice were purchased form
1009 Jackson and crossed with *Syngap1*$^{+/fl}$ for conditional knock-out or *Syngap1*$^{lx\text{-}st}$ for conditional rescue
1010 experiments. Rbp4Cre mouse line (MMRRC_031125-UCD) was obtained from MMRC and was crossed
1011 to *Syngap1*$^{+/-}$ to study structural connectivity (monosynaptic tracing). Thy1-ChR2-YFP mouse line (JAX:
1012 #007612) was crossed to *Syngap1*$^{+/-}$ for functional validation and electrophysiological recordings. Cohort
1013 construction was designed to generate comparable sample sizes between genotypes and sexes, by
1014 allocating equal (if feasible) number of age-matched littermates from separate litters, usually more than
1015 two. Then, animals were assigned a number to hide the identity of genotype and/or group assignment.
1016 Experimentalists were blind to genotype at the time of data acquisition and analysis. Data collection
1017 occurred from mice >8 weeks of age. Mice were housed 4-5 per cage on a 12-hour normal light-dark
1018 cycle. In experiments requiring head-fixation, mice were transferred to a reverse light-dark cycle 2-3
1019 weeks prior to headpost surgeries. Following headpost surgeries, animals were singly housed, with the
1020 addition of environmental enrichment in the form of a plastic running wheel (Bio-Serv) or a cardboard hut.
1021 Only animals that died, became non-responsive or did not participate in behavioral tasks during the study
1022 or data collection procedures were excluded from analysis.

1023

1024 **Headpost surgery**

1025 Headpost surgeries were completed according to established procedures with minor modifications [23]. A
1026 custom titanium headpost was implanted onto the skull of 8-10 week old mice. Animals were anesthetized
1027 with isoflurane (5% induction, 1.5-2% maintenance) via a low-flow vaporizer (Somno Low-Flow Vaporizor,

1028 Kent Scientific) and placed into a stereotaxic frame (David Kopf Instruments). Body temperature was
1029 maintained at 37°C by a regulated pad with temperature feedback under the animal and ophthalmic
1030 ointment (Artificial Tears, Akorn) was placed onto the eyes for lubrication. The scalp was sterilized with
1031 alternating swabs of Betadine and 70 % ethanol. A small flap of skin was removed over the midline
1032 exposing both Lamda and Bregma, and the periosteum was gently cleared with a cotton swab. The skull
1033 was scraped with a scalpel and a thin layer of glue (Vetbond, 3M) was applied to the surface, reaching
1034 the wound margins. The headpost was lowered and affixed onto the skull via dental cement (Metabond,
1035 Parkell). Animals were injected (SubQ) with a cocktail of carprofen (10 mg/kg, Zoetis) and enrofloxacin (5
1036 mg/kg, Norbrook), made in sterile saline (0.9 % NaCl, Vetivex). Animals recovered on a heating pad
1037 before being placed into their home cage. The same drug cocktail was injected once daily for the
1038 following two days for pain management and were routinely monitored for distress.
1039
1040 **WDIL paradigm**
1041 Apparatus: The whisker dependent-instrumental learning (WDIL) paradigm was performed as previously
1042 described with minor modifications [23]. Briefly, mice were singly housed in a reverse light-dark room
1043 following headpost surgery and placed on water restriction (1 mL/d; food ad libitum), 3-7 days following
1044 recovery from headpost surgery. Animals were trained one session/day (~5d/week), all during the dark
1045 phase of the light cycle. The behavioral rig was controlled by BControl software (C. Brody, Princeton
1046 University) running in Matlab (2013B, Mathworks) on a master PC (Dell) and a Real-Time Linux State
1047 Machine (RTLSM). The behavioral rig consisted of a light and sound proofed box constructed from
1048 aluminum rails for the frame and black hardboard (Thorlabs) with sound attenuating foam. Head-fixation
1049 parts were custom built (Max Planck machine shop) and purchased from Thorlabs.
1050 Habituation: Habituation to head-fixation commenced with handling of mice for 1 d, then presentation of a
1051 custom-built stainless steel body tube for 1 d. Mice were then exposed to head-fixation for 3 consecutive
1052 days with increasing time spent under head-fixation (10, 30 and 45 mins). Mice were continuously
1053 monitored via IR light and videography (Raspberry Pi HQ; Model 3B). White noise (70 dB) was
1054 continuously played within the apparatus and all subsequent sessions to attenuate room noise. Following
1055 habituation to head-fixation, all but one whisker on each side, C2, were trimmed under light (2%,

1056 isoflurane) anesthesia and kept trimmed throughout the experiment. The following day, mice learned to
1057 associate water availability by licking water from a lickport. Detection of licks was performed
1058 electronically[91] and precise water delivery (8 μL/ reward) was controlled with a solenoid valve and
1059 controller (INKA2424212H VHS-24V and IECX0501350A, The Lee Company). Lickport training lasted for
1060 a maximum of 10 mins/session or the total consumption of 1 mL of water per session (whichever came
1061 first), for two sessions. A lick would induce water delivery which could be consumed, however another lick
1062 would not deliver more water until a 1.5 s epoch passed. During lickport training, the C2 whisker was
1063 inserted into a plastic tube attached to a piezo to habituate the animals for training.
1064 Training: Mice proceeded to WDIL training which was designed as a "detection" task, whereby the C2
1065 whisker on the right side was plugged into the piezo actuator, acting as the Go signal and a "dummy"
1066 piezo was placed beside the whisker deflecting piezo but was not attached to a whisker, acting as the
1067 NoGo signal. Trials consisted of 50% "Go" and 50% catch (NoGo) trials in a random fashion, with the
1068 exception of no more than three consecutive trials could be of the same type. For Go trials, the whisker
1069 was deflected by the piezo actuator controlled by a linear voltage amplifier (E-650.00 and PL140.11,
1070 Physik Instrumente or EPA-008-1 – 1 and Q220-A4-203YB - 5+, Piezo.com) and a waveform generator
1071 (4054B, BK Precision), for 0.5 or 1.5 s (depending on the stimulus intensity) with a 40 Hz sinusoidal wave
1072 (rostral to caudal, 2-6 ° depending on the stimulus intensity). Bending of the piezo was calibrated using a
1073 laser-based displacement device (LD1610-0.5, Micro-Epsilon). For NoGo trials, the dummy piezo was
1074 stimulated in the same fashion as the whisker deflecting piezo, however no whisker stimulation was
1075 provided. The response window opened 0.1 s following stimulus onset and lasted for 2 s. During the
1076 response a window, a lick on the lickport resulted in a "hit" on Go trials and triggered an 8 μL water
1077 reward, and a "FA" on NoGo trials. Withholding a lick on Go trial resulted in a "Miss", while no licking on
1078 NoGo trials resulted in a "correct rejection". No water reward was provided on correct rejection trials and
1079 no punishments were given on Miss or FA trials. The intertrial interval remained constant at 4 s, but mice
1080 were required to withhold licking for 1.5 s before the piezo was stimulated for trials to proceed and
1081 therefore, provided some level of randomness of trial timing. Mice performed the task until satiated.
1082 Animals were trained for 20 consecutive sessions. Performance was based on a number of factors
1083 including total trials correct, discrimination index (d'; calculated as $d' = z(hit) - z(FA)$, with z scores

1084 computed using the function NORMSINV in excel) and Hit and FA rates. Mice were scored to be expert
1085 learners (ie. reached learning criteria) when the following metrics were achieved for two consecutive
1086 days: d' ≥ 1.1, total trials correct ≥ 70%, Hit rate ≥ 70% and FA rate ≤ 30%. Mice that reached criteria
1087 were graduated to a reduced stimulation protocol after 20 sessions that consisted of a similar task
1088 structure however, the stimulus intensity was reduced on consecutive days (6 °, 4.5 °, 3°, 1.5°, 0.5° for
1089 angular deflection).
1090
1091 **NOR-T**
1092 Novel object recognition (NOR) and novel object texture discrimination (NOR-T) paradigms were
1093 developed for use with high-speed videography and conducted with *Syngap1*$^{lx\text{-}st}$ (heterozygous KO) and
1094 *Syngap1*$^{lx\text{-}st}$ x Emx1-Cre (conditional rescue) mouse lines to assess recognition memory and whisker-
1095 dependent texture discrimination in a freely moving/non-head fixed behavioral setting as a proxy to
1096 assess somatosensory cortical function in these mice.
1097 Apparatus: The apparatus was assembled using infrared-transmissible plexiglass sheets (Part #
1098 ACRY31430, ePlastics) to fashion an open-top box (44(L) x 44(W) x12(H) cm). Four infrared lamps were
1099 attached at each corner, a monochrome camera (A1300, Basler) with a 25mm lens positioned 56 cm over
1100 the center floor of the box and two high-speed cameras (Spark SP-5000M-CXP2, JAI) suspended 22 cm
1101 over each of the two objects were used for video recording. The apparatus was illuminated with diffuse
1102 LED lights from above at ~ 85 Lux to promote exploration. The Basler camera was set to record at 30 fps
1103 to assess full arena activity. The two high speed cameras were set to record at 160 fps to determine
1104 when and how long the mouse explored either object with its whiskers. The Basler camera video data
1105 was fed into Bonsai (https://bonsai-rx.org/) to track animals in real time and produce triggers in response
1106 to animals entering ROIs surrounding the objects. These triggers were fed, via an Arduino (Uno R3,
1107 Arduino), into the high-speed camera trigger to acquire frame captures. Video recordings from the high-
1108 speed cameras were recorded to a DVR system (DVR Express Core 2, IO Industries) using Coreview
1109 software for offline analysis.
1110 NOR-T: 3D-printed white "cog-wheel" columns (7.4 (H) x 3 (D) cm) with different numbers of teeth (50, 75
1111 or 85 per objects corresponding respectively to 5, 8 and 9 ribs/cm) with smoothed cone tops and a

separate smooth-surfaced circular base (1.8 (H) x 3 (D) cm) into which the poles screwed served as objects for texture discrimination. Bases (equidistant from the corners and 9cm from each side of the arena) were fixed throughout the task while familiar (8 ribs/cm) and novel (5 or 9 ribs/cm) poles could be interchanged throughout the task for an entire cohort. Mice were run initially in two 10 min habituation sessions with no objects in the arena. The first session conducted with only the Basler camera suspended above the arena, and the second session conducted with all three cameras positioned as in the training and testing phases. On the following days, each mouse was run in a training session with two identical familiar poles and a testing session (15 mins each) with one of the familiar poles and a novel pole separated by a 5 min intertrial interval in the home cage. Poles were cleaned with 70% EtOH, dried, and stored in clean bedding between sessions while affixed bases were wiped cleaned and dried during ITIs with urine and fecal boli removed from the arena without additional cleaning. Arenas and poles were cleaned between animals. Positions of the novel pole were counterbalanced throughout the cohort. Overall activity was assessed during habituation phases. Time spent with familiar and novel poles were compiled using session videos analyzed manually with BORIS software (https://www.boris.unito.it/) by scoring the time when animal whiskers were in contact with the objects. Comparisons between training and testing phases were performed using two way ANOVA analyses, and % novel exploration ((novel time/(novel and familiar times) x 100) and discrimination index values ((novel-familiar times/(novel+familiar times) were calculated from the pole duration data for each mouse with genotype differences assessed with unpaired t-tests. Mice with at least 10 sec of cumulative pole exploration were included in statistical analyses. For the NOR-T experiment with 8 and 9 ribs/cm object with whisker and no whisker in wt mice. For wildtype mice without whiskers 10 mice were included in the analysis and meeting the criteria out of 11 mice. For wildtype mice with whiskers 10 mice were included in the analysis and meeting the criteria out of 10 mice. For the NOR-T experiment with 8 and 9 ribs/cm object Syngap1+/-. For wildtype mice 8 were included in the analysis and meeting the criteria out of 10 mice. For Syngap1+/- mice 6 were included in the analysis and meeting the criteria out of 12 mice. For the NOR-T experiment with 5 and 8 ribs/cm object Syngap1+/-. For wildtype and Syngap1+/- mice 10 were included in the analysis and meeting the criteria out of 10 mice, respectively.

1139 NOR: Novel object recognition sessions commenced once all mice of a particular cohort finished NOR-T
1140 sessions and were conducted in the same manner as the NOR-T sessions with no initial habituation
1141 sessions. Two different types of objects (two identical master locks for the familiar objects and a mini
1142 stapler for the novel object) were used in this paradigm. These objects have been verified extensively as
1143 approachable with no significant biases for exploration time in the Frick lab [92] and in unpublished data
1144 from the lab. The objects were temporarily fixed to the floor of the arena with heavy duty double-sided
1145 tape not accessible to the mouse. Objects and arena were managed within and between training and
1146 testing phases as in the NOR-T paradigm including counterbalancing of the novel object position. Data
1147 were subjected to the same analyses as in the NOR-T paradigm. Mice with at least 30 sec of cumulative
1148 object exploration in the NOR were included in statistical analyses. For the NOR experiment 12 wildtype
1149 mice were run in the study and 7 out of 12 met the exploration criteria, 13 *Syngap1*$^{+/-}$ mice were run in
1150 the study and 10 out of 13 met the exploration criteria.
1151
1152 **Free-whisking and active touch paradigms**
1153 Following headpost surgery, habituation to head-fixation and whisker trimming (described above), whisker
1154 movements (C2 whisker on the left side) were recorded during "free-air" trials (no presented) in a dark,
1155 sound-isolated chamber while head-fixed. Videos (50 s in duration) were recorded at 500 Hz from above
1156 at 640 x 480 pixels resolution with a high-speed camera (DR1-D1312-200-G2, Photon Focus) coupled
1157 with a 0.243X bi-telecentric lens (MVTC23024, Thorlabs) and Streampix software (Version 8, Norpix). The
1158 field of view was illuminated from below with an array of infrared light-emitting diodes (B001BC52W2,
1159 Amazon) with a diffusion sheet (3026, Rosco) placed above the array.
1160 For active touch experiments, a vertical metal pole (2 mm in diameter), was moved into the whisking
1161 range of the C2 whisker (left side) via a set of feedback controlled linear actuators (L16-P 50mm,
1162 Actuonix), controlled via an Arduino (Uno R3, Arduino) and a motor control board (Part # 1438, Adafruit).
1163 Placement of the pole was adjusted manually for each animal such that the pole resided in line with the
1164 snout (rostrally) and 5-8 mm lateral of the whisker pad. The pole was presented to the animals for a total
1165 of 5 mins each, however only the first 30 s following the first touch was used for further analysis.

1166 Analysis of videos comprised of tracking whiskers offline using the Janelia Whisker Tracker [93], which
1167 supplied whisker traces in 2-dimensional space, followed by manual curation. Processing of this data was
1168 completed in MATLAB (2018b, Mathworks) using established protocols [94,95]. Briefly, instantaneous phase,
1169 amplitude and setpoint were acquired by using the Hilbert transformation of the band-pass (4-30 Hz,
1170 Butterworth) filtered angle. Instantaneous frequency was obtained from the derivative of the
1171 instantaneous phase following unwrapping and conversion to whisk cycle. Angular velocity and
1172 acceleration were quantified by taking the first and second derivatives of the smoothed (Savitzky-Golay
1173 filter; 3rd order, 9 frames) angle. Protraction and retraction values were resolved by obtaining positive and
1174 negative peaks of the resulting traces in question. The moment and duration of touch was determined
1175 manually via BORIS software by experimenters blinded to genotype.
1176
1177 **Pole localization task**
1178 Mice were trained in a pole localization task (Go/NoGo), based on previous studies (O'Connor et al.,
1179 2010), in the same apparatus and with similar pre-training methods (surgery, water restriction,
1180 habituation, lickport training) described above for the WDIL paradigm with minor modifications. This task
1181 was designed as a "discrimination" task. Briefly, mice used the C2 whisker to discriminate between two
1182 pole locations. A smooth pole (1.6 mm in diameter) was positioned (8-12 mm lateral from midline) in a
1183 home position via a high resolution and repeatable stepper linear actuator (NA11B30-T4, Zaber) coupled
1184 to a low friction linear slide (6203K317, McMaster-Carr) prior to trial initiation. Mice were required to
1185 withhold any licking for 1.5 s prior to trial initiation for the trial to proceed. On Go trials, the pole was
1186 positioned in a posterior position (3 mm from home) and lifted into the whisker range by a pneumatic
1187 linear slide (SLS-10-15-P-A, Festo) attached to the linear actuator. On NoGo trials, the pole was moved
1188 to an anterior position (3 mm from home) and lifted. An auditory tone to cue trial initiation was not used,
1189 however, the pneumatic lift generates a sound that is not covered by the white noise. Therefore, the offset
1190 of the Go and NoGo was 6 mm, but adjusted for each animal so the home position was in line with the
1191 snout. It took ~500 ms for the pole to move into position and ~200 ms for the pole to move upward into
1192 whisker range. During this time, mice could lick the lickport without any effect on trial outcome. The
1193 response window started ~1 s after the start of the upward pole movement and was open for 2 s. Mice

made their decision during this time by licking an electronic lickport. On Go trials, if the animal licked, they received an 8 μL water reward and was considered a hit. If they withheld their lick, it was considered a miss. On NoGo trials if the animal licked, it was considered a FA and the animal received a 15 s timeout with the pole remaining in the upward position. If they withheld their lick, it was considered a correct rejection, however no reward was provided. Following the end of the response window (and punishment time), the pole dropped and was moved back to the home position and a 4-6 s intertrial interval began. Animals performed 200-300 trials per session, 1 session/day, ~5 session/week for 29 sessions. Trial types (Go/NoGo) were presented randomly with the only limitation of no more than three of the same trial types could be presented in a row. Animal performance was quantified in a similar fashion to the WDIL paradigm described above.

High speed videography of mouse whiskers was performed on five sessions throughout the training, including Session 1, 17 and 25. These were picked to include whisking behavior when the animals were completely naïve to the task (HS1, session1), when the animals (at a population level) were well into the learning phase (HS3, session17), and at the end of training (HS5, session 25). An addition 2 sessions were recorded based upon individual learning curves. HS2 was performed for each animal when their learning curve showed a steep acceleration (session 10-15) indicating learning. HS4 was conducted after the animal had reached criterion for expert level (as described in the WDIL paradigm) for two consecutive days.

Acquisition of whisking behavior and pole touches during the task was performed using a high-speed camera (Spark SP-5000M-CXP2, JAI; ~500 Hz frame rate, 640 x 480 pixel resolution) under infrared illumination and recorded to a DVR system (DVR Express Core 2, IO Industries) using Coreview software. Each trial triggered a new recording that extended 3 s prior and 3.1 s after upward pole movement (using a pre-trigger buffer). This provided whisker activity prior to pole movement, sampling the pole and during decision making.

1221 Whisker tracking and processing was performed using the Janelia Whisker Tracker and custom Matlab
1222 scripts, as described above, on a trial-by-trial basis. For whisking analysis during electrophysiological
1223 recordings whisker tracking was performed with DeepLabCut where 5 points along the single whisker
1224 track the whisker location. Whisker angle was calculated from the base of the whisker and the whisker
1225 pad to the next marker on the whisker. The moment of touch was quantified using a threshold-based
1226 method assessing the DF/F of pixel intensity within three 12x2 pixel areas 1 pixel away and tangential to
1227 the pole.
1228

1229 **Monosynaptic tracing**

1230 Viral preparation and monosynaptic tracing were performed as previously described [74,76]. Monosynaptic
1231 inputs onto a genetically define cell population of Layer 5 neurons in S1 were targeted with helper virus
1232 AAV9-CAG-Flex-RG (Addgene 48333) and AAV9-CAG-Flex-TCB (Addgene 48332,[75]) in conjunction with
1233 pseudotyped rabies virus EnvA-RV-GFP in Rbp4Cre mouse line crossed with *Syngap1*$^{+/-}$. AAV9-CAG-
1234 Flex-RG (titer: 1.10^12 IU/ml) and AAV9-CAG-Flex-TCB (titer: 1.10^12 IU/ml) were mixed as a 1:1 ratio
1235 and 400 nl were unilaterally injected in S1BF (AP: -1.3 mm, ML:+3.0 mm and DV:-0.45 mm from
1236 Bregrma) at a rate of 200 nl/min. Two weeks after the first injection 400 nl of EnvA-RV-GFP (titer: 1.10^8
1237 IU/ml) was injected in the same location at a rate of 200 nl/min. 7 days after injection of EnvA-RV-GFP
1238 the animals were deeply anesthetized and intracardially perfused with 0.1 M PBS followed by 4%
1239 paraformaldehyde.

1240 **Histology and image acquisition**

1241 After perfusion the brains were post fixed in 4% PFA overnight, placed in 30% sucrose for 3 days prior to
1242 being snap frozen in 2-methylbutane and stored at -80 °C. On the day of slicing the dorsal part of the
1243 brain was placed on a grid, aligned and subsequently embedded in OCT against a frozen razor blade at
1244 the posterior end of the brain, creating a plane perpendicular to the dorsal part of the brain and parallel to
1245 the microtome blade. This ensures the proper alignment of the brain in the medio/lateral and
1246 dorso/ventral axes which facilitates registration to the mouse reference atlas. The whole brain was sliced
1247 on a microtome at 50 um intervals, with every other slice mounted with DAPI (P36931, Invitrogen) onto a
1248 microscope slide. The brain was subsequently imaged on an INCell Analyzer 6000 (GE) for rapid

1249 acquisition with a Nikon 4X/0.20, Plan Apo, CFI/60 at 1.625 um pixel size. Acquired images were
1250 obtained using FITC (excitation: 488nm, emission: 525nm).
1251 Quantification of monosynaptic tracing.
1252 Retrograde labeled cell bodies were segmented and registered onto the mouse reference atlas using
1253 WholeBrain software [76]. To quantify the starter cell populations, sections with red signal from the
1254 transduction of AAV9-CAG-Flex-TCB were pre-identified and re-acquired on the InCell 6000 with a Nikon
1255 10X/0.45, Plan Apo, CFI/60 at a resolution of 0.65 um pixel size for both FITC (excitation: 488nm,
1256 emission: 525nm) and dsRed (excitation: 561nm, emission: 605). The overlapping population of green
1257 and red cell bodies were manually quantified with ImageJ and defined as the starter cell population. All of
1258 the identified inputs for any given brain regions were normalized to the total number of starter cells
1259 identified per mouse brain.
1260 Quantification of electrode tracks.
1261 Sections were imaged on an IN Cell Analyzer 6000 (GE) with a Nikon 4X/0.20, Plan Apo, CFI/60 at 1.625
1262 um pixel size with dsRed (excitation: 561nm, emission: 605) corresponding to the signal emitted by DiI to
1263 identify the electrode and FITC (excitation: 488nm, emission: 525nm) to capture the outline of the brain
1264 with autofluorescence of the tissue. The acquired images were stitched with channels merged prior to
1265 atlas registration and electrode track visualization, which was performed with SHARP-TRACK[96].
1266 **Electrophysiological Recordings**
1267 Mice went through a protocol to allow acquisition of electrophysiological recordings in multiple brain sites
1268 in an awake, head-fixed setting. Details of this protocol are detailed below.
1269 Day1 - Surgery.
1270 The mouse underwent headpost surgery, see prior Methods, with the following addition for
1271 electrophysiological recordings. The entire scalp was removed and the periosteum was gently cleared
1272 with a cotton swab. The skull was then leveled in the antero-posterior axis by having Bregma and
1273 Lambda in the same plane, while the medio-lateral axis was leveled by adjusting the lateral point in the
1274 same plane 2 mm from the midline on each side. Enough bone was shaved from the skull with a 0.6 mm
1275 drill bit to create four reference points. This procedure did not result in exposing the brain. The reference
1276 points were located above the future electrode point of entry to reach the motor cortex (M1; AP:1.0, ML:-

1277 1), the thalamus (TH, AP:-1.5, ML:-1) and the somatosensory cortex (S1, AP: -2, ML: -3.5), along with the
1278 front left corner where the headpost would be located (AP: -5.5, ML: 1.5). A silver wire pre-soldered to a
1279 female gold pin was in contact with the brain above the cerebellum (AP:-5.5, ML:0). Dental cement
1280 (Metabond, Parkell) was applied to secure the 3D printed plastic well, headpost and ground wire. At the
1281 end of the procedure Kwik-Cast (World Precision Instruments) was applied within the well to protect the
1282 skull surface for downstream procedures.
1283 Day4 - IOS imaging.
1284 Three days after recovery of the headpost surgery, Intrinsic Optical Imaging (IOS) was performed to
1285 measure the hemodynamic response of the somatosensory cortex to define the cortical area
1286 corresponding to brain activity responses after single whisker stimulation (C2). The mouse was
1287 anesthetized as described in the headpost surgery protocol. All the whiskers were fully trimmed to the
1288 base of the whisker pad except for the whisker C2 contralateral to the cortical area of interest (trimmed to
1289 a ~5 mm length). The skull was drilled in concentric circles over S1 (AP: -2, ML: -3.5) through the spongy
1290 bone. Debris were removed with compressed air and Ringers solution was applied to cool the bone and
1291 remove the debris. When cerebral blood vessels became visible a scalpel blade (#501251, World
1292 Precision Instruments) was used to shave the bone further until blood vessels were clearly visible. The
1293 mouse was moved from the stereotaxic instrument to the IOS imaging rig and the anesthesia was
1294 reduced to 0.7% in conjunction with the injection of a sedative (chlorprothixene; 1 mg/kg, intramuscular).
1295 Kwik-Cast was removed from the well and ophthalmic ointment (Artificial Tears, Akorn) was applied on
1296 the edge of the well filled with saline and sealed with a glass coverslip. IOS imaging was subsequently
1297 performed as previously described[23]. Briefly, imaging was performed under a 4x objective on an upright
1298 microscope (BW51X, Olympus) and the skull was illuminated with a 630 nm LED light ring mounted to the
1299 objective. Images were acquired with a Zeiss Axiocam camera (Carl Zeiss) controlled my μManager
1300 software (Open Imaging, Inc.). The C2 whisker was deflected for each IOS trial (50-70 trials total) and
1301 resulting images were processed using the IO and VSD Signal Processor plugin in ImageJ [97].
1302 Day5-11 - Habituation. The day after IOS imaging, the mouse was habituated to head-fixation on a
1303 treadmill (https://www.janelia.org/open-science/low-friction-rodent-driven-belt-treadmill). The mouse was
1304 handled for 5 min in the morning. In the afternoon it was handled for 5 min prior to being introduced to the

1305 treadmill and allowed to explore the treadmill for 5 min. Day 6 was the first day of gradual head fixation
1306 with the animals being head-fixed for 15 min, 30 min on day 7, 1hr on day 8 and day 9, and finally 2hr on
1307 day 10 and 11.

1308 Day12 – Surgery.

1309 The mouse was placed in the stereotaxic apparatus (KOPF) to perform 3 craniotomies for future electrode
1310 insertion. The C2 whiskers was trimmed to a length of 5 mm. The skull was properly positioned
1311 (correction for antero/posterior and medio/lateral tilt). Circular craniotomies of a 1.5mm diameter were
1312 drilled automatically with the Neurostar surgery robot with a 0.2 mm drill bit (Harvey tool) above the area
1313 marked during the headpost surgery and identified with IOS for the S1 craniotomy. Once the drilling was
1314 performed, the inner part of the bone was removed. Gelfoam and Ringers solution were applied to
1315 minimize potential bleeding. Kwikcast was applied to protect the brain after the craniotomy and the mouse
1316 was placed on a heating pad for recovery before returning to its home cage for 3 to 4 hrs.

1317 Day12 – Apparatus.

1318 The apparatus was a 30 inx30 inx50 in custom made noise-attenuated chamber mounted on a
1319 breadboard (MB30, Thorlabs). The recording consisted of a 20 min period in the dark followed by 40 min
1320 in the light and 20 min in the dark. In the middle of this sequence white noise that was playing (70 dB)
1321 was turned off. In addition, 2 pole presentation epochs of 10 min occurred 5 min prior to the light
1322 transition. Light, white noise, and actuators (L16-P 50mm, Actuonix) for the pole presentation were
1323 controlled via Matlab through a NI DAQ (USB-6363)**.**The signals for the NI DAQ converged to the eCuber
1324 Server (White Matter) for synchronization. The mouse was video monitored with e3Vision Cameras
1325 (White Matter). Mouse whisking and touch behaviors were acquired at 500 Hz with a high-speed video
1326 camera (DR1-D1312-200-G2, Photon Focus) and a variable zoom lens (Computar) with StreamPix 6.0
1327 software for the entire duration of the recording. The high speed captured video was downsampled with
1328 ffmpeg software (Version 4.0.2) before data analysis. IR light illuminated the mouse and a custom IR
1329 backlight was located underneath the mouse during video recording. Three 3-axis micromanipulators
1330 (New Scale Technologies) were mounted on an inverted 360 MPM-1 platform (New Scale Technologies)
1331 to enable probe insertion at 3 different locations. H2 probes for TH, H2 or H3 probes for S1 and H3
1332 probes for M1(Cambridge Neurotech) were connected via Molex, Omnetix connector adaptor to the HS64

head stages (White Matter), which were connected to the e3 Server (White Matter). The fully retracted probes were positioned in the insertion probe axes above predetermined stereotaxic coordinates of the area of interest. Prior to placement on the manipulators the probes were coated with DiI (Life Technologies, #V22885).

Day12 – Data acquisition.

The mouse was placed on the treadmill and moved to the rig for probe insertion and recording. The reference and the grounds of the probes were grounded to a common ground shared with the ground of the animals. After the mouse was placed in the recording apparatus all the probes were manually lowered to a few millimeters above the skull surface. The position of the probes was monitored with a digital microscope (Dino-Lite, Premier) and the S1 probe was refined based on the blood vessel map corresponding to the responsive area of whisker stimulation determined by IOS imaging. The probes were then lowed at coarse intervals with the manipulator to break the dura. When all the probes were implanted, the probes were further inserted automatically at a rate of 200 um/min until the pre-determined target depth was reached. The probes settled for 30 min prior to recording. Electrophysiological data were acquired at 25 kHz using the Open Ephys GUI with the e3 custom module. Binaries were acquired along with digital and analog data streams from the NI DAQ box through the E3 servers. Whisking and touch behavior were acquired at 500 Hz. At the end of the recording the probes were removed and cleaned and immersed in 1 % Tergazyme overnight.

Data Analysis – Electrophysiology.

Raw binaries were processed in Matlab (2018). Median noise filtering was applied and channels were sorted according to the channel map, followed by common average referencing. From the binaries, action potentials (APs) and local field potentials (LFPs) were extracted using a Butterworth low pass filter between 0.5 and 100 Hz for the LFPs and a high pass filter between 300 Hz and 6kHz for the APs. The filtered APs were run through spike sorting software (Kilosort 2.0). Clusters of spikes were identified as “good” isolated units and “multi-unit activity”. Spike times for these categories were assigned to a specific depth in order to obtain a measure of overall spiking at a given location. Whisking onset was defined when the whisking amplitude increased by 2° within a 250 ms period [69]. The epochs during which the pole was present were excluded from the whisking analysis. Spike rate was aligned to the whishing onset to

1361 obtain peri-stimulus time histograms (PSTH) based on depth of the probes. The PSTH for whisking were
1362 performed with analysis window from -0.25 to 0.5 s and a baseline from -0.25 to 0 s with bins of 10 ms.
1363 The touch onset was identified with a threshold-based method registering whisker and pole interaction.
1364 Manual validation of the method was performed on a subset of the data. The pole was position was
1365 maintained between both pole presentations and kept relatively standard between animals via following
1366 the position of a guided template overlay on the live camera view. The whisker resting state was posterior
1367 to the pole and any touch occurring when the whisker was anterior to the pole was removed from the
1368 analysis. PSTH analysis for touch was performed similarly to the whisker's PSTH with 1 ms bins, an
1369 analysis widow from -0.025 to 0.05 s and a baseline from -0.025 to 0 s. The z-scored PSTH for whisking
1370 and touch were smoothed with a Gaussian kernel using the smooth function. Artifacts at the end and
1371 beginning of the traces were removed from the analysis. Responsive clusters by depth were defined as z-
1372 score firing rate above 1.5 in the post baseline window. The Findpeak function was used to identify the
1373 peak value of the trace crossing this threshold and onset of the response was defined as the first
1374 inflection point of the trace from the identified peak to the beginning of the trace.
1375
1376 **In vivo single electrode field recordings**
1377 LFP recordings were made on a custom in vivo system as described previously[23]. Briefly, mice were
1378 anesthetized with 1.8 g/kg urethane (Sigma-Aldrich), followed by implantation of a custom headplate, and
1379 a 1 mm craniotomy was made over S1. The pipette was lowered 500 µm from the brain surface in S1
1380 (AP: 3.5, ML: 2). Recordings were performed in current-clamp mode with the following internal solution in
1381 the electrode (mM): 130 potassium gluconate, 5 KCl, 10 HEPES, 10 sodium phosphocreatine, 0.4 EGTA,
1382 1 Na-GTP and 4 Mg-ATP (pH 7.3, 285-290 mOsm). Electrophysiological signals were amplified with
1383 Multiclamp 700B (Molecular Devices), filtered at 2 KHz, digitized (10 KHz) with an NI USB-6363 DAQ
1384 (National Instruments) and recorded using the NI acquisition system in Matlab. Optogenetic stimulation
1385 was controlled via the NI acquisition system in Matlab and relayed through the NI DAQ, a LED controller
1386 (LEDD1B, Thorlabs), fiber optic LED 470nm (M470F3, Thorlabs) and a fiber optic cannula (CFML12L02,
1387 Thorlabs) inserted in M1 (AP:1.0, ML:-1, DV:-0.5). Before each experiment the power of the laser was
1388 calibrated to obtain the following powers 1, 5, 10, 15, 20, 25,30, 35 and 40 mW/mm2 at the end of the

1389 fiber optic. Piezo stimulations were performed on a single whisker with a deflection of 200 μm at 2 mm
1390 away from the whisker pad (6° or 1200 °/s). To obtain LFPs, 30 trials were averaged.
1391
1392 **Neural communication subspaces**
1393
1394 To analyze neural communication subspaces in neural populations for wild-type and *Syngap1*$^{+/-}$ mice we
1395 applied the regularized regression technique described in the noted reference[71]. We analyzed neural data
1396 collected from three types of behavioral epochs: whisks, touches, and inactive periods. For each whisking
1397 or touch event, a symmetric time window was centered on the event time. For whisking, the window
1398 spanned 500 ms before and after the event, while for touch, the window extended 50 ms before and after.
1399 The inactive epochs were established by finding intervals without whisking or touch events. Intervals of at
1400 least 1 second between events were considered as potential windows of inactivity. Each window was
1401 defined to begin at least 1 second after one event and end at least 1 second before the next, ensuring
1402 that the neural activity within the window was not contaminated by any whisks or touches.
1403
1404 *Data preprocessing*
1405
1406 Spike trains collected from WT and HET mice were transformed into spike rate arrays for the different
1407 brain regions (M1, S1, and TH). To do so, we convolved spike trains with a moving window (20 ms wide),
1408 allowing for the smoothing of the spike rates over time. The smoothed data were then downsampled to
1409 reduce the time resolution, which allowed for more efficient analysis of the neural dynamics. The
1410 downsampling process was implemented with a stride of 5 ms, reducing the size of the dataset while
1411 maintaining the overall trend in neural activity. This downsampled data was then used as input for
1412 subsequent analyses such as dimensionality reduction and regression.
1413 To enable fair comparisons of neural communication between brain regions, neuronal populations
1414 recorded in each area were matched based on their firing rates. The goal of this matching process was to
1415 control for variability in neural activity levels and ensure that equivalent neural populations were being
1416 compared across regions.

First, the mean spike rate of each neuron was calculated across all time points and event types. Neurons with low spike rates (< 0.1 Hz) were excluded from further analysis. Once this filtering step was complete, neurons belonging to one area were grouped into 10 equal-width bins according to their spike rate. The binning was conducted separately for the source and target neurons, resulting in a bin index for each neuron in the source area *X* ($b_X(i)$, for $i = 1, \dots, N_X$) and the target area *Y* (($b_Y(j)$, for $j = 1, \dots, N_Y$). Within each bin, neurons from the source and target areas were randomly paired. If the number of neurons in the source area within a particular bin N_X was larger than the number of neurons in the target area N_Y, or vice versa, the smaller of the two numbers was chosen so the number of neurons in each population would be matched. This random matching procedure was repeated 25 times for each pair of populations. When source and target dimensions belonged to the same brain region, neurons within the region were randomly split into two groups to serve as source and target populations. We then followed the same matching procedure as for cross-area comparisons.

Reduced Rank Regression with Ridge Regularization

After the neurons were matched across regions, reduced rank regression (*RRR*) was employed to analyze communication between the source and target areas. The relationship between the activity in the source population X and in the target population Y was modeled as:

$$Y = X\boldsymbol{B} + \epsilon$$

where $X \in R^{n \times p}$ represents the neural activity in a source population containing *p* neurons, $Y \in R^{n \times p}$represents the neural activity in the target population with the same number of neurons, $B \in R^{p \times p}$ is the matrix of regression coefficients, and ϵ is the noise term. To identify the most important communication dimensions we decomposed $\mathbf{B}$ into lower-dimensional components:

$$\boldsymbol{B} = \boldsymbol{UDV}^{\top}$$

where $U \in R^{p \times r}$ and $V \in R^{p \times r}$ are orthogonal matrices and $D \in R^{r \times r}$ is a diagonal matrix containing the singular values. The rank *r* was selected based on cross-validation as described below. To reduce overfitting, $\boldsymbol{B}$ was determined by applying a ridge regression model which minimized the following objective function:

$$\min_{B}\{|Y - X\mathbf{B}|^2 + \alpha|\mathbf{B}|^2\}$$

where α is a regularization parameter which controls the magnitude of the penalty on large coefficient values. To determine the optimal value of α, a grid search was conducted over 100 logarithmically spaced values from 10^{-5} to 10^{5}. The best α was chosen as the largest α within one standard error of the best-performing model across all α values using cross validation, ensuring that the model is regularized while maintaining predictive accuracy. The rank of the reduced regression model was varied from rank 2 to full rank, which varied depending on the number of neurons obtained after the matching procedure.

Cross-Validation and statistical testing

To assess the performance of the RRR models at different ranks, 10-fold cross-validation was used. In each fold, the dataset was split into training and testing sets, with the RRR model trained on the training set and evaluated on the test set. We measured each model's performance using including the Normalized Mean Squared Error (NMSE) calculated as:

$$NMSE = \frac{\sum\left(Y_{test} - Y_{pred}\right)^2}{\sum\left(Y_{test} - \overline{Y}_{test}\right)^2}$$

where Y_{test} is the observed activity in the test set, Y_{pred} is the predicted activity, and $\overline{Y}_{test}$ is the mean of the test set. Cross-validation was performed for each rank, generating average performance metrics and standard errors across 10 folds. The optimal rank was chosen as the smallest number of dimensions *r* where the 1-NMSE remained within one standard error of the mean from the best model.

To validate the robustness of the observed genotype effects, Monte Carlo permutation tests were conducted. The genotype labels of the matched neuron pairs were randomly shuffled, and the RRR models were re-fitted to generate a null distribution of performance metrics. The observed difference between WT and HET mice was compared to this null distribution to calculate a two-sided p-value. Each permutation test was repeated 10,000 times. A *Mann-Whitney U test* was used to compare the distributions of 1-NMSE scores and SEM ranks between WT and HET mice. To account for the large number of statistical comparisons, the *Holm-Bonferroni* correction was applied to the resulting p-values.

Statistics

Data analyses were conducted in GraphPad Prism (version 9.4.1, GraphPad Software) or custom Python scripts (version 3.9). Linear mixed models with repeated measures were used in passive and active WDIL experiments to determine differences in overall genotype performances and their learning differences within these tasks by assessing interactions between genotype and session progression during acquisition phases or angular velocity degression during "pullback" phases. ANOVAs and t tests were utilized to compare genotype differences within, between, or among different categories or stages of WDIL experiments, as well as NOR/T experiments, whisker kinematics comparisons, synaptic/circuit connectivity experiments and brain region-specific neural activity experiments. Kaplan-Meier survival curves were utilized to compare genotype differences in reaching endpoints, namely, reaching criteria for a particular stage of a WDIL task. Data are presented as mean ± SEM unless otherwise noted. D'Agostino-Pearson omnibus normality test was applied to test data normality and the appropriate parametric or non-parametric statistical test was performed accordingly. The statistical tests used and number of observations are reported explicitly in a comprehensive table **(Table S1)**. *P*-values are corrected for multiple comparisons when multiple simultaneously statistical comparisons were performed. No statistical test was used to predetermine sample sizes, however, our sample sizes are similar to those previously reported in the field [23,69].

1498 **References**

1499 1. Siegel, M., Buschman, T. J. & Miller, E. K. Cortical information flow during flexible
1500 sensorimotor decisions. *Science* **348**, 1352–1355 (2015).
1501 2. Pape, A.-A., Noury, N. & Siegel, M. Motor actions influence subsequent sensorimotor
1502 decisions. *Sci Rep* **7**, 15913 (2017).
1503 3. Huber, D. *et al.* Multiple dynamic representations in the motor cortex during sensorimotor
1504 learning. *Nature* **484**, 473–478 (2012).
1505 4. J.T. Wixted, J.T. Serences (Eds.), The Stevens Handbook of Experimental Psychology and
1506 Cognitive Neuroscience: Sensation, Perception, and Attention, Vol. II (2018). The neural
1507 basis of haptic perception. (2018).
1508 5. Karadimas, S. K. *et al.* Sensory cortical control of movement. *Nat Neurosci* **23**, 75–84 (2020).
1509 6. Yamawaki, N., Raineri Tapies, M. G., Stults, A., Smith, G. A. & Shepherd, G. M. Circuit
1510 organization of the excitatory sensorimotor loop through hand/forelimb S1 and M1. *eLife*
1511 **10**, e66836 (2021).
1512 7. Yu, C., Derdikman, D., Haidarliu, S. & Ahissar, E. Parallel Thalamic Pathways for Whisking
1513 and Touch Signals in the Rat. *PLOS Biology* **4**, e124 (2006).
1514 8. Diamond, M. E., von Heimendahl, M., Knutsen, P. M., Kleinfeld, D. & Ahissar, E. 'Where' and
1515 'what' in the whisker sensorimotor system. *Nat Rev Neurosci* **9**, 601–612 (2008).
1516 9. O'Connor, D. H., Krubitzer, L. & Bensmaia, S. Of mice and monkeys: Somatosensory
1517 processing in two prominent animal models. *Prog Neurobiol* 102008 (2021)
1518 doi:10.1016/j.pneurobio.2021.102008.

1519 10. Kleinfeld, D. & Deschênes, M. Neuronal Basis for Object Location in the Vibrissa Scanning
1520 Sensorimotor System. *Neuron* **72**, 455–468 (2011).
1521 11. Halley, A. C., Baldwin, M. K. L., Cooke, D. F., Englund, M. & Krubitzer, L. Distributed Motor
1522 Control of Limb Movements in Rat Motor and Somatosensory Cortex: The Sensorimotor
1523 Amalgam Revisited. *Cerebral Cortex* **30**, 6296–6312 (2020).
1524 12. Shepherd, G. M. G. & Yamawaki, N. Untangling the cortico-thalamo-cortical loop: cellular
1525 pieces of a knotty circuit puzzle. *Nat Rev Neurosci* **22**, 389–406 (2021).
1526 13. Dalton, K. M. *et al.* Gaze fixation and the neural circuitry of face processing in autism. *Nat*
1527 *Neurosci* **8**, 519–526 (2005).
1528 14. Gowen, E. & Hamilton, A. Motor abilities in autism: a review using a computational context.
1529 *J Autism Dev Disord* **43**, 323–344 (2013).
1530 15. Fournier, K. A., Hass, C. J., Naik, S. K., Lodha, N. & Cauraugh, J. H. Motor coordination in
1531 autism spectrum disorders: a synthesis and meta-analysis. *J Autism Dev Disord* **40**, 1227–
1532 1240 (2010).
1533 16. Abbruzzese, G. & Berardelli, A. Sensorimotor integration in movement disorders. *Mov*
1534 *Disord* **18**, 231–240 (2003).
1535 17. Tamilselvam, Y. K., Jog, M. & Patel, R. V. Robot-assisted investigation of sensorimotor
1536 control in Parkinson's disease. *Sci Rep* **13**, 4751 (2023).
1537 18. Neeper, R. & Greenwood, R. S. On the Psychiatric Importance of Neurological Soft Signs. in
1538 *Advances in Clinical Child Psychology* (eds. Lahey, B. B. & Kazdin, A. E.) 217–258 (Springer
1539 US, Boston, MA, 1987). doi:10.1007/978-1-4613-9826-4_6.

1540 19. Orefice, L. L. Outside-in: Rethinking the etiology of autism spectrum disorders. *Science* **366**,
1541 45–46 (2019).
1542 20. He, C. X. *et al.* Tactile Defensiveness and Impaired Adaptation of Neuronal Activity in the
1543 Fmr1 Knock-Out Mouse Model of Autism. *J Neurosci* **37**, 6475–6487 (2017).
1544 21. Burgdorf, J. S. *et al.* An IGFBP2-derived peptide promotes neuroplasticity and rescues
1545 deficits in a mouse model of Phelan-McDermid syndrome. *Mol Psychiatry* **28**, 1101–1111
1546 (2023).
1547 22. Orefice, L. L. *et al.* Targeting Peripheral Somatosensory Neurons to Improve Tactile-Related
1548 Phenotypes in ASD Models. *Cell* **178**, 867-886.e24 (2019).
1549 23. Michaelson, S. D. *et al.* SYNGAP1 heterozygosity disrupts sensory processing by reducing
1550 touch-related activity within somatosensory cortex circuits. *Nat Neurosci* **21**, 1–13 (2018).
1551 24. Klintwall, L. *et al.* Sensory abnormalities in autism: A brief report. *Research in*
1552 *Developmental Disabilities* **32**, 795–800 (2011).
1553 25. Marco, E. J., Hinkley, L. B. N., Hill, S. S. & Nagarajan, S. S. Sensory Processing in Autism: A
1554 Review of Neurophysiologic Findings. *Pediatr Res* **69**, 48–54 (2011).
1555 26. Robertson, C. E. & Baron-Cohen, S. Sensory perception in autism. *Nat Rev Neurosci* **18**, 671–
1556 684 (2017).
1557 27. Greven, C. U. *et al.* Sensory Processing Sensitivity in the context of Environmental
1558 Sensitivity: A critical review and development of research agenda. *Neuroscience &*
1559 *Biobehavioral Reviews* **98**, 287–305 (2019).
1560 28. Stevenson, R. A. *et al.* Multisensory Temporal Integration in Autism Spectrum Disorders. *J.*
1561 *Neurosci.* **34**, 691–697 (2014).

1562 29. Satterstrom, F. K. *et al.* Large-Scale Exome Sequencing Study Implicates Both
1563 Developmental and Functional Changes in the Neurobiology of Autism. *Cell* **180**, 568-
1564 584.e23 (2020).
1565 30. Staiger, J. F. & Petersen, C. C. H. Neuronal Circuits in Barrel Cortex for Whisker Sensory
1566 Perception. *Physiological Reviews* **101**, 353–415 (2021).
1567 31. Koshiyama, D. *et al.* Hierarchical Pathways from Sensory Processing to Cognitive, Clinical,
1568 and Functional Impairments in Schizophrenia. *Schizophr Bull* **47**, 373–385 (2021).
1569 32. Goel, A. *et al.* Impaired perceptual learning in a mouse model of Fragile X syndrome is
1570 mediated by parvalbumin neuron dysfunction and is reversible. *Nat Neurosci* **21**, 1404–
1571 1411 (2018).
1572 33. Pastor-Cerezuela, G., Fernández-Andrés, M.-I., Sanz-Cervera, P. & Marín-Suelves, D. The
1573 impact of sensory processing on executive and cognitive functions in children with autism
1574 spectrum disorder in the school context. *Research in Developmental Disabilities* **96**, 103540
1575 (2020).
1576 34. Lyons-Warren, A. M., McCormack, M. C. & Holder, J. L. Sensory Processing Phenotypes in
1577 Phelan-McDermid Syndrome and SYNGAP1-Related Intellectual Disability. *Brain Sci* **12**, 137
1578 (2022).
1579 35. Holder, J. L., Hamdan, F. F. & Michaud, J. L. SYNGAP1-Related Intellectual Disability. in
1580 *GeneReviews®* (eds. Adam, M. P. et al.) (University of Washington, Seattle, Seattle (WA),
1581 1993).
1582 36. Hamdan, F. F. *et al.* Mutations in SYNGAP1 in Autosomal Nonsyndromic Mental
1583 Retardation. *N Engl J Med* **360**, 599–605 (2009).

1584 37. Vlaskamp, D. R. M. *et al.* SYNGAP1 encephalopathy. *Neurology* **92**, e96–e107 (2019).
1585 38. Parker, M. J. *et al.* De novo, heterozygous, loss-of-function mutations in SYNGAP1 cause a
1586 syndromic form of intellectual disability. *Am J Med Genet A* **167**, 2231–2237 (2015).
1587 39. Mignot, C. *et al.* Genetic and neurodevelopmental spectrum of SYNGAP1-associated
1588 intellectual disability and epilepsy. *Journal of Medical Genetics* **53**, 511–522 (2016).
1589 40. Carreño-Muñoz, M. I. *et al.* Sensory processing dysregulations as reliable translational
1590 biomarkers in SYNGAP1 haploinsufficiency. *Brain* **145**, 754–769 (2022).
1591 41. Deng, Y.-T. *et al.* Large-scale whole-exome sequencing of neuropsychiatric diseases and
1592 traits in 350,770 adults. *Nat Hum Behav* **8**, 1194–1208 (2024).
1593 42. Nakajima, R. *et al.* Comprehensive behavioral analysis of heterozygous Syngap1 knockout
1594 mice. *Neuropsychopharmacol Rep* **39**, 223–237 (2019).
1595 43. Verschure, P. F. M. J., Pennartz, C. M. A. & Pezzulo, G. The why, what, where, when and
1596 how of goal-directed choice: neuronal and computational principles. *Philos Trans R Soc*
1597 *Lond B Biol Sci* **369**, 20130483 (2014).
1598 44. Zagha, E. *et al.* The Importance of Accounting for Movement When Relating Neuronal
1599 Activity to Sensory and Cognitive Processes. *J. Neurosci.* **42**, 1375–1382 (2022).
1600 45. Kleinfeld, D., Ahissar, E. & Diamond, M. E. Active sensation: insights from the rodent
1601 vibrissa sensorimotor system. *Curr Opin Neurobiol* **16**, 435–444 (2006).
1602 46. Feldmeyer, D. *et al.* Barrel cortex function. *Progress in Neurobiology* **103**, 3–27 (2013).
1603 47. Petersen, C. C. H. Sensorimotor processing in the rodent barrel cortex. *Nat Rev Neurosci* **20**,
1604 533–546 (2019).

1605 48. Esmaeili, V. *et al.* Cortical circuits for transforming whisker sensation into goal-directed
1606 licking. *Current Opinion in Neurobiology* **65**, 38–48 (2020).
1607 49. Petersen, C. C. H., Knott, G. W., Holtmaat, A. & Schürmann, F. Toward Biophysical
1608 Mechanisms of Neocortical Computation after 50 Years of Barrel Cortex Research. *Function*
1609 **2**, zqaa046 (2021).
1610 50. Sherman, D., Oram, T., Harel, D. & Ahissar, E. Attention Robustly Gates a Closed-Loop Touch
1611 Reflex. *Curr Biol* **27**, 1836-1843.e7 (2017).
1612 51. Llamosas, N. *et al.* Syngap1 regulates experience-dependent cortical ensemble plasticity by
1613 promoting in vivo excitatory synapse strengthening. *Proc Natl Acad Sci U S A* **118**,
1614 e2100579118 (2021).
1615 52. Zhao, M. & Kwon, S. E. Interneuron-Targeted Disruption of SYNGAP1 Alters Sensory
1616 Representations in the Neocortex and Impairs Sensory Learning. *J. Neurosci.* **43**, 6212–6226
1617 (2023).
1618 53. Yang, H., Kwon, S. E., Severson, K. S. & O'Connor, D. H. Origins of choice-related activity in
1619 mouse somatosensory cortex. *Nat Neurosci* **19**, 127–134 (2016).
1620 54. Gibson, J. J. Observations on active touch. *Psychological Review* **69**, 477–491 (1962).
1621 55. Szwed, M., Bagdasarian, K. & Ahissar, E. Encoding of Vibrissal Active Touch. *Neuron* **40**,
1622 621–630 (2003).
1623 56. Pluta, S. R., Lyall, E. H., Telian, G. I., Ryapolova-Webb, E. & Adesnik, H. Surround Integration
1624 Organizes a Spatial Map during Active Sensation. *Neuron* **94**, 1220-1233.e5 (2017).
1625 57. Xu, N. *et al.* Nonlinear dendritic integration of sensory and motor input during an active
1626 sensing task. *Nature* **492**, 247–251 (2012).

1627 58. O'Connor, D. H. *et al.* Vibrissa-Based Object Localization in Head-Fixed Mice. *J. Neurosci.* **30**,
1628 1947–1967 (2010).
1629 59. Mathis, A. *et al.* DeepLabCut: markerless pose estimation of user-defined body parts with
1630 deep learning. *Nat Neurosci* **21**, 1281–1289 (2018).
1631 60. Deutsch, D., Pietr, M., Knutsen, P. M., Ahissar, E. & Schneidman, E. Fast Feedback in Active
1632 Sensing: Touch-Induced Changes to Whisker-Object Interaction. *PLOS ONE* **7**, e44272
1633 (2012).
1634 61. Kim, J. H., Liao, D., Lau, L. F. & Huganir, R. L. SynGAP: a synaptic RasGAP that associates with
1635 the PSD-95/SAP90 protein family. *Neuron* **20**, 683–691 (1998).
1636 62. Porter, K., Komiyama, N. H., Vitalis, T., Kind, P. C. & Grant, S. G. N. Differential expression of
1637 two NMDA receptor interacting proteins, PSD-95 and SynGAP during mouse development.
1638 *Eur J Neurosci* **21**, 351–362 (2005).
1639 63. Ahissar, E. & Assa, E. Perception as a closed-loop convergence process. *eLife* **5**, e12830
1640 (2016).
1641 64. Petersen, C. C. H. The Functional Organization of the Barrel Cortex. *Neuron* **56**, 339–355
1642 (2007).
1643 65. Nguyen, Q.-T. & Kleinfeld, D. Positive feedback in a brainstem tactile sensorimotor loop.
1644 *Neuron* **45**, 447–457 (2005).
1645 66. Clement, J. P. *et al.* Pathogenic SYNGAP1 mutations impair cognitive development by
1646 disrupting maturation of dendritic spine synapses. *Cell* **151**, 709–723 (2012).
1647 67. Gorski, J. A. *et al.* Cortical Excitatory Neurons and Glia, But Not GABAergic Neurons, Are
1648 Produced in the Emx1-Expressing Lineage. *J. Neurosci.* **22**, 6309–6314 (2002).

1649 68. Luo, L. *et al.* Optimizing Nervous System-Specific Gene Targeting with Cre Driver Lines:
1650 Prevalence of Germline Recombination and Influencing Factors. *Neuron* **106**, 37-65.e5
1651 (2020).
1652 69. Yu, J., Hu, H., Agmon, A. & Svoboda, K. Recruitment of GABAergic Interneurons in the Barrel
1653 Cortex during Active Tactile Behavior. *Neuron* **104**, 412-427.e4 (2019).
1654 70. Mitchinson, B. *et al.* Active vibrissal sensing in rodents and marsupials. *Philosophical*
1655 *Transactions of the Royal Society B: Biological Sciences* **366**, 3037–3048 (2011).
1656 71. Semedo, J. D., Zandvakili, A., Machens, C. K., Yu, B. M. & Kohn, A. Cortical Areas Interact
1657 through a Communication Subspace. *Neuron* **102**, 249-259.e4 (2019).
1658 72. Manita, S. *et al.* A Top-Down Cortical Circuit for Accurate Sensory Perception. *Neuron* **86**,
1659 1304–1316 (2015).
1660 73. Feldmeyer, D. Excitatory neuronal connectivity in the barrel cortex. *Front Neuroanat* **6**, 24
1661 (2012).
1662 74. Aceti, M. *et al.* Syngap1 haploinsufficiency damages a postnatal critical period of pyramidal
1663 cell structural maturation linked to cortical circuit assembly. *Biol Psychiatry* **77**, 805–815
1664 (2015).
1665 75. Miyamichi, K. *et al.* Dissecting local circuits: parvalbumin interneurons underlie broad
1666 feedback control of olfactory bulb output. *Neuron* **80**, 1232–1245 (2013).
1667 76. Fürth, D. *et al.* An interactive framework for whole-brain maps at cellular resolution. *Nat*
1668 *Neurosci* **21**, 139–149 (2018).
1669 77. Arenkiel, B. R. *et al.* In vivo light-induced activation of neural circuitry in transgenic mice
1670 expressing channelrhodopsin-2. *Neuron* **54**, 205–218 (2007).

1671 78. Barco, T. L. *et al.* SYNGAP1-related developmental and epileptic encephalopathy: The
1672 impact on daily life. *Epilepsy Behav* **127**, (2022).
1673 79. Schaffler, M. D., Middleton, L. J. & Abdus-Saboor, I. Mechanisms of Tactile Sensory
1674 Phenotypes in Autism: Current Understanding and Future Directions for Research. *Curr*
1675 *Psychiatry Rep* **21**, 134 (2019).
1676 80. Orefice, L. L. Peripheral Somatosensory Neuron Dysfunction: Emerging Roles in Autism
1677 Spectrum Disorders. *Neuroscience* **445**, 120–129 (2020).
1678 81. Chen, Q. *et al.* Dysfunction of cortical GABAergic neurons leads to sensory hyper-reactivity
1679 in a Shank3 mouse model of ASD. *Nat Neurosci* **23**, 520–532 (2020).
1680 82. Orefice, L. L. *et al.* Peripheral Mechanosensory Neuron Dysfunction Underlies Tactile and
1681 Behavioral Deficits in Mouse Models of ASDs. *Cell* **166**, 299–313 (2016).
1682 83. Cascio, C. J. Somatosensory processing in neurodevelopmental disorders. *J Neurodevelop*
1683 *Disord* **2**, 62–69 (2010).
1684 84. He, J. L. *et al.* Disorder-specific alterations of tactile sensitivity in neurodevelopmental
1685 disorders. *Commun Biol* **4**, 1–15 (2021).
1686 85. Jung, J. *et al.* Associations between physiological and neural measures of sensory reactivity
1687 in youth with autism. *J Child Psychol Psychiatry* **62**, 1183–1194 (2021).
1688 86. SFARI | Approaches for measuring sensory function in ASD/NDD. *SFARI*
1689 https://www.sfari.org/2023/04/25/approaches-for-measuring-sensory-function-in-asd-
1690 ndd/ (2023).

1691 87. Cohen, J. D., Hirata, A. & Castro-Alamancos, M. A. Vibrissa sensation in superior colliculus:
1692 wide-field sensitivity and state-dependent cortical feedback. *J Neurosci* **28**, 11205–11220
1693 (2008).
1694 88. Kilinc, M. *et al.* Species-conserved SYNGAP1 phenotypes associated with
1695 neurodevelopmental disorders. *Molecular and Cellular Neuroscience* **91**, 140–150 (2018).
1696 89. Kilinc, M. *et al.* Endogenous Syngap1 alpha splice forms promote cognitive function and
1697 seizure protection. *eLife* **11**, e75707 (2022).
1698 90. Kim, J. H., Lee, H.-K., Takamiya, K. & Huganir, R. L. The role of synaptic GTPase-activating
1699 protein in neuronal development and synaptic plasticity. *J Neurosci* **23**, 1119–1124 (2003).
1700 91. Slotnick, B. A simple 2-transistor touch or lick detector circuit. *J Exp Anal Behav* **91**, 253–255
1701 (2009).
1702 92. Tuscher, J. J., Fortress, A. M., Kim, J. & Frick, K. M. Regulation of object recognition and
1703 object placement by ovarian sex steroid hormones. *Behav Brain Res* **285**, 140–157 (2015).
1704 93. Clack, N. G. *et al.* Automated Tracking of Whiskers in Videos of Head Fixed Rodents. *PLoS*
1705 *Comput Biol* **8**, e1002591 (2012).
1706 94. Pammer, L. *et al.* The mechanical variables underlying object localization along the axis of
1707 the whisker. *J Neurosci* **33**, 6726–6741 (2013).
1708 95. Severson, K. S. *et al.* Active Touch and Self-Motion Encoding by Merkel Cell-Associated
1709 Afferents. *Neuron* **94**, 666-676.e9 (2017).
1710 96. Shamash, P., Carandini, M., Harris, K. & Steinmetz, N. A tool for analyzing electrode tracks
1711 from slice histology. 447995 Preprint at https://doi.org/10.1101/447995 (2018).

1712 97. Harrison, T. C., Sigler, A. & Murphy, T. H. Simple and cost-effective hardware and software
1713 for functional brain mapping using intrinsic optical signal imaging. *Journal of Neuroscience*
1714 *Methods* **182**, 211–218 (2009).
1715
1716
1717
1718
1719

1720

Figure1

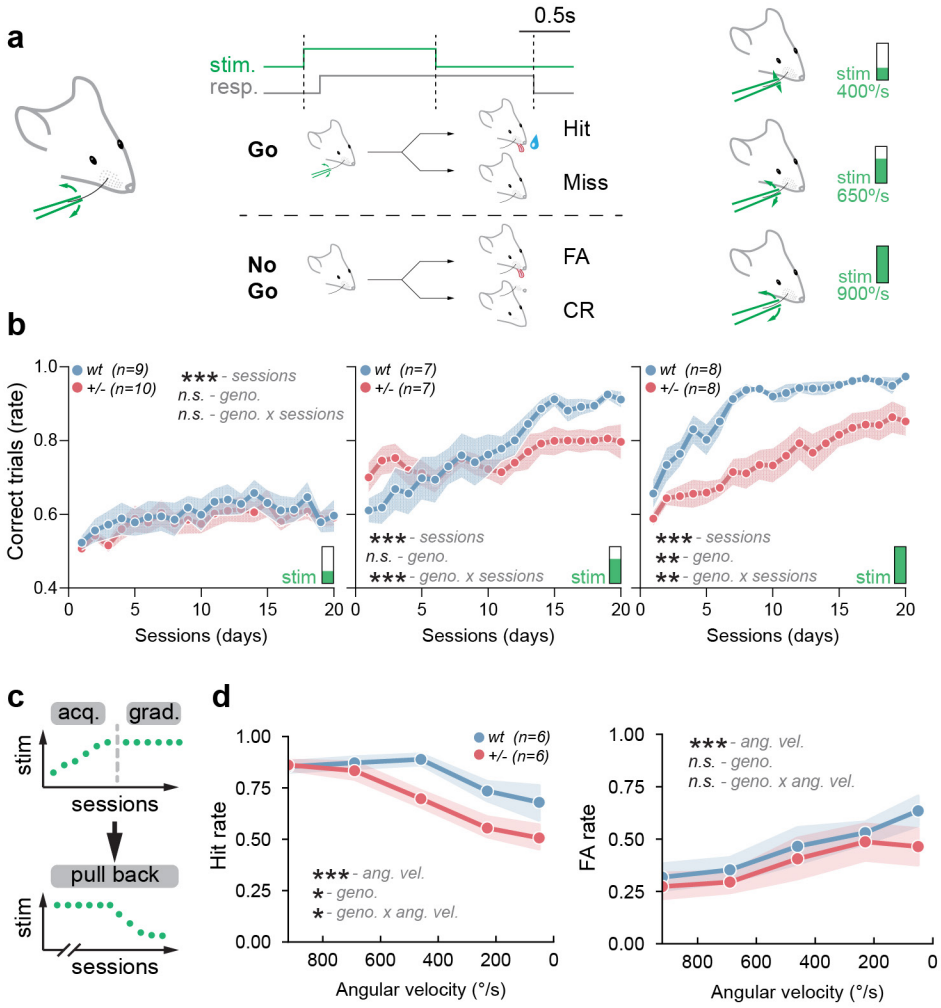
a
0.5s
stim.
resp.
Go
Hit
Miss
No Go
FA
CR
stim 400°/s
stim 650°/s
stim 900°/s
b
wt (n=9)
+/- (n=10)
*** - sessions
n.s. - geno.
n.s. - geno. x sessions
wt (n=7)
+/- (n=7)
*** - sessions
n.s. - geno.
*** - geno. x sessions
wt (n=8)
+/- (n=8)
*** - sessions
** - geno.
** - geno. x sessions
Correct trials (rate)
Sessions (days)
stim
c
acq.
grad.
stim
sessions
pull back
d
wt (n=6)
+/- (n=6)
*** - ang. vel.
* - geno.
* - geno. x ang. vel.
Hit rate
Angular velocity (°/s)
*** - ang. vel.
n.s. - geno.
n.s. - geno. x ang. vel.
FA rate

Figure2

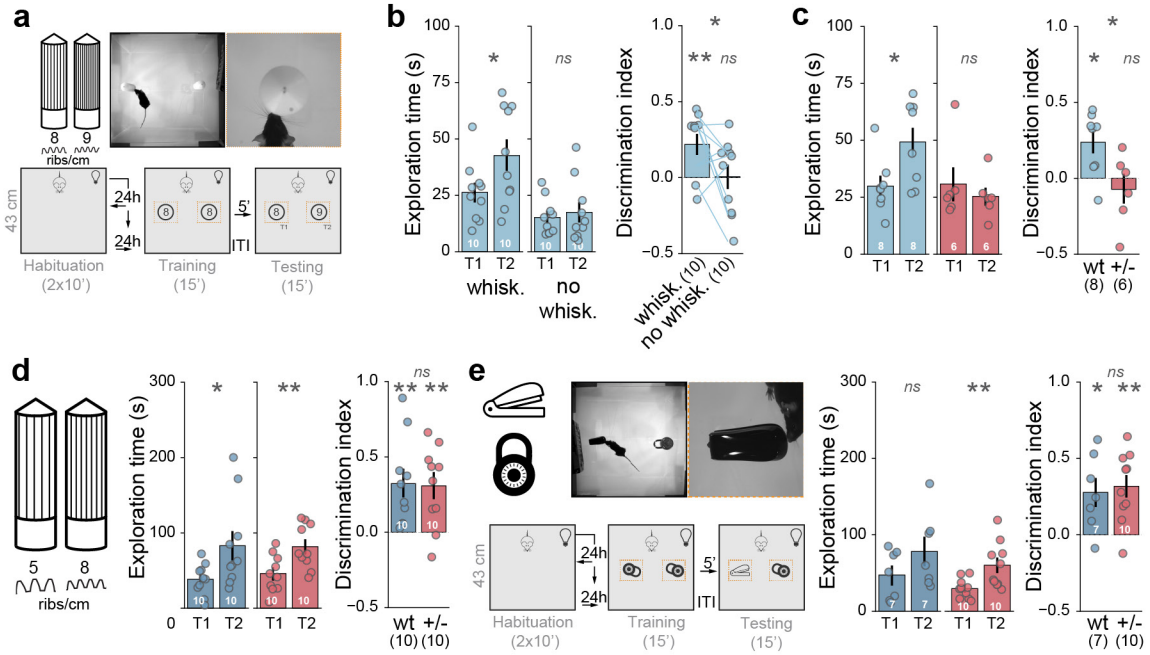
a
8 9
ribs/cm
43 cm
24h
24h
5'
ITI
Habituation (2x10')
Training (15')
Testing (15')
b
Exploration time (s)
T1 T2 T1 T2
whisk.
no whisk.
Discrimination index
whisk. (10)
no whisk. (10)
c
wt (8)
+/- (6)
d
5 8
ribs/cm
wt (10)
+/- (10)
e
wt (7)
+/- (10)

Figure3

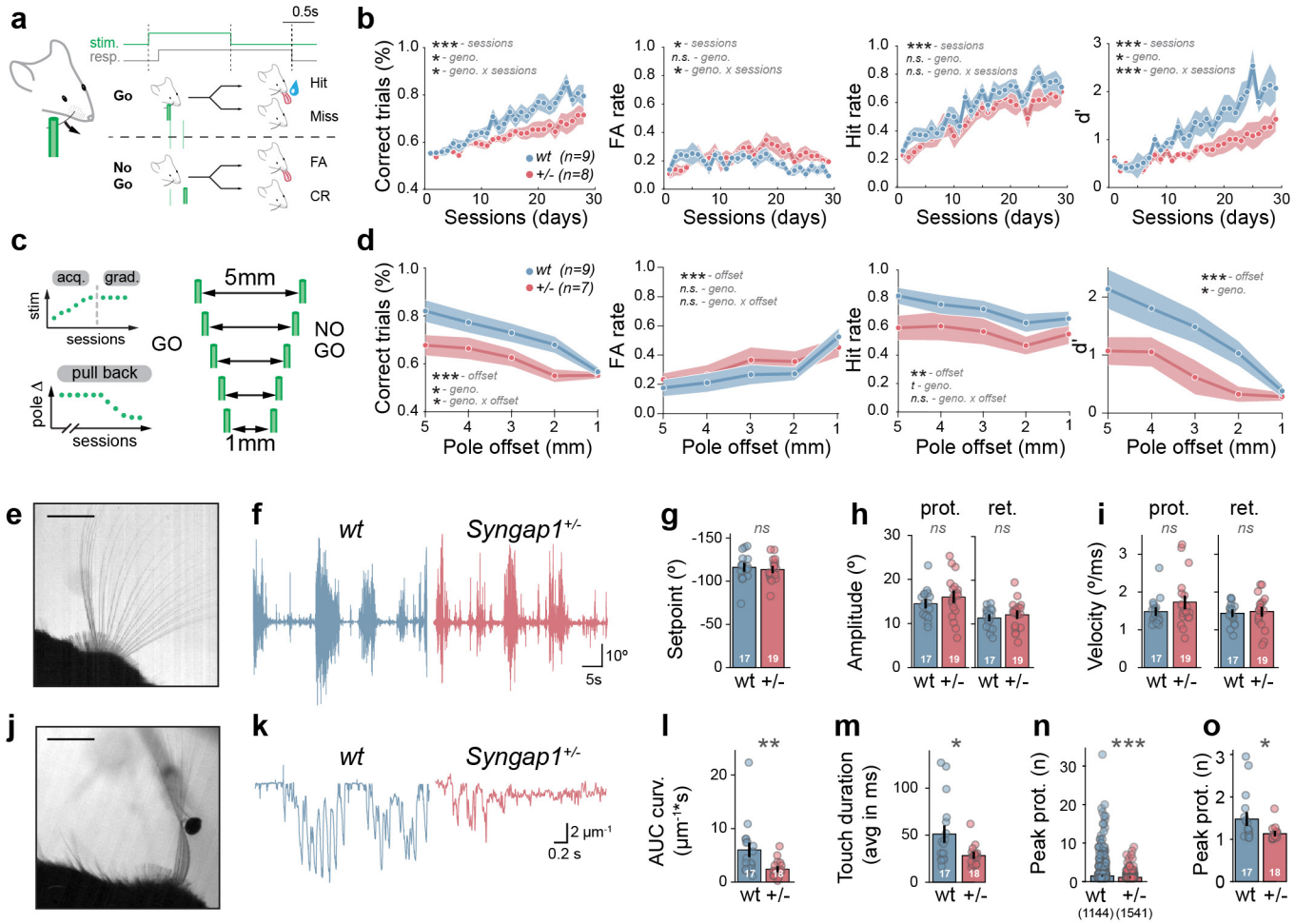
a
0.5s
stim.
resp.
Go
Hit
Miss
No Go
FA
CR
b
Correct trials (%)
*** - sessions
* - geno.
* - geno. x sessions
wt (n=9)
+/- (n=8)
Sessions (days)
FA rate
* - sessions
n.s. - geno.
* - geno. x sessions
Hit rate
*** - sessions
n.s. - geno.
n.s. - geno. x sessions
d'
*** - sessions
* - geno.
*** - geno. x sessions
c
acq.
grad.
stim
sessions
GO
pull back
pole Δ
sessions
5mm
NO GO
1mm
d
Correct trials (%)
wt (n=9)
+/- (n=7)
*** - offset
* - geno.
* - geno. x offset
Pole offset (mm)
FA rate
*** - offset
n.s. - geno.
n.s. - geno. x offset
Hit rate
** - offset
t - geno.
n.s. - geno. x offset
d'
*** - offset
* - geno.
e
f
wt
Syngap1+/-
10°
5s
g
Setpoint (°)
ns
wt +/-
h
prot.
ret.
Amplitude (°)
ns
i
Velocity (°/ms)
j
k
wt
Syngap1+/-
2 µm-1
0.2 s
l
AUC curv. (µm-1*s)
**
m
Touch duration (avg in ms)
*
n
Peak prot. (n)
***
(1144) (1541)
o
Peak prot. (n)
*

Figure4

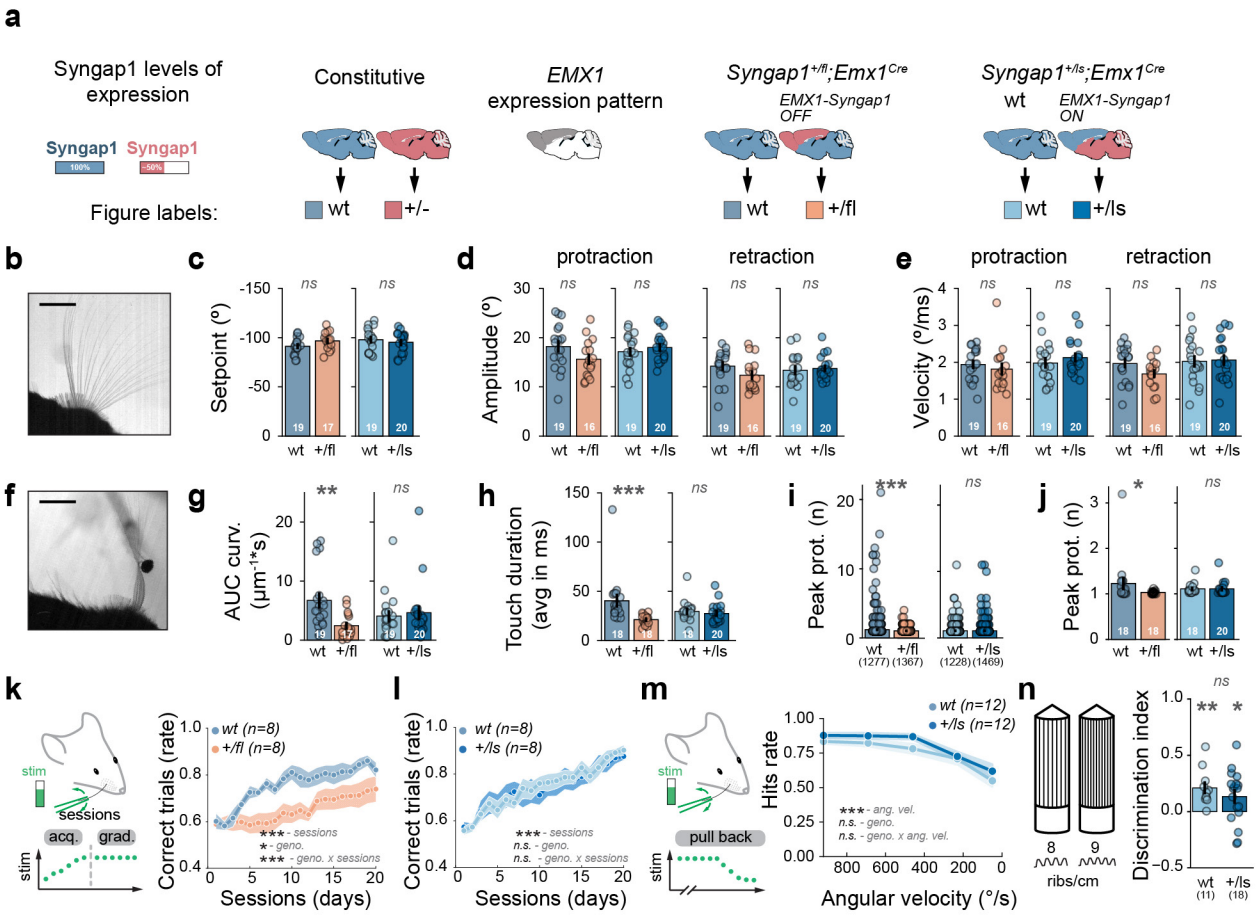
a
Syngap1 levels of expression
Syngap1
Syngap1
Figure labels:
Constitutive
wt
+/-
EMX1 expression pattern
Syngap1+/fl;Emx1Cre
EMX1-Syngap1 OFF
wt
+/fl
Syngap1+/ls;Emx1Cre
wt
EMX1-Syngap1 ON
wt
+/ls
b
c
Setpoint (°)
d
protraction
retraction
Amplitude (°)
e
Velocity (°/ms)
f
g
AUC curv. (µm-1*s)
h
Touch duration (avg in ms)
i
Peak prot. (n)
j
Peak prot. (n)
k
stim
sessions
acq.
grad.
Correct trials (rate)
wt (n=8)
+/fl (n=8)
*** - sessions
* - geno.
*** - geno. x sessions
Sessions (days)
l
Correct trials (rate)
wt (n=8)
+/ls (n=8)
*** - sessions
n.s. - geno.
n.s. - geno. x sessions
Sessions (days)
m
stim
pull back
Hits rate
wt (n=12)
+/ls (n=12)
*** - ang. vel.
n.s. - geno.
n.s. - geno. x ang. vel.
Angular velocity (°/s)
n
ribs/cm
Discrimination index

Figure5

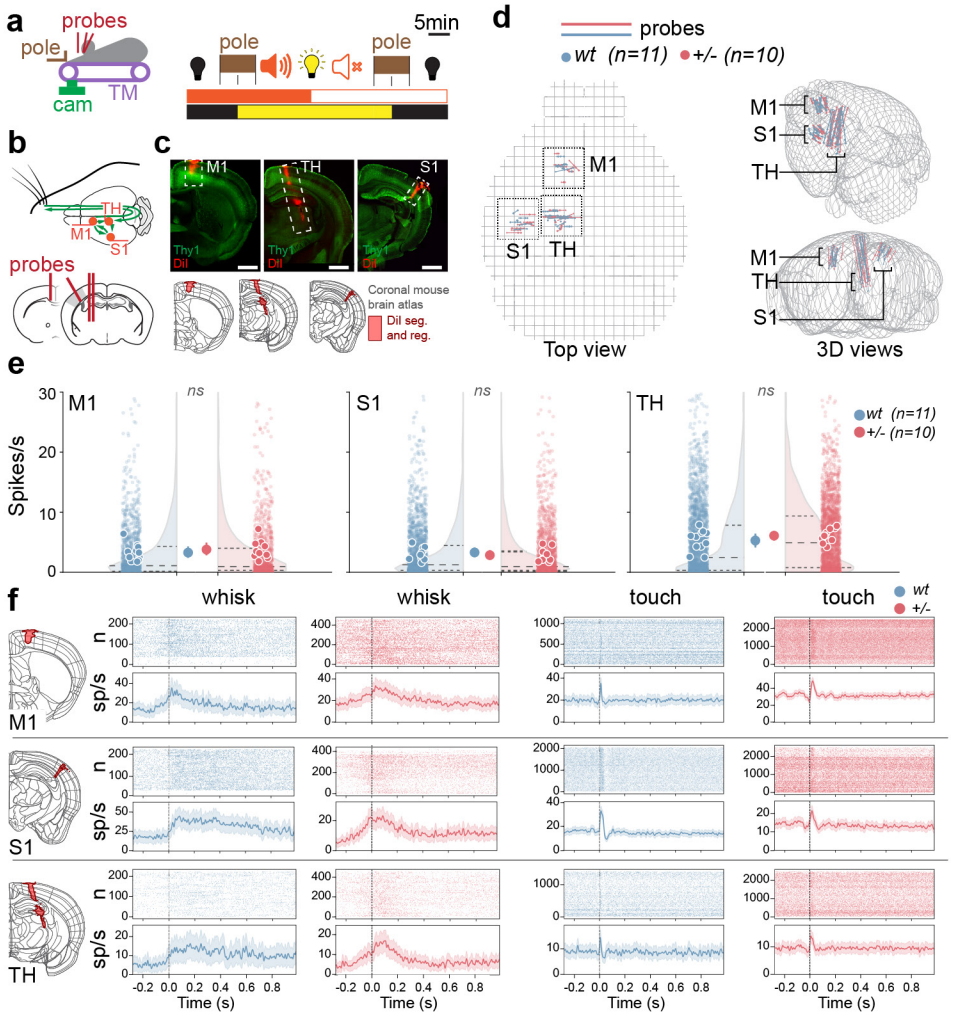
a
probes
pole
TM
cam
pole
pole
5min
b
TH
M1
S1
probes
c
M1
TH
S1
Thy1
DiI
Coronal mouse brain atlas
DiI seg. and reg.
d
probes
wt (n=11)
+/- (n=10)
M1
S1
TH
Top view
3D views
e
M1
S1
TH
ns
Spikes/s
wt (n=11)
+/- (n=10)
f
whisk
whisk
touch
touch
wt
+/-
n
sp/s
Time (s)

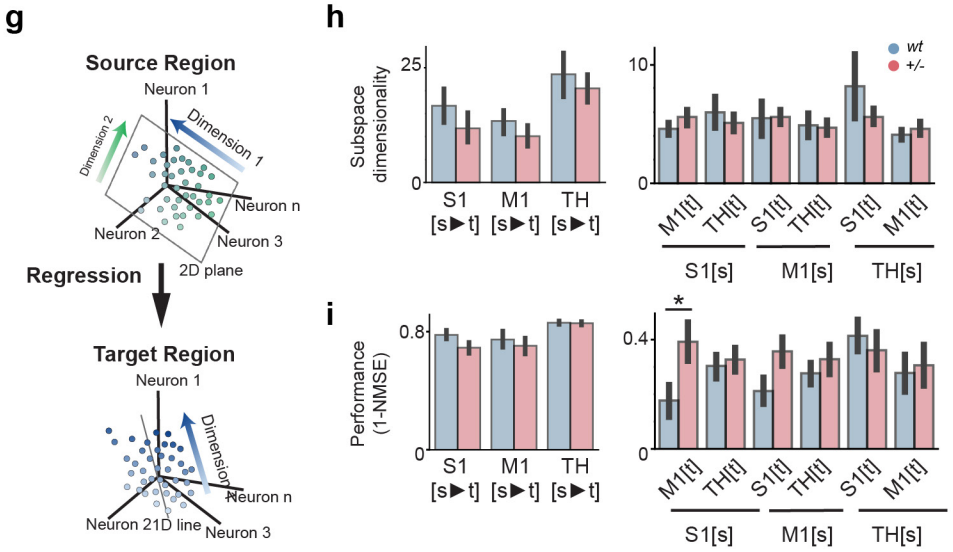
g
Source Region
Neuron 1
Dimension 1
Dimension 2
Neuron n
Neuron 2
Neuron 3
2D plane
Regression
Target Region
Neuron 1
Dimension 1
Neuron n
Neuron 21D line
Neuron 3
h
Subspace dimensionality
wt
+/-
S1 [s▶t]
M1 [s▶t]
TH [s▶t]
M1[t]
TH[t]
S1[t]
TH[t]
S1[t]
M1[t]
S1[s]
M1[s]
TH[s]
i
Performance (1-NMSE)
*

Figure6

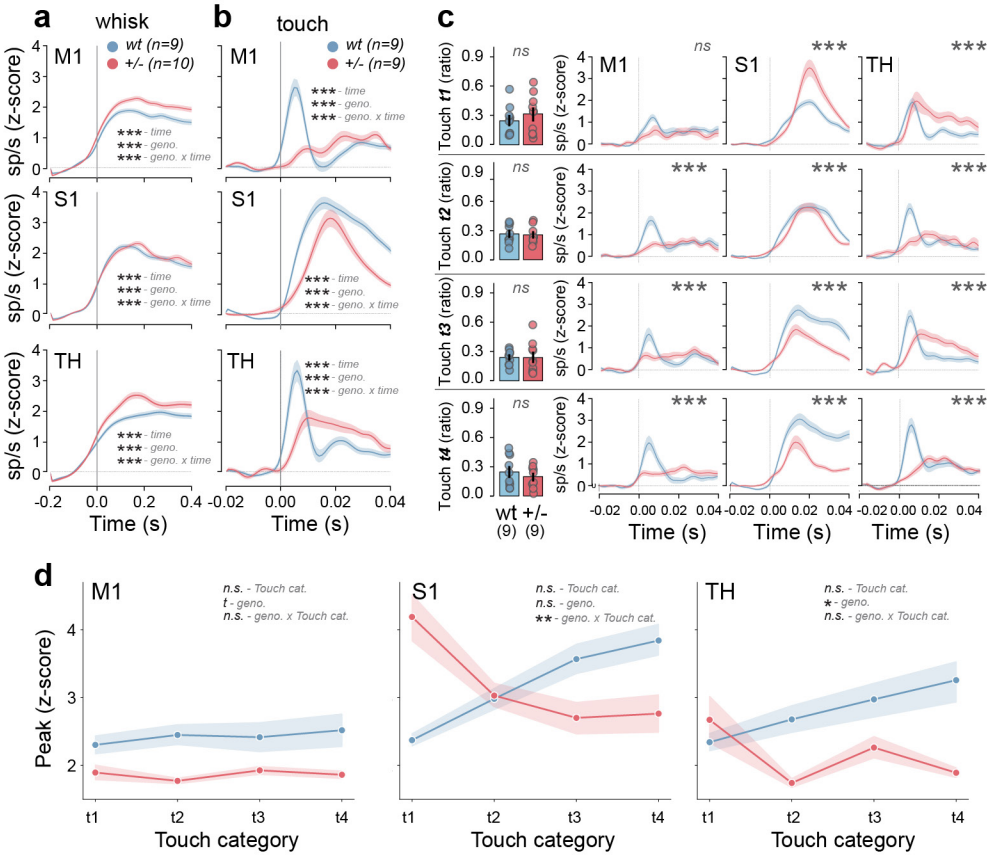
a
whisk
b
touch
c
M1
S1
TH
wt (n=9)
+/- (n=10)
+/- (n=9)
*** - time
*** - geno.
*** - geno. x time
sp/s (z-score)
Time (s)
Touch t1 (ratio)
Touch t2 (ratio)
Touch t3 (ratio)
Touch t4 (ratio)
ns
wt +/-
(9) (9)

d
M1
S1
TH
n.s. - Touch cat.
t - geno.
n.s. - geno. x Touch cat.
n.s. - Touch cat.
n.s. - geno.
** - geno. x Touch cat.
n.s. - Touch cat.
* - geno.
n.s. - geno. x Touch cat.
Peak (z-score)
t1
t2
t3
t4
Touch category

Figure7

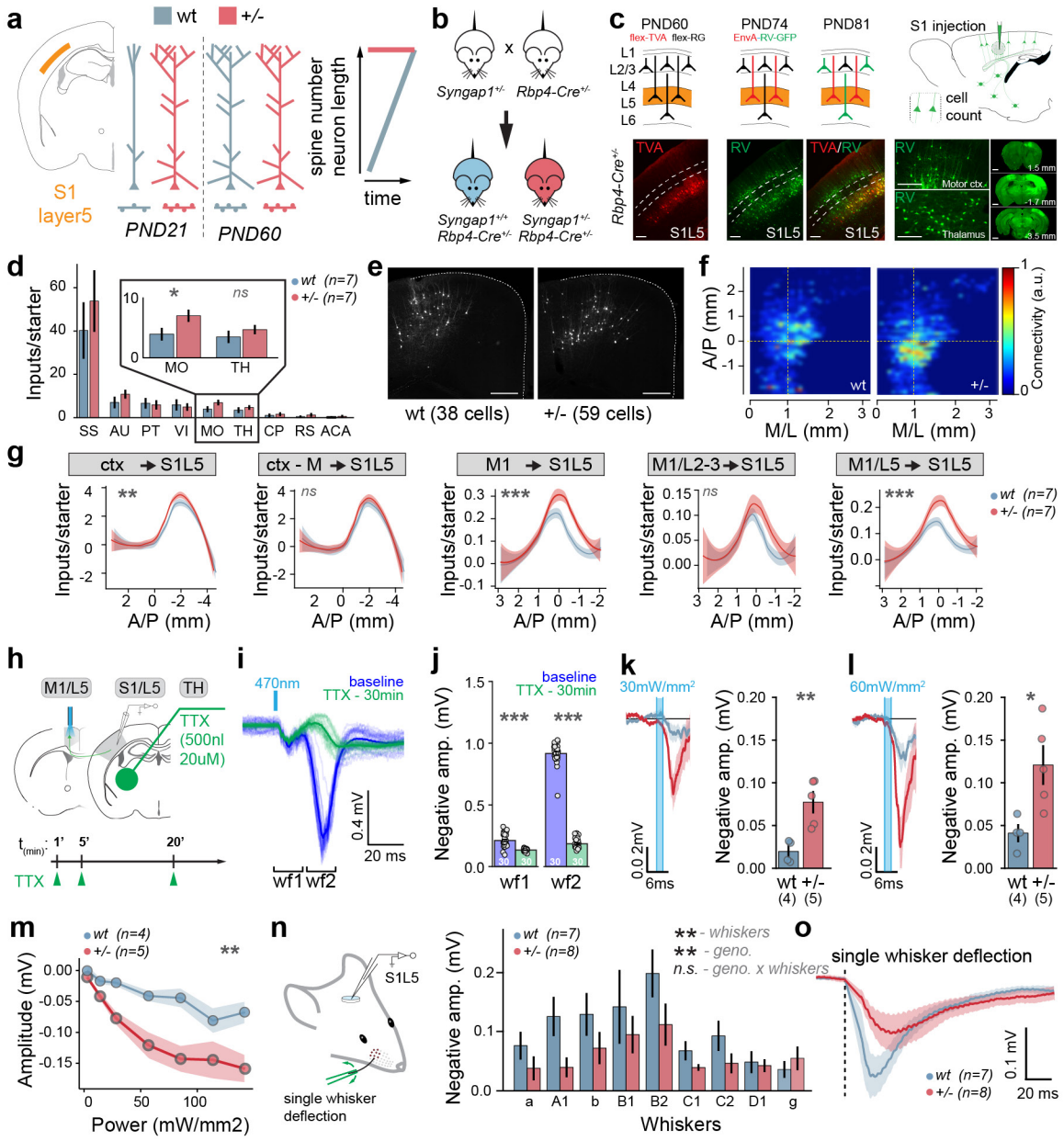
a
wt
+/-
S1
layer5
PND21
PND60
spine number
neuron length
time
b
Syngap1+/-
Rbp4-Cre+/-
Syngap1+/+
Rbp4-Cre+/-
Syngap1+/-
Rbp4-Cre+/-
c
PND60
PND74
PND81
S1 injection
flex-TVA
flex-RG
EnvA-RV-GFP
L1
L2/3
L4
L5
L6
cell
count
TVA
RV
TVA/RV
S1L5
Motor ctx.
Thalamus
1.5 mm
-1.7 mm
-3.5 mm
d
Inputs/starter
wt (n=7)
+/- (n=7)
MO
TH
SS
AU
PT
VI
CP
RS
ACA
e
wt (38 cells)
+/- (59 cells)
f
A/P (mm)
M/L (mm)
Connectivity (a.u.)
wt
+/-
g
ctx → S1L5
ctx - M → S1L5
M1 → S1L5
M1/L2-3 → S1L5
M1/L5 → S1L5
Inputs/starter
A/P (mm)
h
M1/L5
S1/L5
TH
TTX
(500nl
20uM)
t(min): 1'
5'
20'
TTX
i
470nm
baseline
TTX - 30min
0.4 mV
20 ms
wf1
wf2
j
baseline
TTX - 30min
Negative amp. (mV)
wf1
wf2
k
30mW/mm2
0.2mV
6ms
Negative amp. (mV)
wt
+/-
(4)
(5)
l
60mW/mm2
0.2mV
6ms
Negative amp. (mV)
wt
+/-
(4)
(5)
m
wt (n=4)
+/- (n=5)
Amplitude (mV)
Power (mW/mm2)
n
S1L5
single whisker
deflection
Negative amp. (mV)
wt (n=7)
+/- (n=8)
** - whiskers
** - geno.
n.s. - geno. x whiskers
a
A1
b
B1
B2
C1
C2
D1
g
Whiskers
o
single whisker deflection
wt (n=7)
+/- (n=8)
0.1 mV
20 ms

Figure 8

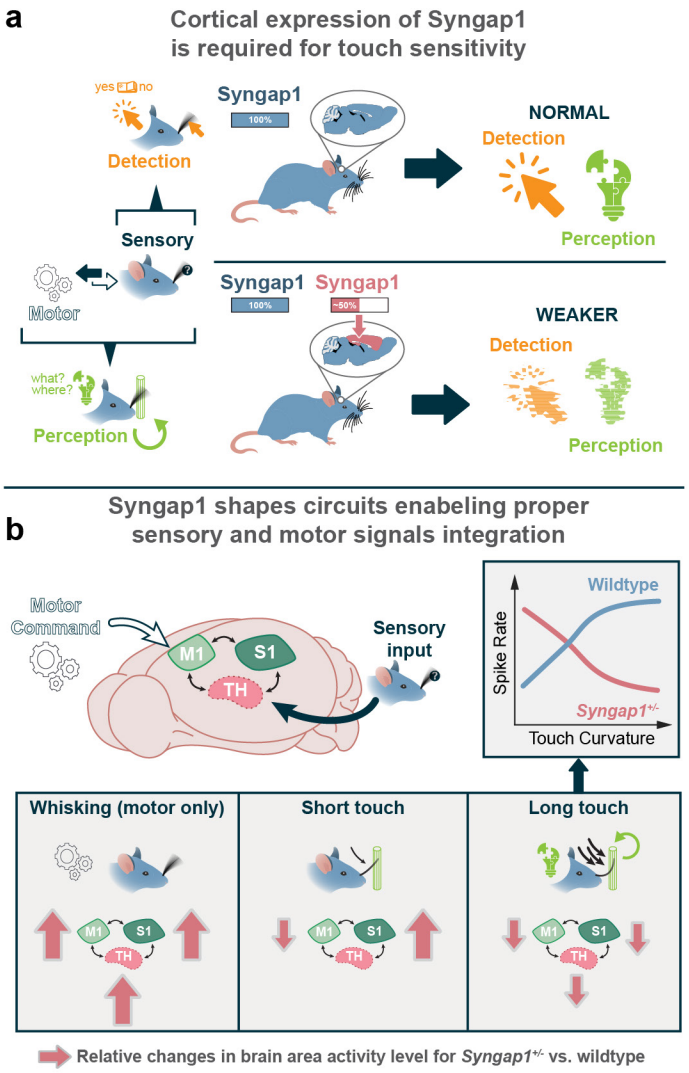
a
Cortical expression of Syngap1 is required for touch sensitivity
yes no
Detection
Sensory
Motor
what? where?
Perception
Syngap1
100%
NORMAL
Detection
Perception
Syngap1
Syngap1
100%
~50%
WEAKER
Detection
Perception
b
Syngap1 shapes circuits enabeling proper sensory and motor signals integration
Motor Command
M1
S1
TH
Sensory input
Wildtype
Spike Rate
Syngap1+/-
Touch Curvature
Whisking (motor only)
Short touch
Long touch
Relative changes in brain area activity level for Syngap1+/- vs. wildtype

Supplementary Figure 1 *(related to Figure1)*

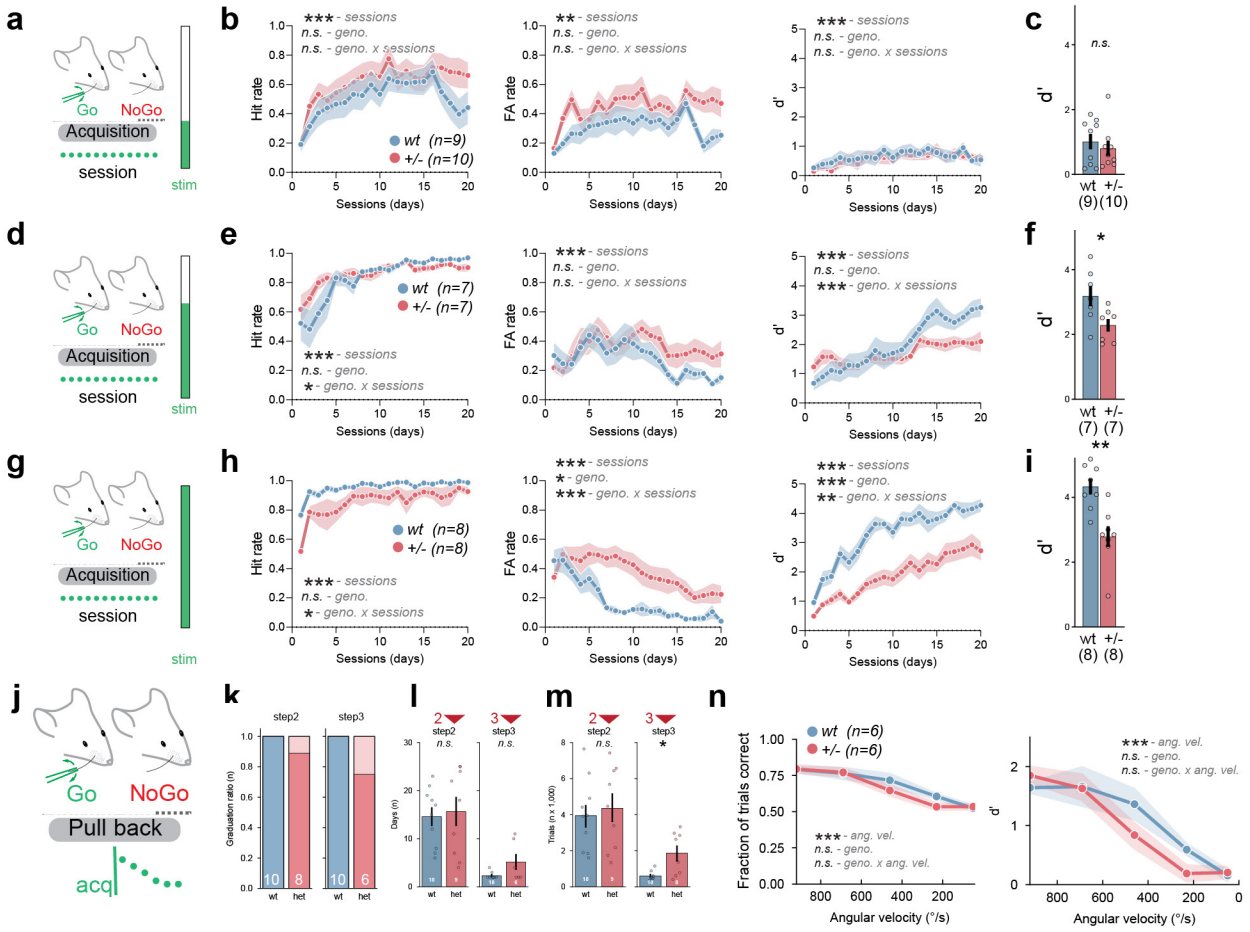

Supplementary Figure 2 *(related to Figure3)*

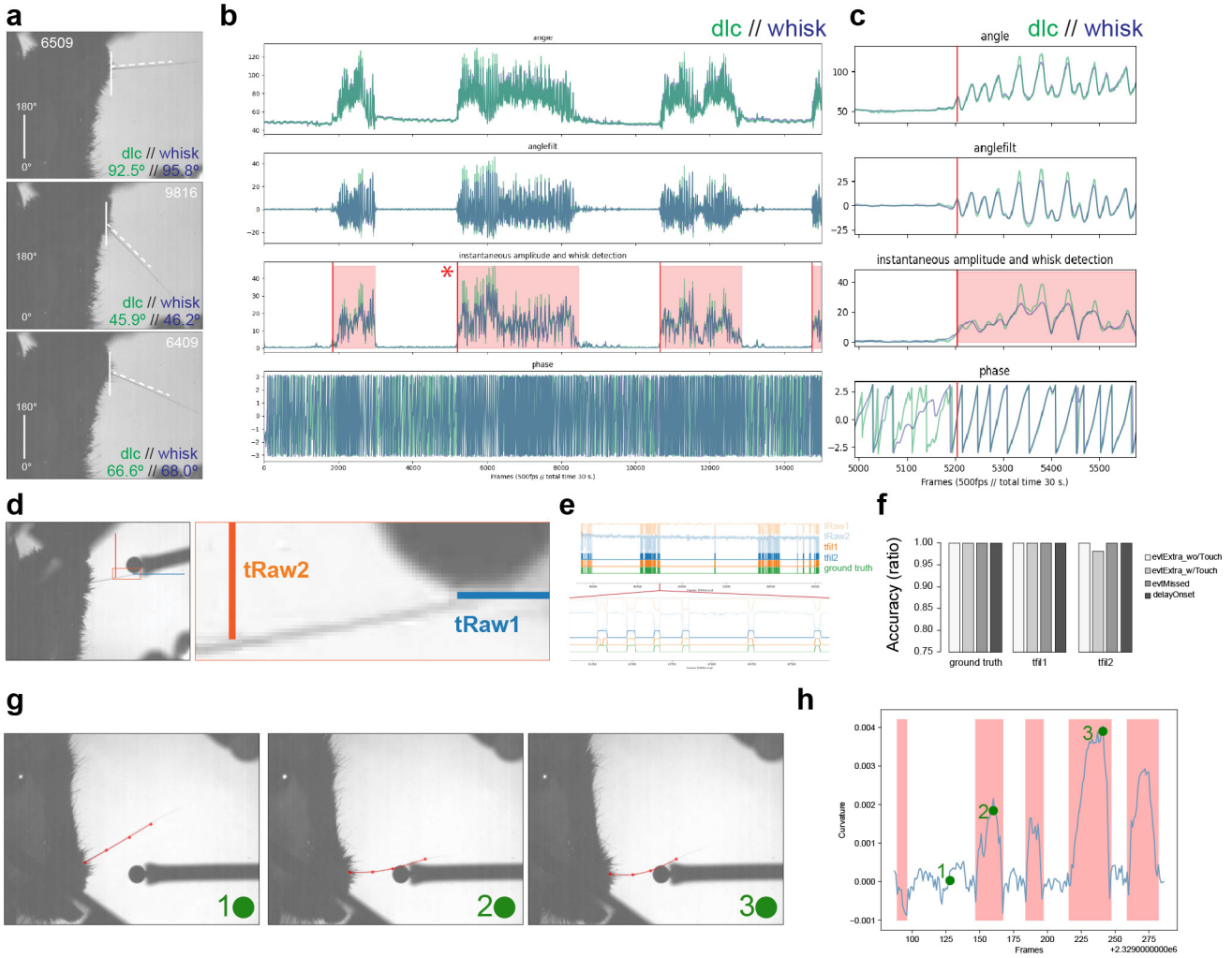

Supplementary Figure 3 *(related to Figure3)*

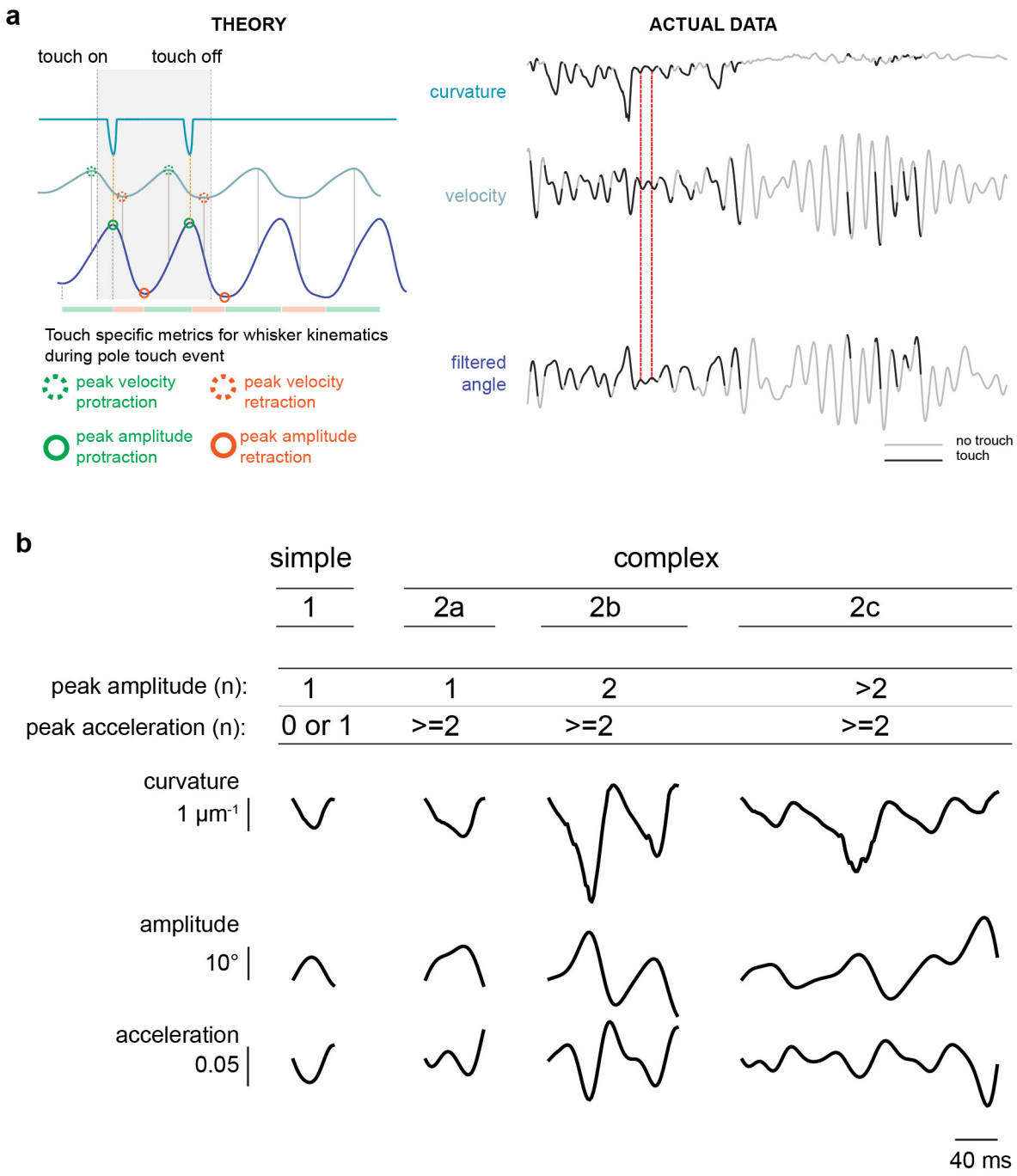

Supplementary Figure 4 *(related to Figure4)*

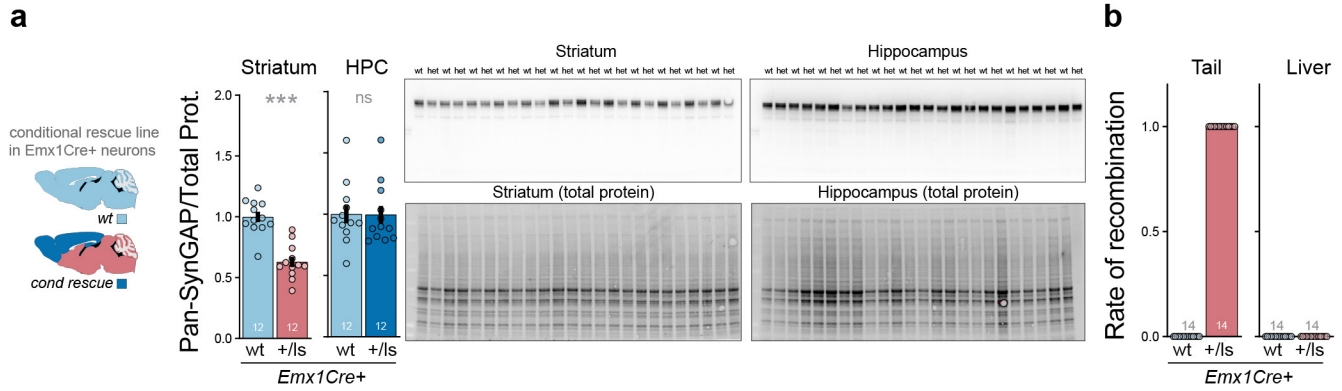

Supplementary Figure 5 *(related to Figure4)*

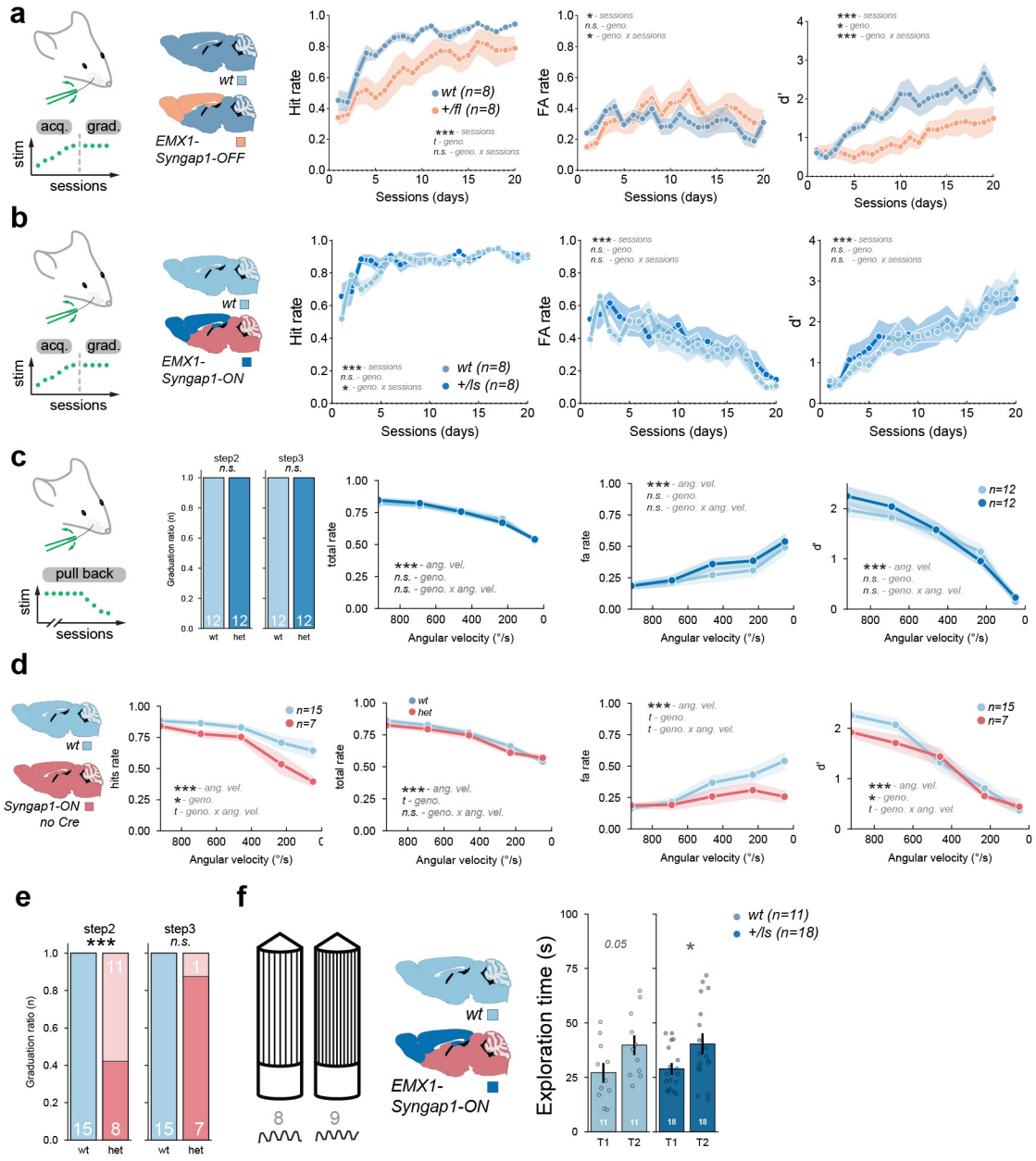

Supplementary Figure 6 *(related to Figure5)*

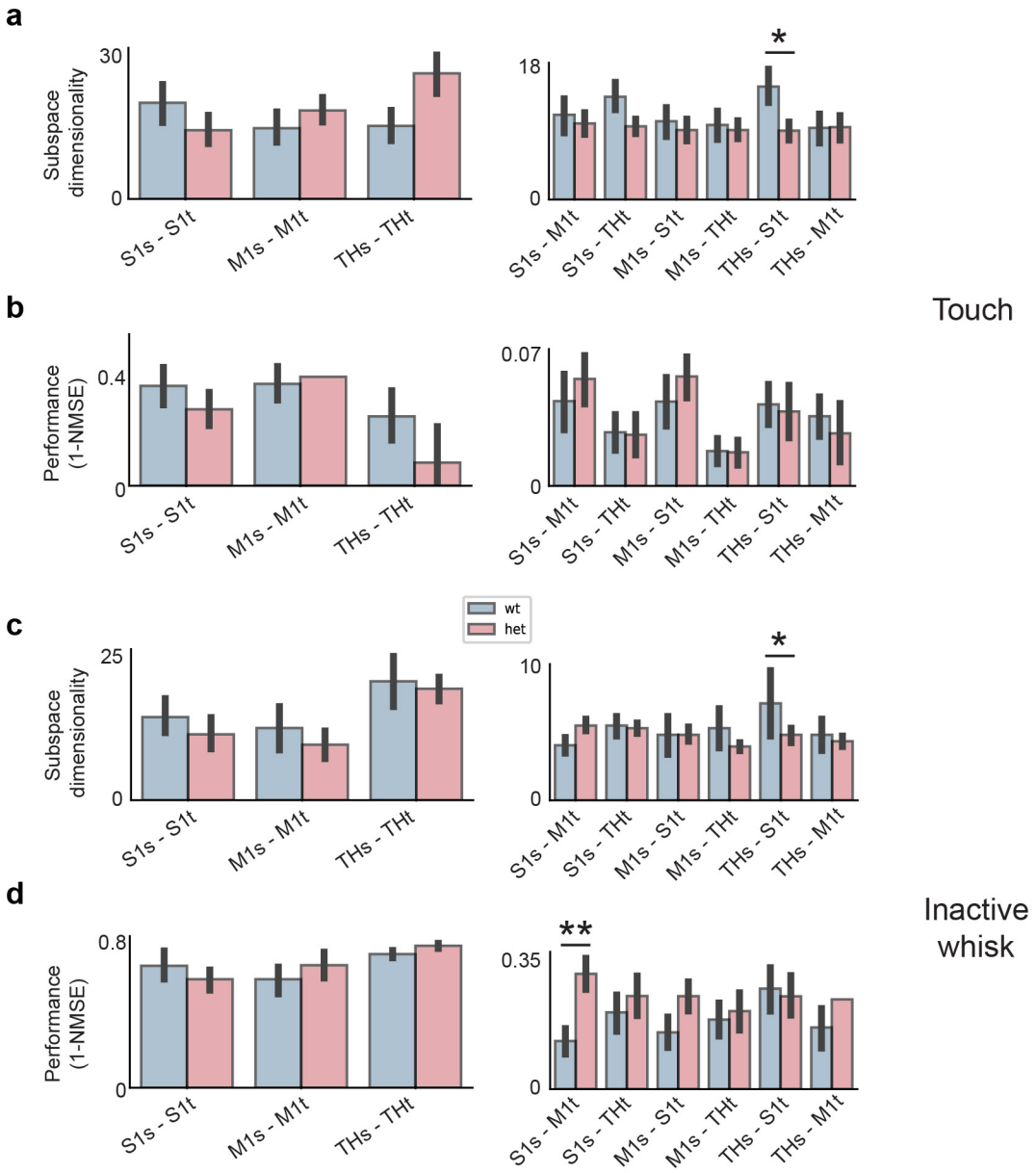

Supplementary Figure 7

(related to Figure 5 and 6)

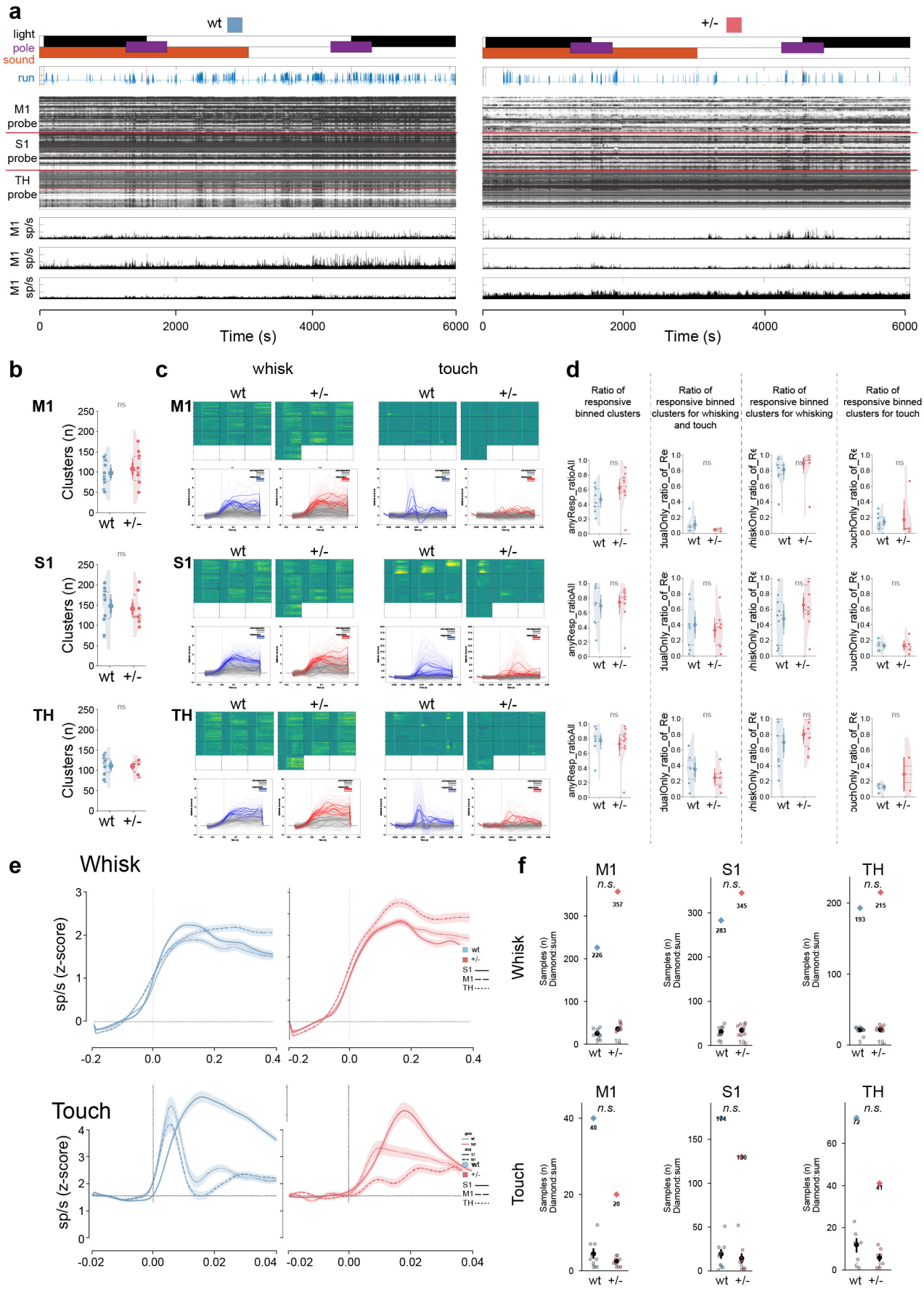

Supplementary Figure 8 *(related to Figure 5 and 6)*

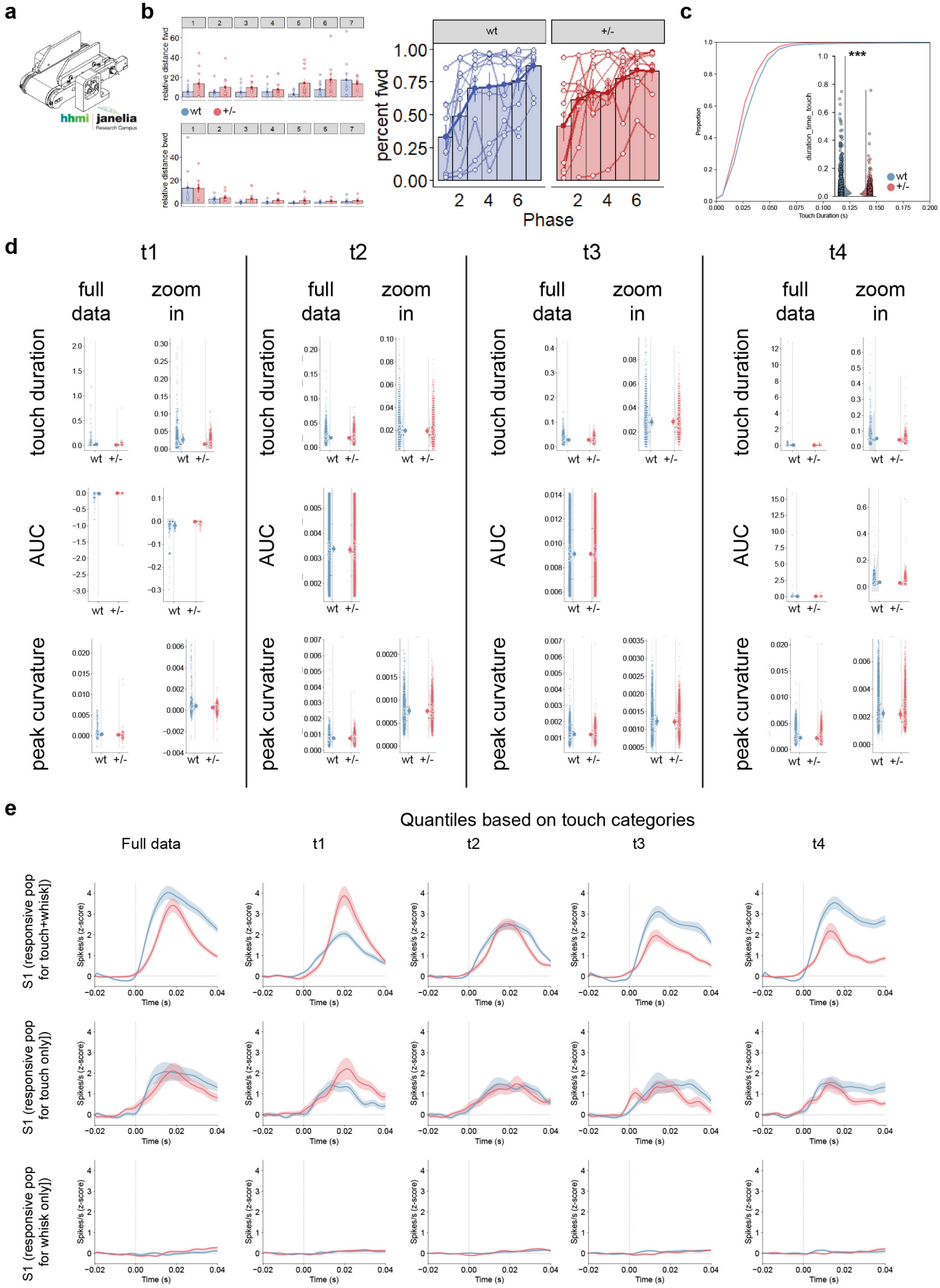
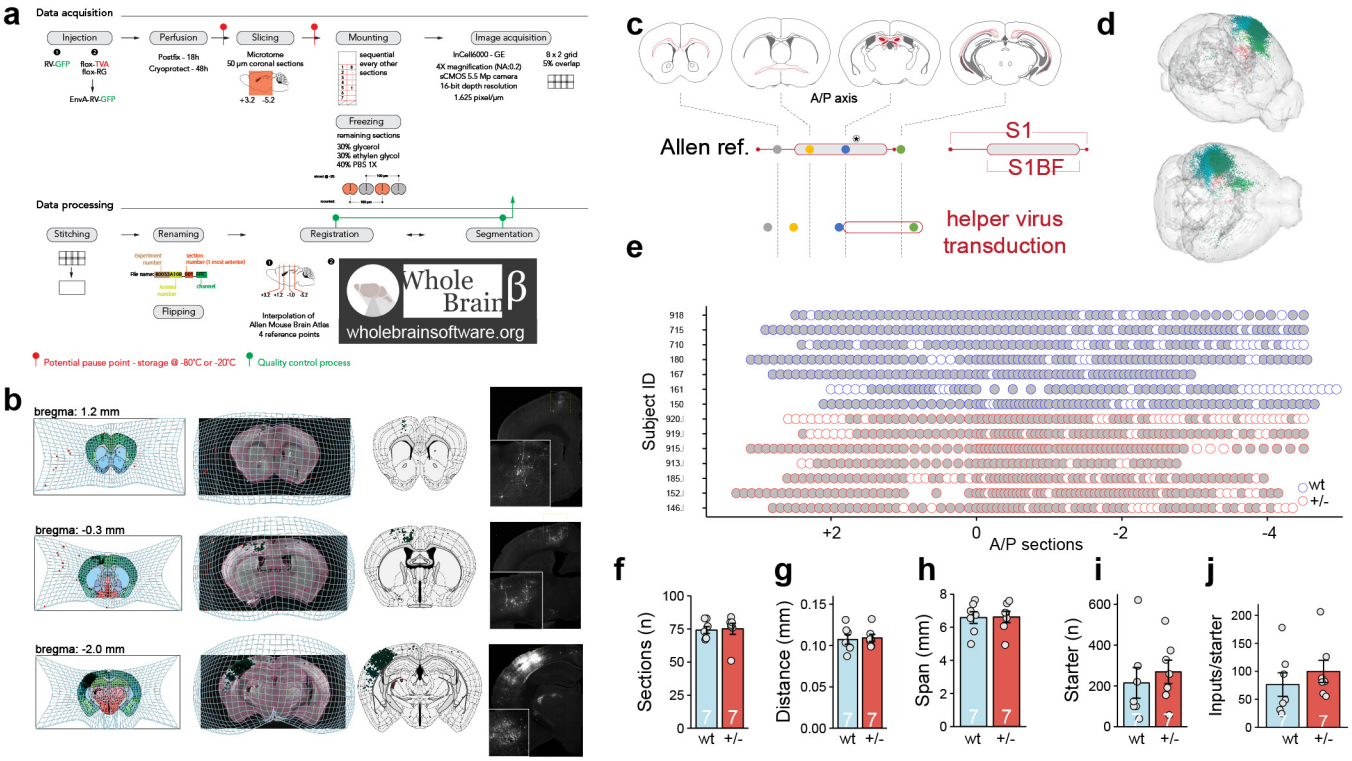
Supplementary Figure 9 *(related to Figure7)*